952129

68–

60008

QUARTERLY REPORT NO. 2
CONTRACT JPL 952129

HUGHES

HUGHES AIRCRAFT COMPANY

ION ENGINE THRUST VECTOR STUDY

JULY 1968

HUGHES RESEARCH LABORATORIES ○ MALIBU

HUGHES RESEARCH LABORATORIES
Malibu, California

a division of hughes aircraft company

ION ENGINE THRUST VECTOR STUDY

Quarterly Report No. 2
JPL Contract 952129

G.R. Brewer, K. Amboss, G. Nudd, H. King,
R. Seliger, S. Kami, D. Berman, and
J.D. Smith

July 1968

TABLE OF CONTENTS

vi

LIST OF ILLUSTRATIONS

ABSTRACT

This report describes the results of the second quarter of
the program to establish the expected degree of thrust vector mis-
alignment in an electron bombardment ion thruster. Further results
of analysis of the change in ion beam current and direction with elec-
trode displacement are presented. The degree of electrode misalign-
ment due to thermally induced stresses in the accel and screen electrodes
has been analyzed and is shown graphically. A comprehensive analysis
of the thrust stand, which will be used in Phase II to measure the beam
deflection, has been carried out and is described in this report.

I.   INTRODUCTION

This report covers the second three-months period of the subject contract. During this period the ion optical program was used to solve for six cases of normal and perturbed electrode positions; approximately five cases remain to be solved early in the third quarter. The ion optical trajectory results are analyzed in detail and linear coefficients determined between thrust vector displacement and electrode motion. The effect on current due to electrode axial motion was analyzed. The result showed, for example, that the position of the plasma sheath (which moves with the displaced accel electrode) is the strongest factor in changing the current. This is due to the change in number of ions arriving at the plasma boundary, which is a function of the shielding of the edge of the tapered screen hole.

The temperature profile over both screen and accel electrodes is determined by digital computer analysis. These data are used in thermally induced stress calculations (again by the use of a digital computer) to show the change in spacing and radial position of the two electrodes. These results, together with the ion optical coefficients, allow preliminary calculation of the axial and transverse thrust change of a single hole. This analysis will be competed for the entire thruster in the next period.

The thrust stand, using the floating suspension system, is analyzed in detail. It is shown that the system is stable and will perform satisfactorily. A comparative analysis of linear transducers and bubble sensor for error signal input is made. It is concluded that the linear transducer involves less system complexity. The photoelectric position sensor has been demonstrated experimentally.

II.   ION OPTICAL STUDY

The effort during this quarter has been concerned with the calculation of the thrust from a single perturbed aperture. The geometry of the unperturbed accelerator considered in this analysis is shown in Fig. 1. The changes in thrust produced by various electrode perturbations and ion arrival rates have also been calculated. The electrode configurations analyzed to date are illustrated in Fig. 2. The unperturbed electrode system is shown in Fig. 2(a), and Fig. 2(b) shows the accel electrode displaced axially 0.020 in. toward the screen. Figure 2(c) shows the accel electrode displaced 0.0142 in. (10% of the accel aperture diameter) normal to the axis of the system, and Fig. 2(d) shows the accel electrode tilted by 0.02 rad. Thrust calculations for a reduction in ion arrival rate have also been made, with the assumption that the geometry of the system is unperturbed.

Each perturbed aperture will produce different resultant thrust vectors, which in turn will result in different thrust values for the entire engine. An axial displacement of the accel electrode alters the magnitude of the thrust from the aperture; however, because the circular symmetry of the system is preserved, there will be no resultant transverse thrust. However, this type of displacement could produce a transverse thrust component when the effect of all apertures is considered, if the change in axial spacing is not rotationally symmetric.

In general, the rotational symmetry of the flow is destroyed by electrode shift, and the perturbed flow will be formed about a curvilinear axis. It is not possible to determine this type of flow exactly either with the analog or digital computer. However, a first order solution can be formed by a combination of an axisymmetric solution and a planar solution as described below.

A.   The Unperturbed Geometry

The unperturbed electrode system is shown in Fig. 1. The spacing between the screen and accel-electrodes is 0.090 in., and the diameters of the screen and accel apertures are 0.187 in. and 0.142 in.,

E992-10

0.090 in.

0.060 in.

0.030 in.

20°

0.187 in.

0.142 in.

SCREEN
ELECTRODE

ACCEL
ELECTRODE
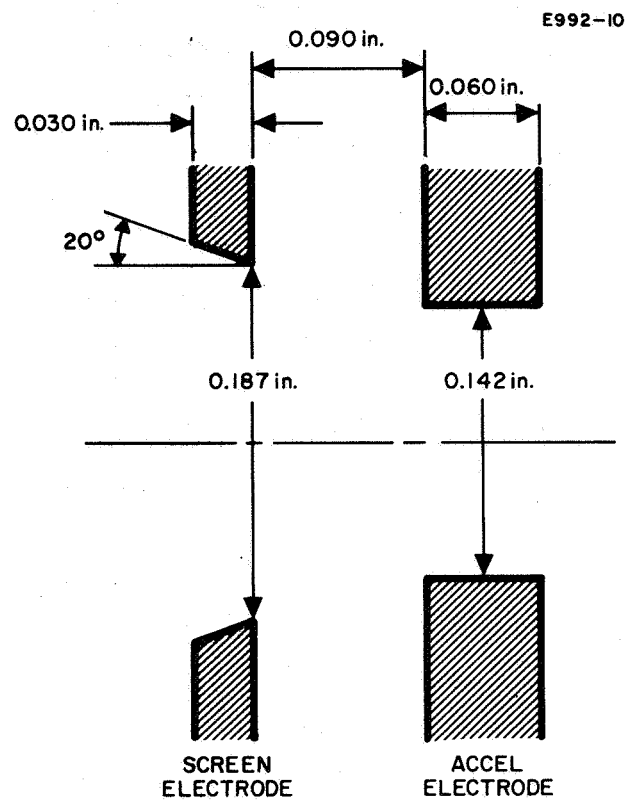
Fig. 1. Unperturbed electrode configuration.

4
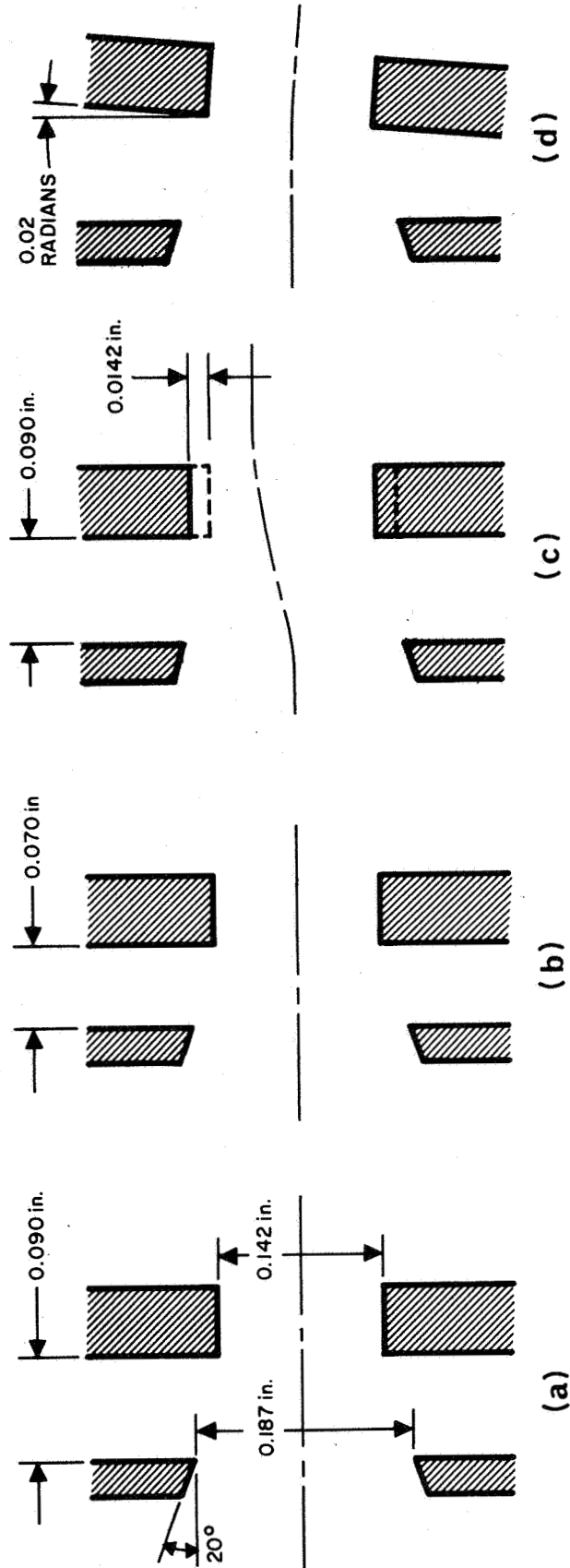
Fig. 2. Geometries considered.

E992—11

(a)

0.090 in.

0.142 in.

0.187 in.

20°

(b)

0.070 in.

(c)

0.090 in.

0.0142 in.

(d)

0.02 RADIANS

respectively. The screen electrode is shown with a re-entrant taper of 20°.

A first estimate of the upstream boundary was obtained from the electrolytic tank solutions and the correct downstream plasma boundary was found. The boundary condition for the plasma requires that both the potential and the normal electric field be zero. The method used to determine the downstream boundary consisted of specifying the correct exit potential of 0 V on a trial boundary and examining the normal electric field. The boundary was then deformed until both the above conditions were satisfied. This iterative method had to be employed since the potential and its derivative cannot be used as boundary conditions simultaneously because the Laplace and Poisson equations to be solved would become overspecified. The final solution of the downstream boundary is illustrated in Fig. 3 and is located approximately 0.330 in. in front of the screen electrode.

This boundary has been used to represent the edge of the downstream plasma for all cases considered to date. Movement of the upstream boundary produces negligible changes at the downstream plasma; the changes in the ion trajectories produced by small perturbations < (0.010 in.) of this boundary have been investigated and found to be negligible. The trajectories immediately in front of the boundary also have been examined and found to be straight. The errors introduced are thus considered to be of second order, and the correct upstream plasma boundary was then sought.

In calculations for the ion trajectories the screen electrode is assumed to be at - 40 V with respect to the emitting plasma and the accel-electrode at -4.0 kV with respect to the screen. In this case the surface of the emitting plasma will not meet the screen electrode, but will lie approximately parallel to it at a distance d (see Fig. 4). As a first estimate, therefore, d can be calculated by Child's law for a parallel diode with a voltage difference of 40 V. If this is done for a plasma

SCREEN
ELECTRODE

ACCEL
ELECTRODE

EMITTING
PLASMA

DOWNSTREAM
PLASMA
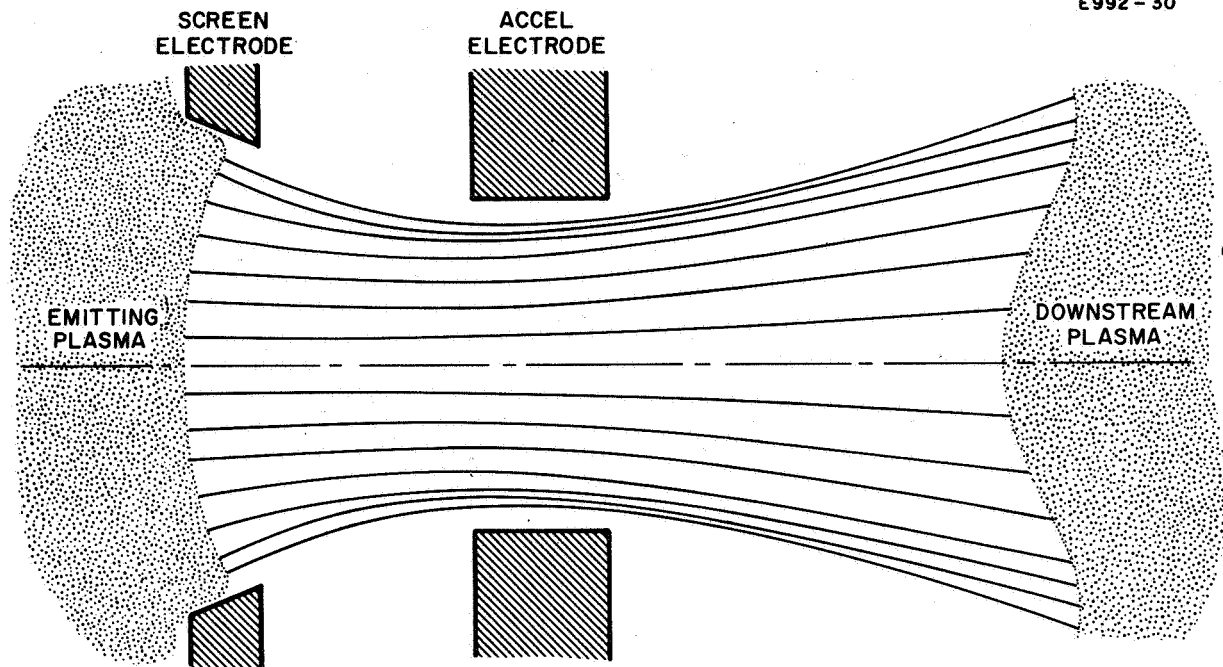
Fig. 3. Plasma boundaries and beam profile for the unperturbed
accelerator.
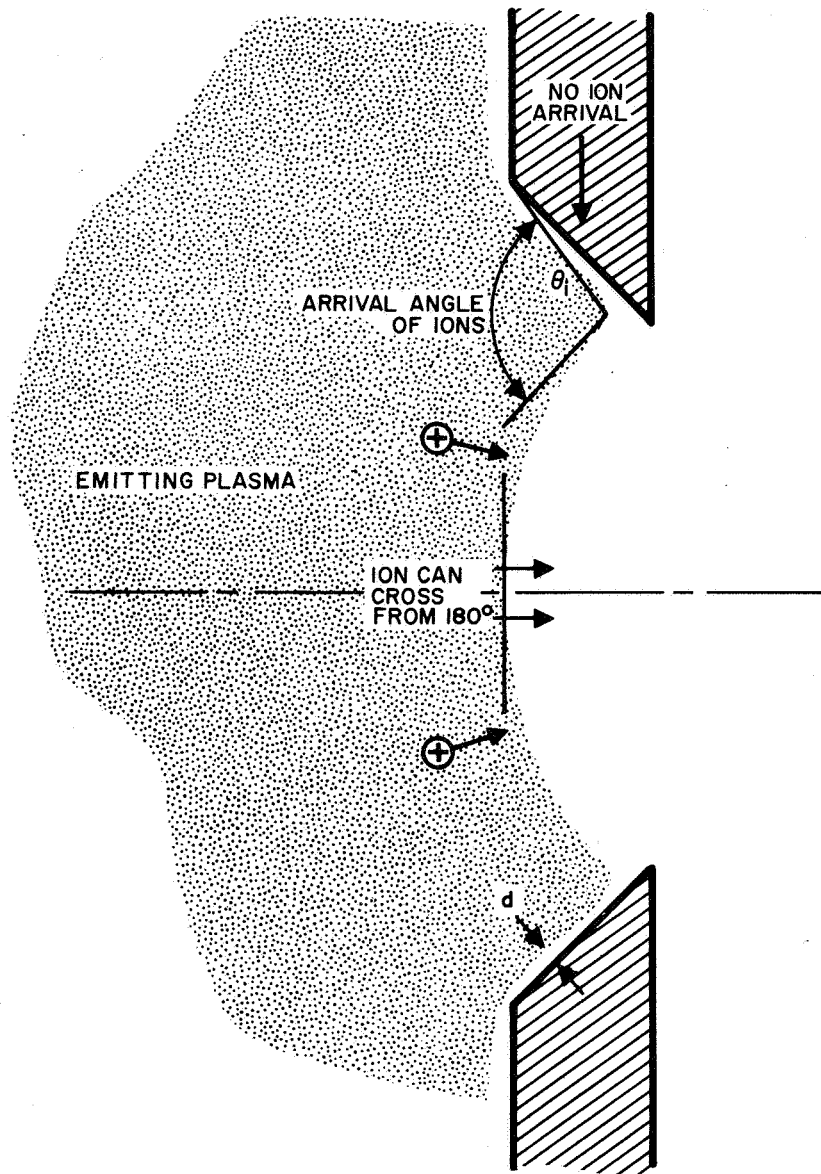
Fig. 4.   Geometry at the emitter, showing the shield-
ing effect of the screen.

with an ion arrival rate equivalent to 3.4×10^{-6} electron pervs,[*] a value of d $\simeq$ 0.005 in. is obtained.

The solution obtained in the electrolytic tank study was again used as a first estimate. Because the emitting plasma in the tank was assumed to be at screen potential, the boundary obtained had to be deformed near the screen electrode to allow for the above separation.

The boundary conditions used for the solution of the emitting surface were

    1.   The emitting surface must be an equipotential

    2.   The normal derivative of the voltage must be zero across the surface

    3.   The emission density at each point across the surface must equal the ion arrival rate at the plasma surface.

These three conditions cannot be applied simultaneously in the solution of the Poisson equation and the trajectory equation without first determining the shape and location of the boundary. Hence an iterative method was used.

The first of these conditions was met in the computer calculations by assuming that the emitting surface is a Dirichlet boundary, and the second by assuming that the emission is space-charge limited. Since the ion current is determined solely by the ion arrival rate, the location and shape of the surface must be deformed until the space-charge limited emission is exactly maintained by the arriving ions. Hence the ion arrival rate across the surface first must be calculated from the desired perveance of the unperturbed beam. In this case the assumed perveance was 3.4 μperv. As a result of the finite thickness of the screen electrode (see Fig. 3) the arriving ion current density is not uniform across the screen aperture, because the angle from which ions can arrive at the emitting surface varies with position over the aperture. For a plasma density of 10^{11} ions/cm^3 and an ion temperature of 300°C, the mean free path is of the order of 10 cm. This is

---

[*]The digital computer program is set up to calculate electron flow, and the perveance given above is therefore the electron perveance.

9

long compared with the screen thickness. In this case the ion paths can be assumed to be collision free in the vicinity of the screen electrode and the ion arrival rate at a point on the emitter surface can be calculated from the angle θ shown in Fig. 4, which shows a diametrical plane through the aperture. Hence for the ith segment in this plane the current will be proportional to the angle θ_i. The comparable angle from which the ions can arrive at the plasma boundary in the plane normal to that shown in Fig. 4 is ψ. For the unperturbed case the current density $\bar{j}_i$ in an element represented by one trajectory was calculated from the required perveance P and the product of the angles θ_i and ψ_i, using $\bar{j}_i \propto \psi_i \theta_i$ and

$$\Sigma \bar{j}_i = \frac{P}{V^{3/2}} \frac{N}{A_s}$$

where N is the number of trajectories.

A fundamental limitation arises in the solution of the plasma location in the above manner. This was reported last month and is analyzed in Appendix I. As a result, the following method was used. A number of cases for various boundaries were first run as described above until the position of the boundary was known within approximately 0.0005 in. The best location for the boundary was then estimated and the correct current distribution is imposed upon it. This step is equivalent to assuming a small initial velocity of ions at the emitter, which is true in practice. The solution of the plasma boundaries and the beam profile for the unperturbed geometry is shown in Fig. 5 and the results are summarized in Table I.

The computer program, when used to solve problems with axial symmetry, divides the flow into a number of annular segments centered on the axis of symmetry and calculates a self-consistent ion trajectory for each segment. Each trajectory so calculated illustrates the flow of all the ions emitted from its annular segment. If I_i is the current associated with the ith annular segment, the total axial thrust T_A from the aperture is

10
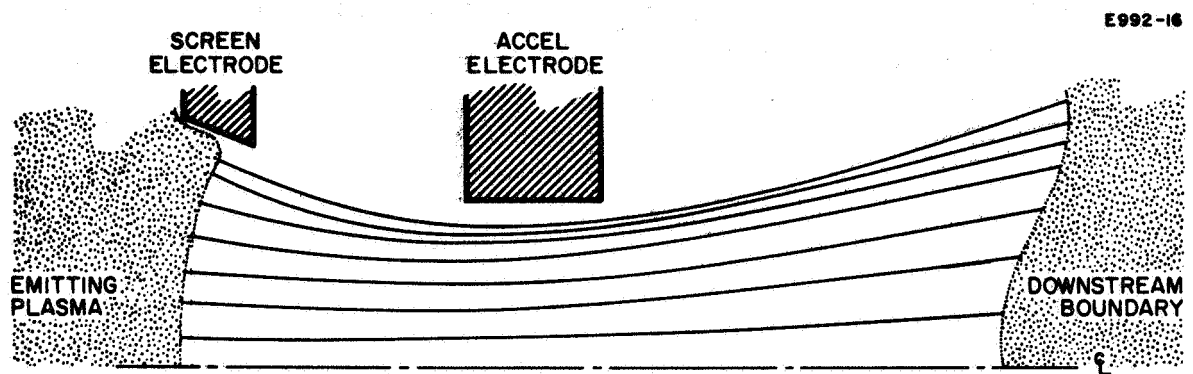
Fig. 5.   Ion trajectories for the unperturbed geometry ($P = 3.4 \times 10^{-6}$ electron pervs).

TABLE I

Thrust Calculated for Three Electrode Configurations

Case Number	Screen/ Accel Spacing, in.	Average Current Density,[a] A/cm^2	Total Current A	Electron Perv $\times 10^{-6}$	Axial Thrust lb $\times 10^{-5}$	$\frac{\delta T}{T}$, %	$\frac{\delta T_1}{T}$, %	$\frac{\delta T_2}{T}$, %	$\frac{\delta T_3}{T}$, %	$\frac{\delta T_4}{T}$, %
1	0.090	7.87	0.00132	3.4	2.503	—	—	—	—	—
2	0.070	8.87	0.00149	3.83	2.829	13	1.43	8.9	2.67	—
3	0.090	4.5	0.000753	1.942	1.502	-40	2.96	8.6	2.7	54.3

[a]Evaluated at the screen aperture.

$$T_A = k \sum_i I_i \sqrt{V} \cos \phi_i \qquad (1)$$

where the summation is for all the trajectories and where

$V \equiv$ the voltage difference between upstream and down-stream plasma

$\phi_i \equiv$ the angle between the trajectory and axis at down-stream boundary — (the exit angle).

k is a constant.

The total axial thrust for the unperturbed geometry was calculated to be 2.503×10^{-5} lb.

The transverse thrust $T_\perp$ is given by an expression similar to (1)

$$T_\perp = k \sum_i I_i \sqrt{V} \sin \phi_i \quad ; \qquad (2)$$

because of axial symmetry, however, the summation leads to zero.

B.   Axial Misalignments

It has been found that the major contribution to the change in thrust for axial displacements results from the movement of the upstream plasma boundary rather than from the change of direction of the trajectories downstream. A change in screen-accel electrode spacing causes the form and position of the boundary to change, resulting in a change in emitting area and hence in the total emitted current. The total current I_t passing through a single aperture can be expressed as

$$I_t = \sum_{o}^{A_s} \overline{j}_o \, (\Delta A_i) \, F_i \tag{3}$$

where $\overline{j}_o$ is the density of current flowing through an element of area ΔA_i on the emitting surface, F_i is the "view factor" which accounts for the shielding effect of the screen electrode. A_s is the total curved surface area of the emitting plasma, and the summation is for all elements on the emitting surface. It can be seen that an increase in area A_s will cause an increase in total current and hence an increase in the thrust. The axial thrust from an aperture calculated from (1) can be expressed by means of (3) as

$$T = k \sqrt{V} \, \Sigma \, \overline{j}_o \, (\Delta A_i) \, F_i \cos \phi_i \tag{4}$$

From (4) we can find the effect of changes in the various parameters

$$\delta T_A = \Sigma \left(\frac{\partial T_i}{\partial (\Delta A_i)} \, \delta(\Delta A_i) \right) + \Sigma \left(\frac{\partial T_i}{\partial F_i} \, \delta F_i \right) + \Sigma \, \frac{\partial T_i}{\partial (\cos \psi_i)} \, \delta(\cos \phi_i)$$

$$= \Sigma T_i \, \frac{\delta(\Delta A_i)}{\Delta A_i} + \Sigma T_i \, \frac{\delta F_i}{F_i} + \Sigma T_i \, \frac{\delta(\cos \phi_i)}{\cos \phi_i} \, . \tag{5}$$

The first two components result solely from changes in the emitting plasma boundary while the third is an ion optical effect. The relative importance of the three components can be estimated from the magnitudes of

13

$$\frac{\delta(A_i)}{A_i}, \quad \frac{\delta F_i}{F_i} \quad \text{and} \quad \frac{\delta(\cos \phi_i)}{\cos \phi_i}$$

When the solution obtained for the unperturbed geometry is compared with that for a 22% decrease in accel-screen spacing, the change in thrust resulting from ion optics can be shown to be small compared with that resulting from the boundary movement. This can readily be seen if δT_A is expressed as

$$\delta T_A = \Sigma \left(\frac{\partial T_i}{\partial I_i} \delta I_i \right) + \Sigma \left(\frac{\partial T_i}{\partial (\cos \phi_i)} \delta(\cos \phi_i) \right)$$

$$= \Sigma T_i \frac{\delta I_i}{I_i} + \Sigma T_i \frac{\delta(\cos \phi_i)}{\cos \phi_i} \tag{6}$$

and if the maximum values $\delta I_i / I_i$ and $\delta(\cos \phi_i)/\cos \phi_i$ are compared. Since

$$\delta \frac{(\cos \phi_i)}{\cos \phi_i} = \tan \phi_i \, \delta \phi_i$$

ϕ_i is small (less than 20° for all trajectories and $\tan 20^\circ = 0.36$) and the maximum value of $\delta \phi_i < 0.1$, this term will be less than 0.036. However, the maximum value of $\delta I_i / I_i = 0.13$. Hence the change in thrust resulting from the change in current is the dominant factor in this case; this result is somewhat unexpected at first glance.

When the actual values rather than the maximum values are used for the 22% decrease in axial spacing, summing for all the trajectories we obtain

$$\frac{\delta I_t}{I_t} = 0.117;$$

hence, for δT_A,

14

$$\Sigma \, T_i \frac{\delta I_i}{I_i} = 2.9 \times 10^{-6}$$

$$\Sigma \, T_i \frac{\delta(\cos \phi_i)}{\cos \phi_i} = 3.6 \times 10^{-7}$$

However, the increase in emitted current results from two factors: the increase in emission area and the increase in view factor. We can therefore write

$$I_t = \Sigma I_i = J_o \, \Sigma'(\Delta A_i) \, F$$

$$\delta I_t = \Sigma \, \frac{\partial I_i}{\partial(\Delta A_i)} \, \delta(\Delta A_i) + \Sigma \, \frac{\partial I_i}{\partial F} \, \delta F$$

$$= \Sigma \, J_o \, \delta(\Delta A_i) \, F + \Sigma J_o \, \delta F \, (\Delta A_i)$$

$$= \Sigma J_o \, (\Delta A_i) \, F \, \frac{\delta(\Delta A_i)}{\Delta A_i} + \Sigma \, J_o \, \delta F \, (\Delta A_i) \qquad (7)$$

Since the trajectories calculated represent annuli of equal thickness, the fractional change in emitting area will be the same for all elements and we can write

$$\frac{\delta(\Delta A_i)}{\Delta A_i} \text{ (is constant)} = \frac{\delta A_s}{A_s} \, . \qquad (8)$$

Therefore,

$$\delta I_t = I_t \, \frac{\delta A_s}{A_s} + \Sigma \, J_o \, \delta F_i \, (\Delta A_i)$$

or

$$\frac{\delta I_t}{I_t} = \frac{\delta A_s}{A_s} + \frac{\Sigma J_o \, \delta F_i \, (\Delta A_i)}{I_t} \, . \qquad (9)$$

In this case $\delta A_s / A_s$ was calculated to be approximately 0.09; hence the change in current resulting from the change in view factor is approximately 2.7%.

We can now write the change in thrust δT_A as

$$\frac{\delta T_A}{T_A} = \frac{\delta T_{1,A}}{T_A} + \frac{\delta T_{2,A}}{T_A} + \frac{\delta T_{3,A}}{T_A} \qquad (10)$$

where

$\delta T_{1,A} \equiv$ change in axial thrust due to change in ion paths alone

$\delta T_{2,A} \equiv$ change in axial thrust due to change in emitting area

$\delta T_{3,A} \equiv$ change in axial thrust due to change in screen electrode shielding.

The results for the case of a 0.020 in. axial movement of the accel electrode are given in Table I. Since axial symmetry is assumed, there is no resultant transverse thrust.

A further case has been solved assuming axial symmetry. This is also included in Table I, designated Case 3. For this case it is assumed that the geometry is unperturbed but the ion arrival rate is reduced. Hence the emitting plasma boundary will recede until the reduced ion arrival rate is sufficient to maintain self-consistent space-charge emission.

In this case the change in thrust is given by

$$\delta T_A = \Sigma T_i \frac{\delta I_i}{I_i} + \Sigma T_i \frac{\delta(\cos \phi_i)}{\cos \phi_i} \qquad (11)$$

where

$$\delta I_i = I_t \frac{\delta A_s}{A_s} + I_t \frac{\delta \bar{j}_o}{\bar{j}_o} + \Sigma \bar{j}_o \, \delta F \, (\Delta A_i) \qquad (12)$$

because the ion arrival rate $\bar{j}_o$ varies.

Using the above notation we can write

$$\frac{\delta T_A}{T_A} = \frac{\delta T_{1,A}}{T_A} + \frac{\delta T_{2,A}}{T_A} + \frac{\delta T_{3,A}}{T_{A,}} + \frac{\delta T_{4,A}}{T_A} \qquad (13)$$

where $\delta T_{4,A} \equiv$ the change in thrust because of the change in ion arrival rate. The trajectories calculated for cases 1, 2, and 3 are shown in Figs. 5, 6 and 7, respectively.

The results of the perturbations which preserve axial symmetry are illustrated in Figs. 8 and 9. It can be seen that the total change in thrust resulting from a change in electrode spacing of 0.020 in. is 0.326×10^{-5} lb. Hence if it is assumed that the change is linear for small perturbations, a proportionality factor α can be defined such that

$$\alpha = \frac{\text{change in thrust}}{\text{change in electrode spacing}}$$

$$= -0.000163 \text{ mlb/thousandths of an inch.}$$

The change in thrust due to a decrease in ion arrival rate of 54.3% is shown in Fig. 8 to be 0.884×10^{-5} lb. A proportionality constant β can similarly be defined such that

$$\beta = \frac{\text{change in thrust}}{\text{change in total current emitted}}$$

$$= 0.01765 \text{ mlb/mA .}$$

C.   Transverse Misalignments

When a transverse displacement of the accel-electrode is made, the axis of symmetry of the aperture is destroyed; hence the ion motion cannot be solved assuming circular symmetry. This type of distortion is illustrated in Fig. 10 where the axis of the screen electrode and the accel electrode are shown displaced by a distance ϵa (where a is the radius of the accel aperture).

17
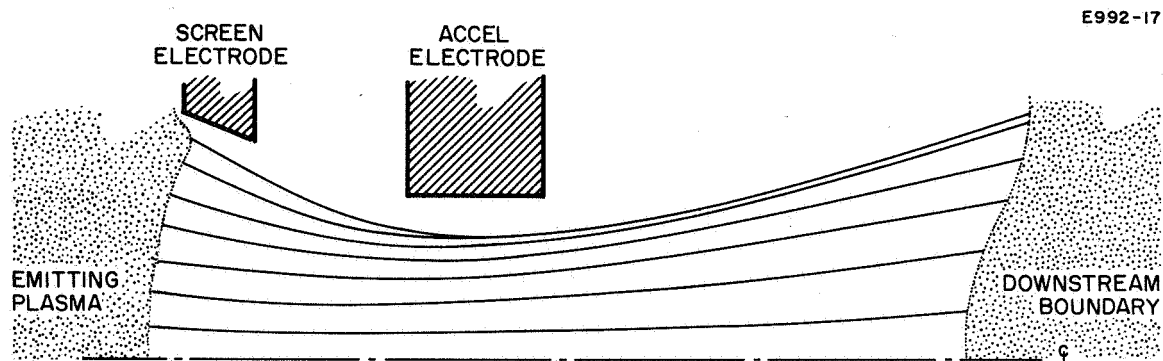
Fig. 6. Ion trajectories for a screen-to-accel electrode spacing of
0.070 in. (P = 3.4 x 10^{-6} electron pervs).
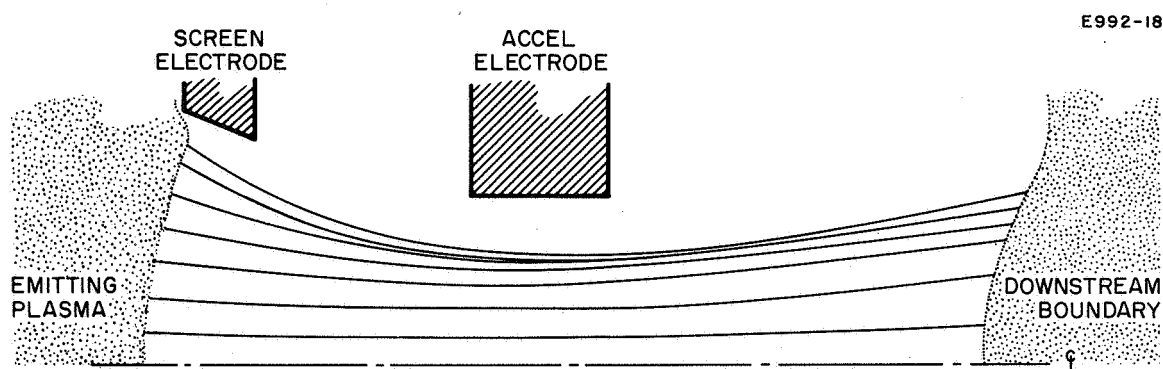
Fig. 7. Ion trajectories for the unperturbed geometry but with a re-
duced emission (P = 1.9 x 10^{-6} electron pervs).
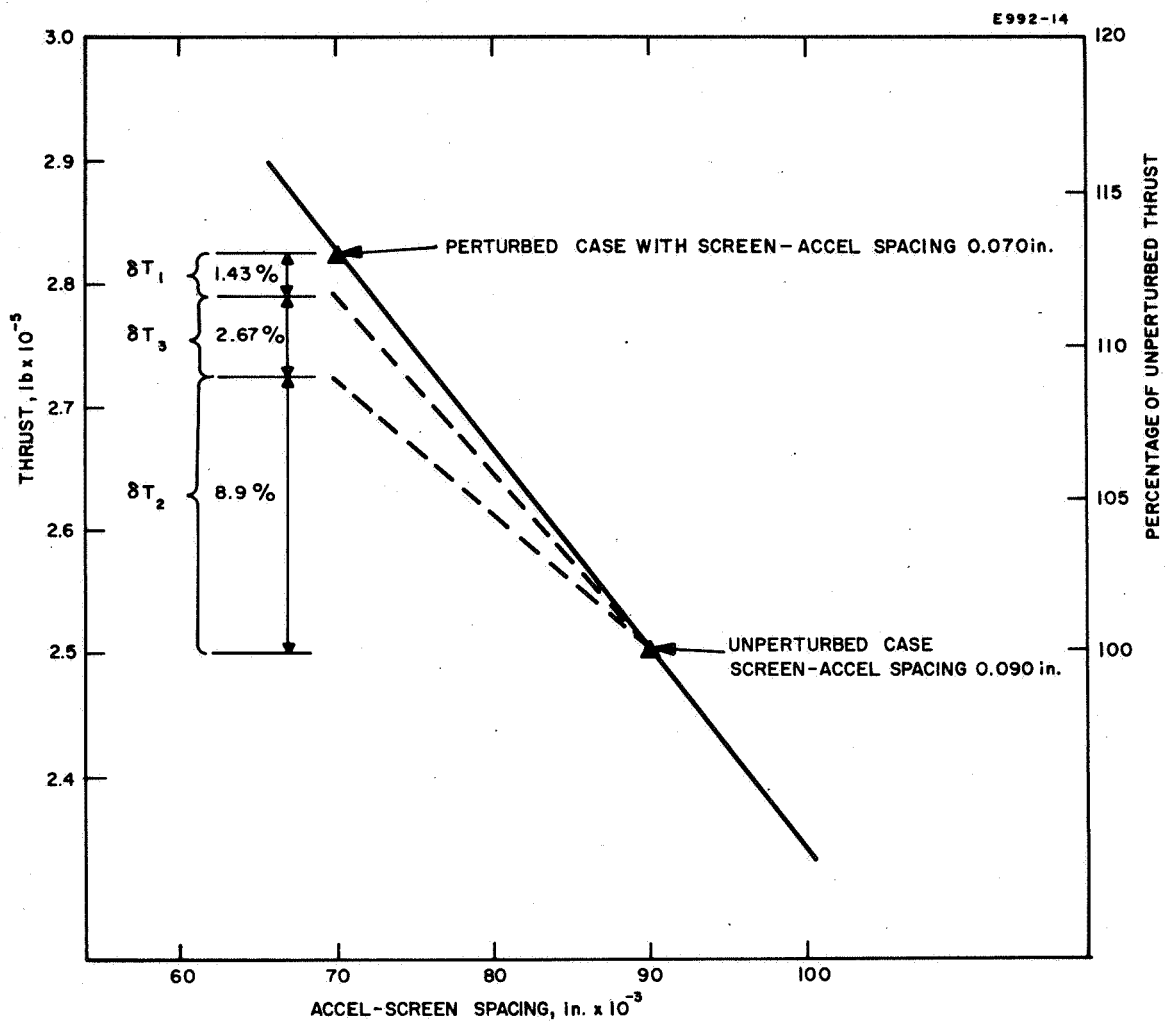
Fig. 8. Change in axial thrust with electrode spacing. δT_1 = change in axial thruster due to ion paths. δT_2 = change in axial thrust due to emitting area. δT_3 = change in axial thrust due to screen shielding.
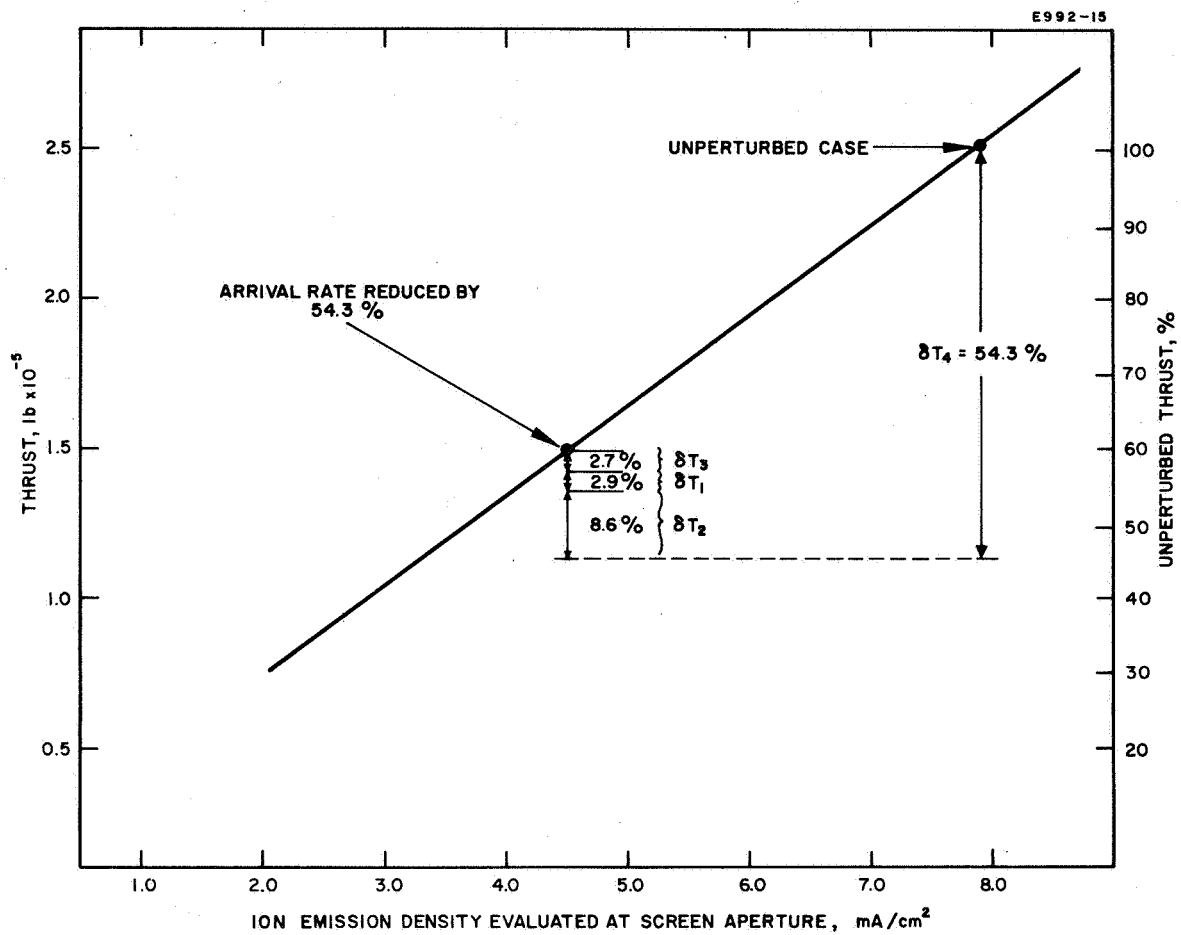
Fig. 9. Ion emission density at screen aperture.
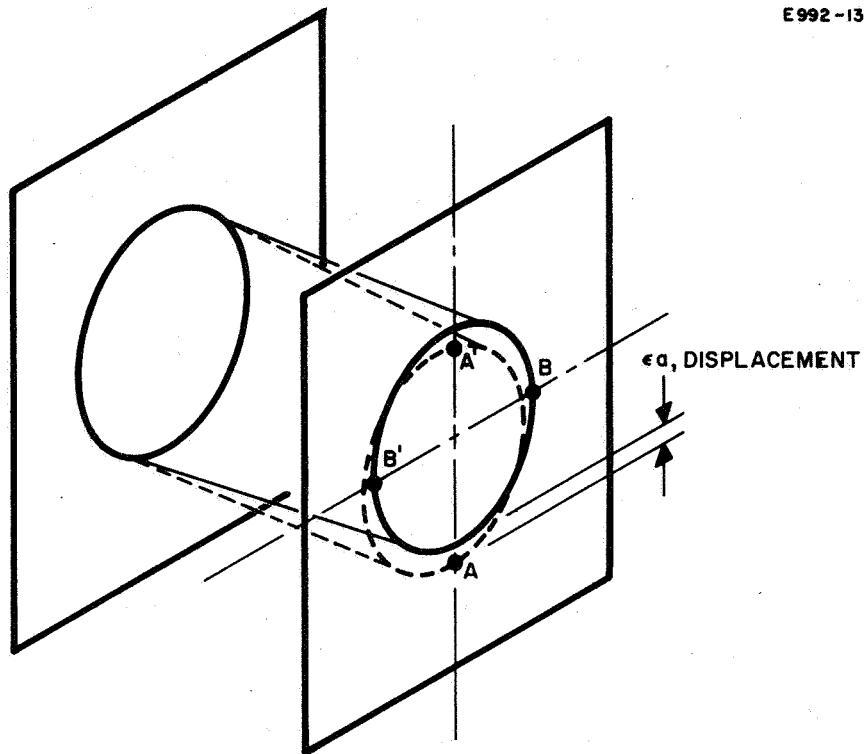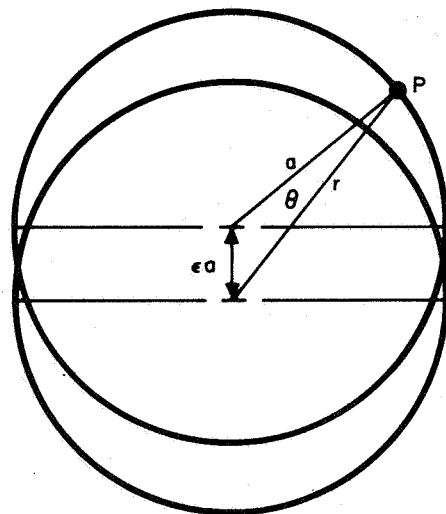
ɛa, DISPLACEMENT

Fig. 10. Displacement of the accel electrode of ɛa
normal to the axis of the unperturbed
system.

The R - θ equation of the displaced surface can be found by expressing

$$R = x + i y \qquad\qquad (14)$$

where

$$x = a\cos\theta$$

$$y = \epsilon a + a\sin\theta;$$

hence

$$R = (x^2 + y^2)^{1/2}, \qquad\qquad (15)$$

or to first order

$$R = (a^2 + 2\epsilon a^2 \sin\theta)^{1/2} = a(1 + \epsilon \sin\theta) \qquad (16)$$

It can thus be seen that this type of displacement introduces a perturbation in the radial coordinate R which varies as $\sin\theta$.

If two sections are drawn through the system normal to each other, representing the planes of least and greatest perturbations, the axis lines of the two electrodes will coincide in the first plane and be displaced by ϵ_a in the second plane. The trajectory equation can be solved as a planar problem for these two cases and the result will be as illustrated in Fig. 11. It can be seen that the calculated trajectories will differ. The effect of this transverse displacement can be thought of as displacing each trajectory through an angle δ_i. Hence, for the trajectories nearest the screen the change in exit angle if δ_{27} at the top and δ_1 at the bottom.

If it is assumed that the change in exit angle varies as $\sin\theta$ in the azimuthal direction (as shown in Fig. 12), the angular displacement of the outermost trajectory in a plane at an angle $(\pi/2 - \theta)$ from the plane of the displacement can be written as
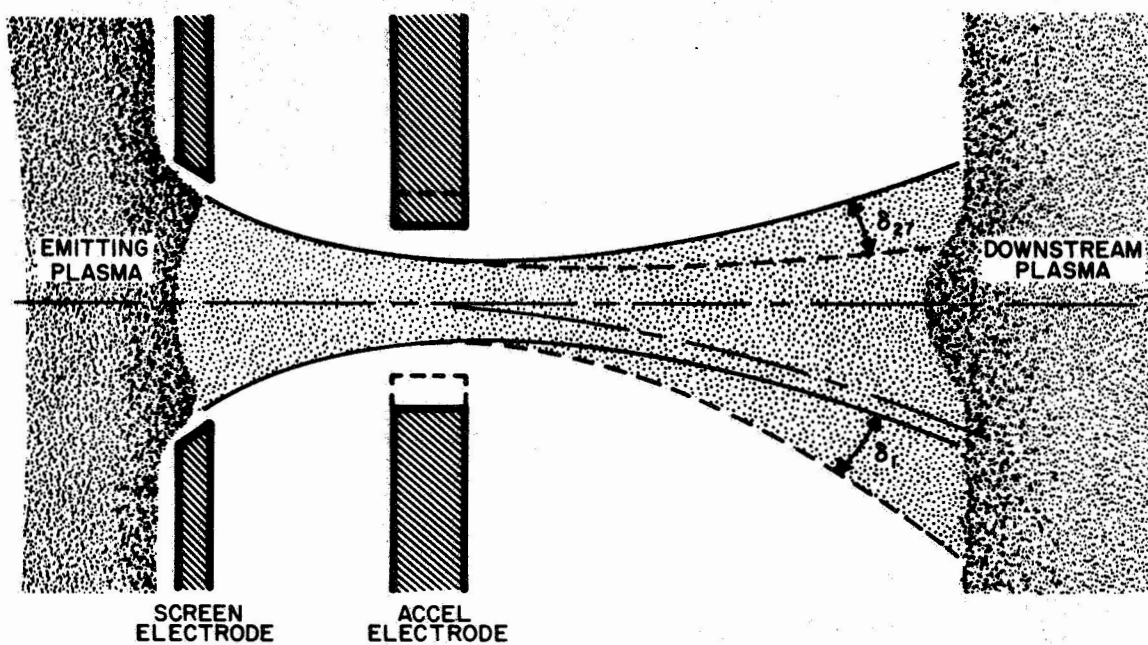
Fig. 11.   Effect of translational misalignment of the ion paths calcu-
lated assuming planar symmetry (dotted lines represent
perturbed solutions).
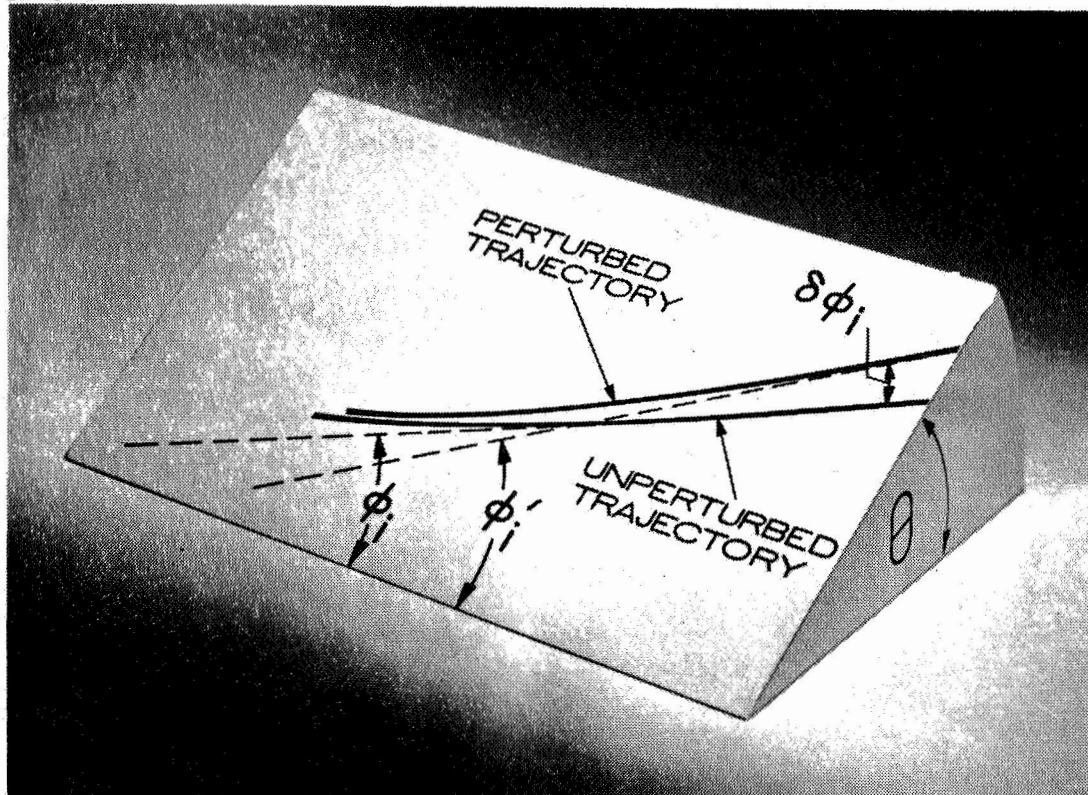
Fig. 12. Three-dimensional representation of the perturbed and
unperturbed trajectories.

$$- \frac{1}{2} (\delta_1 + \delta_{27}) \sin \theta + \frac{1}{2} (\delta_1 - \delta_{27}) . \qquad (17)$$

Hence in a plane normal to the displacement where $\theta = 0$, the change in exit angle $\delta\phi_i$ is $1/2 (\delta_1 - \delta_{27})$. In the plane of the displacement at $\theta = \pi/2$, $\delta\phi_i = -\delta_{27}$; at $\theta = -\pi/2$,

$$\delta\phi_1 = \delta_1 .$$

Hence from a small element shown in Fig. 13 where the current density is $\overline{j}_i$, the axial thrust is given by

$$\Delta T_{i, A} = \overline{j}_i \, \delta S_i \cos \phi_i' \, t_i \sqrt{V} \qquad (18)$$

where ϕ_i' is the exit angle

$$\delta S_i = R_i \, \delta\theta$$

$$R_i \equiv \text{ radial coordinate of the element}$$

$$\delta\theta \equiv \text{ angular width of the element.}$$

Therefore,

$$\Delta T_{i, A} = R_i \, t_i \sqrt{V} \, \overline{j}_i \cos \phi_i' \, \delta\theta . \qquad (19)$$

Hence the total thrust from the annulus shown is

$$T_{i, A} = \Sigma (R_i \, t_i \, \overline{j}_i) \sqrt{V} \cos \phi_i' \, \delta\theta \qquad (20)$$

In this equation we can write $J_i \, \delta\theta = R_i \, t_i \, \overline{j}_i \, \delta\theta$. J_i is the current per radian in the ith trajectory; therefore, $J_i \delta\theta$ is the current contained in an element of the ith trajectory subtended by an angle $\delta\theta$ at the axis.

ACCEL
ELECTRODE

$\delta\theta$

R_i

J_i

ϕ_i
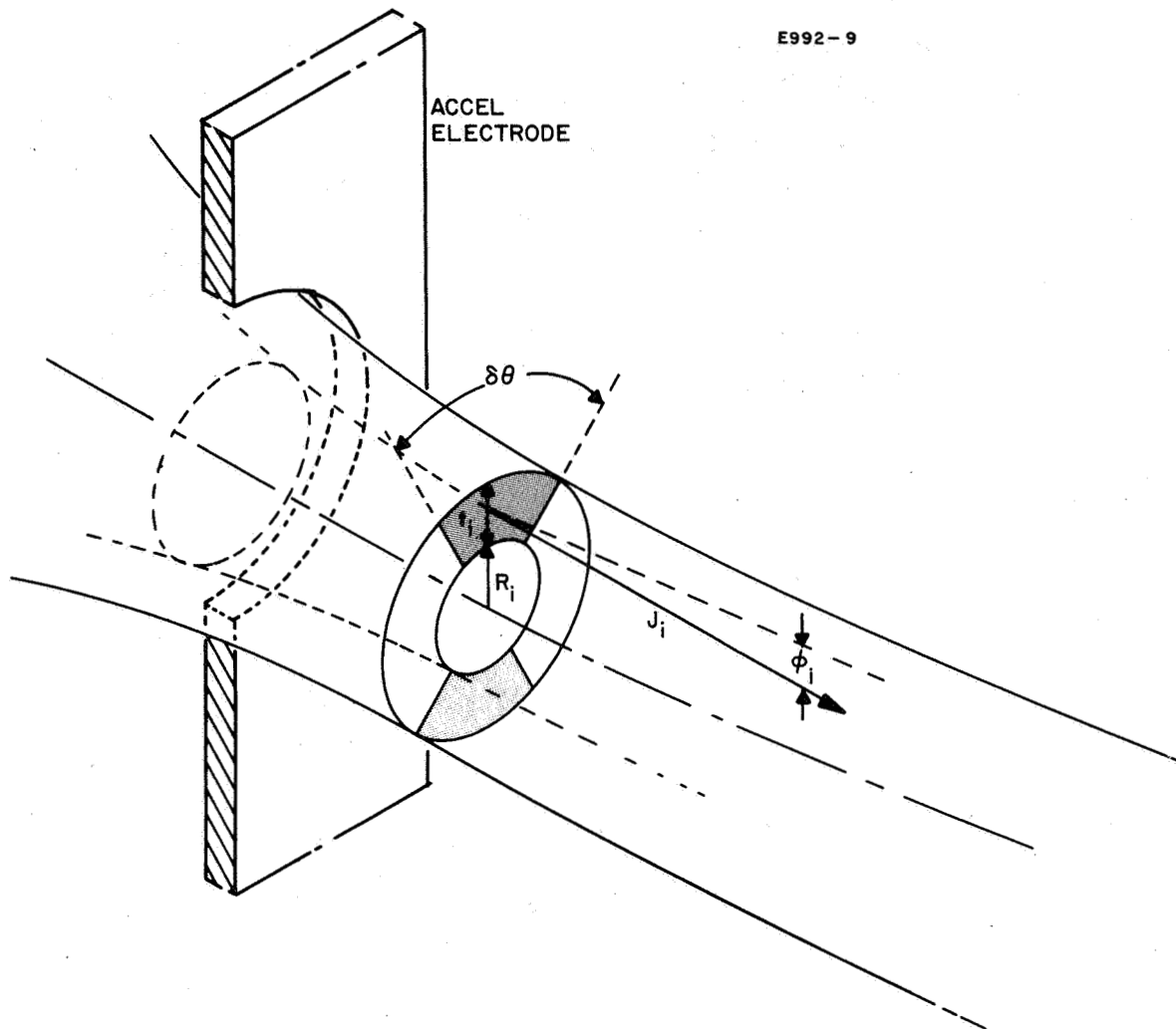
Fig. 13. Element of flow from a single aperture.

Hence $I_i = \Sigma J_i \, \delta\theta$. Since boundary conditions for the upstream plasma are that the emission density be equivalent to the ion arrival rate at the surface and that the ion density be assumed constant across a single aperture, it can be shown that variations in J_i with θ will produce second order perturbations in the thrust. (Variations in J_i will be produced by variations in the shielding effect of the screen electrode only because of the asymmetry of the upstream boundary.) Hence

$$J = \frac{I_i}{2\pi} \ .$$

In (20),

$$\phi_i' = \phi_i - \frac{1}{2} (\delta_i + \overline{\delta}_i) \sin\theta + \frac{1}{2} (\delta_i - \overline{\delta}_i) \tag{21}$$

where

$$\phi_i \equiv \text{ exit angles for the unperturbed axisymmetric run}$$

$$\delta_i \equiv \text{ maximum positive angular displacement}$$

$$\overline{\delta}_i \equiv \text{ maximum negative angular displacement.}$$

Hence

$$T_i = \frac{I_i \sqrt{V}}{2\pi} \int_0^{2\pi} \cos\left\{ \phi_i + \frac{(\delta_i - \overline{\delta}_i)}{2} + \frac{(\delta_i + \overline{\delta}_i)}{2} \sin\theta \right\} d\theta$$

$$= \frac{I_i \sqrt{V}}{2\pi} \left[\cos\left(\phi + \frac{\delta_1 - \overline{\delta}_i}{2} \right) \int_0^{2\pi} \cos\left(\frac{(\delta_i + \overline{\delta}_1)}{2} \sin\theta \right) d\theta \right.$$

$$\left. - \sin\left(\phi + \frac{\delta_1 - \overline{\delta}_i}{2} \right) \int_0^{2\pi} \sin\left(\frac{\delta_i + \delta_1}{2} \sin\theta \right) d\theta \right] \tag{22}$$

27

However,

$$\int_0^{2\pi} \cos\left(\left(\frac{\delta_i + \overline{\delta}_i}{2}\right)\sin\theta\right) d\theta = 2\pi J_0\left(\frac{\delta_i + \overline{\delta}_i}{2}\right)$$

where J_0 is the Bessel function of order zero and

$$\int_0^{2\pi} \sin\left(\frac{\delta_i + \overline{\delta}_i}{2}\sin\theta\right) d\theta = 0 .$$

Hence

$$T_i = I_i \sqrt{V} J_0\left(\frac{\delta_i + \overline{\delta}_i}{2}\right)\cos\left(\phi_i + \frac{\delta_i - \overline{\delta}_i}{2}\right) \tag{23}$$

The total perturbed axial thrust is therefore given by

$$T_0 = \Sigma I_i \sqrt{V} J_0\left(\frac{\delta_i + \overline{\delta}_i}{2}\right)\cos\left(\phi_i + \frac{\delta_i - \overline{\delta}_i}{2}\right). \tag{24}$$

The self-consistent ion trajectories have been solved for the unperturbed and perturbed geometries, and the results are shown in Figs. 14 and 15. The perturbation introduced was a transverse shift of the accel electrode of 0.0142 in. A self-consistent upstream boundary was found for the perturbed case. It can be seen that the beam is deflected in an opposite direction to the perturbation, and that the two beam edges are moved in this direction by approximately equal amounts. This result is in agreement with previous work.[1] The angular deflection at the edges is about 4°; hence for the beam edge the angular deflection can be calculated to be $0.028^\circ/\text{mil}$. However, the mean angular deflection $\overline{\delta\phi}_i$ is calculated as

$$\overline{\delta\phi}_i = \sum_i^N \frac{(\delta\phi_i)}{N}$$

where

$$N \equiv \text{number of trajectories}$$
$$= 8.2^\circ .$$

28
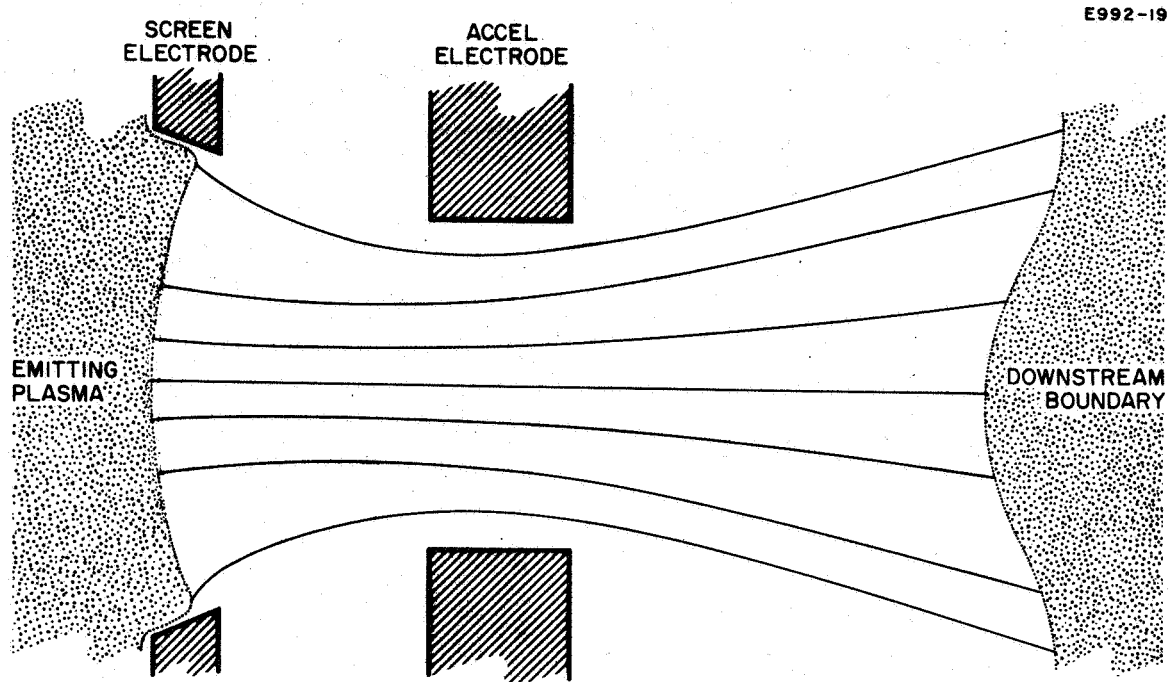
Fig. 14.   Ion trajectories for the unperturbed geometry (solved assuming planar symmetry).
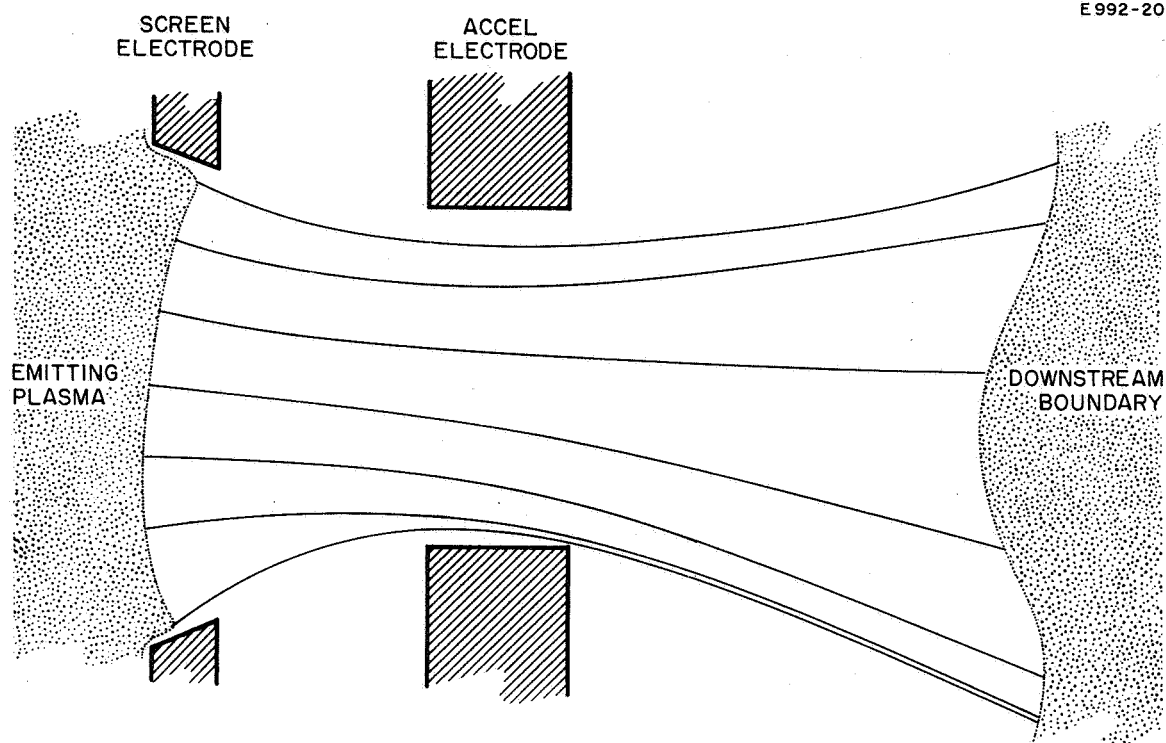
Fig. 15. Ion trajectories for a 0.0142 in. displacement of the accel electrode.

Hence if it is assumed that the mean angular deflection is a linear function of transverse displacement of the accel electrode, the proportionality constant can be calculated as $0.578^{\circ}/\text{mil}$. In metric units this is equivalent to $23.2^{\circ}/\text{mm}$, which compares with a value of $29^{\circ}/\text{mm}$ reported by other workers.[2] This difference can be explained by a number of factors. The geometry and voltages assumed in this case are somewhat different. Thus the lens produced in our geometry is slightly stronger, which tends to reduce the divergence. In previous work no account was taken of the relocation of the emitting plasma caused by the electrode perturbation; in addition, the correct position of the downstream boundary was not determined. Nevertheless it can be seen that there is quite good agreement, and a first order analysis of the effects caused by the above discrepancies indicates that the two values are consistent to within approximately 5%.

If the total thrust is calculated using

$$T = \Sigma I_i \sqrt{V} \, J_0 \left(\frac{\delta_i + \overline{\delta}_i}{2} \right) \cos \left(\phi_i + \frac{\delta_i - \overline{\delta}_i}{2} \right) ,$$

a value of 2.472×10^{-5} lb is obtained.

The transverse thrust $\overrightarrow{T'}$ is a vector which can be represented by its components T_1' and T_2' where T_1' is the component of thrust parallel to the displacement ϵa and T_2' is the component normal to it.

Then

$$T_1' = \Sigma \int_0^{2\pi} \frac{I_i}{2\pi} \sqrt{V} \, \sin \phi_i' \sin \theta \, d\theta \qquad (25)$$

and

$$T_2' = \Sigma \int_0^{2\pi} \frac{I_i}{2\pi} \sqrt{V} \, \sin \phi_i' \cos \theta \, d\theta \qquad (26)$$

where

$$\phi_i = \phi_i + \frac{1}{2} (\delta_i + \overline{\delta}_i) \sin \theta + \frac{1}{2} (\delta_i - \overline{\delta}_i)$$

and the summation is for i = 1 to 27.

We can write

$$T'_1 = \Sigma \int_0^{2\pi} \frac{I_i}{2\pi} \sqrt{V} \left\{ \sin \left(\phi_i + \frac{\delta_i - \overline{\delta}_i}{2} \right) \cos \left(\frac{\delta_i + \overline{\delta}_i}{2} \sin \theta \right) \right.$$

$$\left. + \cos \left(\phi_i + \frac{\delta_i - \overline{\delta}_i}{2} \right) \sin \left(\frac{\delta_i + \overline{\delta}_i}{2} \sin \theta \right) \right\} \sin \theta \, d\theta \qquad (27)$$

and

$$T'_2 = \Sigma \int_0^{2\pi} \frac{I_i}{2\pi} \sqrt{V} \left\{ \sin \left(\phi_i + \frac{\delta_i - \overline{\delta}_i}{2} \right) \cos \left(\frac{\delta_i + \overline{\delta}_i}{2} \sin \theta \right) \right.$$

$$\left. + \cos \left(\phi_i + \frac{\delta_i - \overline{\delta}_i}{2} \right) \sin \left(\frac{\delta_i + \overline{\delta}_i}{2} \sin \theta \right) \right\} \cos \theta \, d\theta \quad . \qquad (28)$$

Noting that

$$\int_0^{2\pi} \sin \left(\frac{1}{2} (\delta_i + \overline{\delta}_i) \sin \theta \right) \cos \theta = 0$$

$$\int_0^{2\pi} \sin \left(\frac{1}{2} (\delta_i + \overline{\delta}_i) \sin \theta \right) \sin \theta = 2\pi J_1 \left(\frac{\delta_i + \overline{\delta}_i}{2} \right)$$

$$\int_0^{2\pi} \cos \left(\frac{1}{2} (\delta_i + \overline{\delta}_i) \sin \theta \right) \cos \theta = 0$$

$$\int_0^{2\pi} \cos \left(\frac{1}{2} (\delta_i + \overline{\delta}_i) \sin \theta \right) \sin \theta = 0 \qquad (29)$$

32

We can write

$$T_1' = \Sigma I_i \sqrt{V} \cos\left(\phi_i + \frac{\delta_i - \bar{\delta}_i}{2}\right) J_1\left(\frac{\delta_i + \bar{\delta}_i}{2}\right) \tag{30}$$

$$T_2' = 0. \tag{31}$$

The transverse thrust calculated for the displacement of 0.0142 in. can be calculated to be $= 2.529 \times 10^{-6}$ lb. This represents a rotation of the thrust vector of $\tan^{-1} (0.103)$ or 5.84°. Again if these changes are assumed to be linear we can define

$$\eta = \frac{\text{change in transverse thrust}}{\text{transverse displacement of the accel}}$$

$$= 1.78 \times 10^{-7} \text{ lb/thousandth of an inch}$$

$$\omega = \frac{\text{rotation of the thrust vector}}{\text{transverse displacement of the accel}}$$

$$= 0.411^\circ/\text{thousandth of an inch}$$

The change in axial thrust $\delta T = 0.031 \times 10^{-5}$ lb, or 1.24%. If this change is assumed to be linear with transverse displacement we can define

$$\gamma = \frac{\text{change in axial thrust}}{\text{displacement of the accel-electrode}}$$

$$= -0.00218 \times 10^{-5} \text{ lb/thousandth of an inch}$$

These results are illustrated in Fig. 16.

In general, the changes in transverse thrust due to transverse displacements can be shown to be about an order of magnitude greater than the changes in axial thrust.
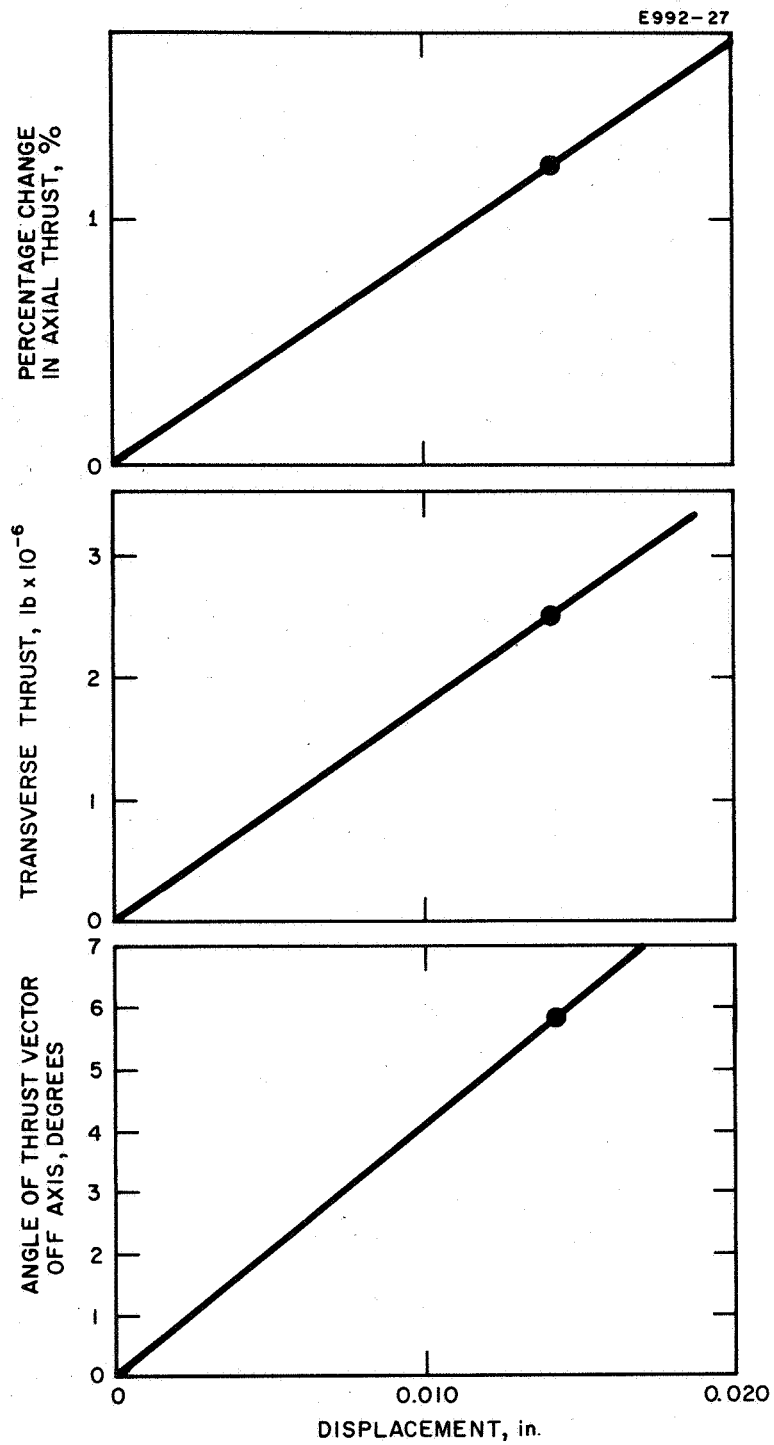
Fig. 16. Change in thrust due to transverse
displacement.

This can be seen if the thrust relations are written

$$T' = \Sigma T_i J_1 \left(\frac{\delta_i + \overline{\delta}_i}{2} \right)$$

and

$$T = \Sigma T_i J_0 \left(\frac{\delta_i + \overline{\delta}_i}{2} \right)$$

where the unperturbed axial thrust is given by ΣT_i. The changes in thrust can then be written

$$\delta T = \Sigma T_i \left\{ 1 - J_0 \left(\frac{\delta_i + \overline{\delta}_i}{2} \right) \right\}$$

$$\delta T' = \Sigma T_i J_1 \left(\frac{\delta_i + \overline{\delta}_i}{2} \right)$$

Recalling that the zero order Bessel function can be written as

$$J_0 \left(\frac{\delta_i + \overline{\delta}_i}{2} \right) \doteq 1 - \frac{1}{4} \left(\frac{\delta_i + \overline{\delta}_i}{2} \right)^2$$

and the first order Bessel function as

$$J_1 \left(\frac{\delta_i + \overline{\delta}_i}{2} \right) \doteq \frac{\delta_i + \overline{\delta}_i}{4} \quad ,$$

We can write

$$\frac{\delta T}{\delta T'} = \frac{\text{change in axial thrust}}{\text{change in transverse thrust}}$$

$$\doteq \frac{1}{4} \frac{\Sigma T_i \left(\delta_i + \overline{\delta}_i\right)^2}{\Sigma T_i \left(\delta_i + \overline{\delta}_i\right)}$$

Since $1/2(\delta_i + \overline{\delta}_i)$ is about 0.3 at maximum,

$$\frac{\delta T'}{\delta T} \geq 6.6 \ .$$

D.   Tilt

Since the engine diameter is 30 cm and the spacing between the screen and accel electrode is 0.090 in., the maximum angle for gross tilt is of the order of $\tan^{-1} 0.007$. This is equivalent to an angle of about 0.4°. (However, localized warping could increase the angle to some extent.) A case has been run with symmetric tilt of 1.5° about the unperturbed center line. This produces a maximum displacement of the accel-electrode of 0.002 in. The results from this run show no significant change in ion optics or emission density. This is in general agreement with the other reported work,[2] where it was found that "for tilt angles of less than 5° no meaningful results could be obtained since the small calculated beam deflection approach the accuracy of the computer program."

However, tilt may be a significant factor at the edge of the engine where the displacement of the accel-electrode can be regarded as a combination of an axial movement and a tilt. In this case a satisfactory solution can be found by considering the appropriate axial displacement alone.

E.   Conclusions

The results obtained can be compared to some extent with those reported in Ref. 2. In that investigation the exact location of the plasma boundaries was not determined for each perturbation, the downstream boundary was not determined, and no axial perturbations were made. However, the results of the ion optics for tilt and transverse displace-ments appear to agree to within approximately 5%. No attempt was made in that work to calculate the total thrust; hence no comparison can be made with the over-all results reported here.

Although the results to date are preliminary in the sense that more accurate knowledge of the change in thrust with the various param-eters would result from additional data, some conclusions can be drawn. If it is assumed that the changes are linear over the range considered, sufficient information is now available to calculate the thrust for any type of perturbation. The change in thrust can then be expressed in terms of the five parameters α, β, γ, η, ω (previously defined) where

$$\alpha = \frac{\delta \text{ (Axial Thrust)}}{\text{Axial Movement}} = -0.000163 \text{ mlb/mil}$$

$$\beta = \frac{\delta \text{ (Axial Thrust)}}{\delta \text{ (Current)}} = 0.01573 \text{ mlb/mA}$$

$$\gamma = \frac{\delta \text{ (Axial Thrust)}}{\text{(Transverse Movement)}} = 0.0000218 \text{ mlb/mil}$$

$$\eta = \frac{\delta \text{ (Transverse Thrust)}}{\text{(Transverse Movement)}} = -0.000178 \text{ mlb/mil}$$

$$\omega = \frac{\delta (\emptyset)}{\text{(Transverse Movement)}} = 0.411 \text{ deg/mil.}$$

III.   CAUSES AND MAGNITUDES OF ELECTRODE
        MISALIGNMENT

A.   Introduction

As described in the previous progress report, the electrode misalignments caused by thermal stresses within the grid system are the most difficult to calculate because they require complicated thermal-stress models of the electron bombardment thruster. We describe below the progress made during this quarter on the analysis of the thermally induced misalignments.

Temperature distributions were measured on a thermal mockup of a bombardment thruster. A schematic drawing of the mockup is shown in Fig. 17. Each spot represents the location of one of the 24 thermocouples. The heat sources were simulated by heating coils located at the front of the anode A, over the remaining anode surface B, and at the cathode position. Ten temperature distributions were measured for various combinations of input heater powers, with the mockup in a vacuum tank. Typical data are also shown in Fig. 17. Attempts to predict these data by using analytical models for the non-reflective radiative transfer were unsuccessful. Upon further consideration of the data (particularly the rather uniform equilibrium temperature distributions across the electrodes), we suspected that a large number of multiple reflections occur inside the discharge chamber; accordingly, the heat flux distribution across the screen electrode is fairly uniform. Since the multiple reflection radiation problem is too difficult for hand calculations, our efforts to calculate the misalignments due to thermal stresses were redirected toward (1) a detailed analysis of the grid system only, and the assumption of various incident heat flux distributions from the discharge chamber; (2) consideration of only the most noticeable thermal misalignment, the warping of electrodes in operating engines.

39

303°C
258
226

303
258
228

293
232
224

224
207
186

293
230
222

280 220
220 205
211 184

403°C
348
311

397
348
311

403
348
309
317

403
348

387 414
332 358
293 315

504W
333
220

HEATER A

673
580
498

536°C
465
421

HEATER B

80W
80
80

495°C
412
379

484
403
371

213
184

207 165
174
165

328
280
254

491
410
375

276
242
224

108W
102
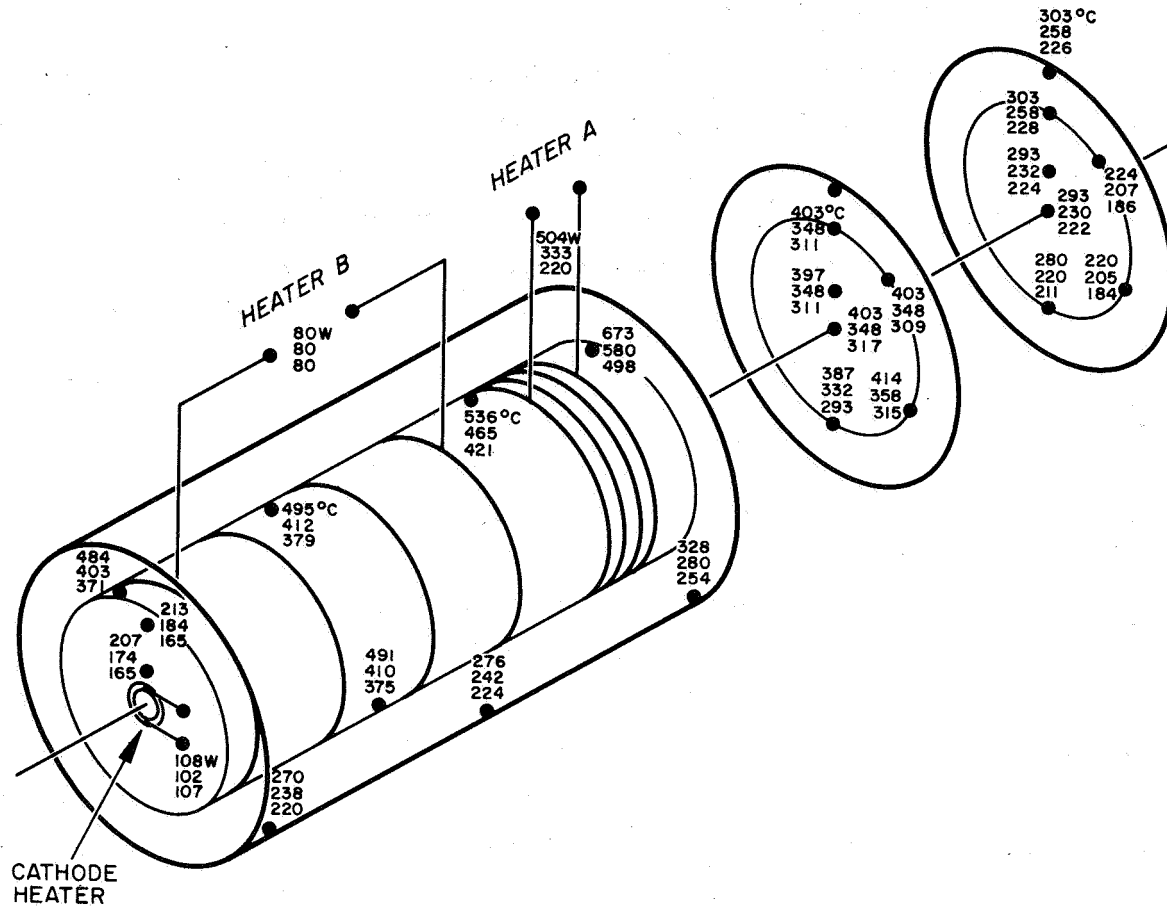107

270
238
220

CATHODE
HEATER

Fig. 17. Thermal mockup of electron bombardment thruster.

40

A serious difficulty which arises in modeling electrode warping is that the thermal and stress models employed should be general enough to govern a wide variety of electrode designs. For example, it is desirable that the models include electrodes of different diameters, thicknesses, and open areas which may also be tapered, initially dished, and clamped in the center and on the edges in various ways. A modeling technique which lends itself to this electrode warping analysis is to use general but versatile computer simulation programs. The HAC library of computer programs was studied, and two programs were selected which will greatly facilitate the thermal-stress modeling. The first is a heat transfer analysis program (TAS-1B) which will be used to solve for the temperature distributions and heat flows in the grid system. TAS-1B is a digital computer program which solves for the steady-state temperature distribution in a lumped parameter network of temperature points (nodes) and heat flow paths (resistors). A node is provided for each constant temperature portion of the device being modeled. The network may contain up to 80 nodes and each node may be connected to any or all of the others. Any two nodes may be connected by two resistors. One represents conduction and/or convection; the other represents infrared radiation. TAS-1B does not account for the temperature dependence of thermal properties, and thus heat flows due to conduction and convection are linear with respect to node temperatures. Infrared radiation is not linear because it depends on the fourth powers of the absolute temperature. Any two nodes may be connected by a linear resistor, a radiation resistor, or both. In addition to interchanging heat with other nodes, each node may receive radiation and/or a direct heat input (such as from internal dissipation of electrical energy); TAS-1B does not permit a node to produce a direct heat output.

The second computer program[3] chosen analyzes the structure of shells using a finite element method. Shells of revolution subject to axisymmetric or asymmetric mechanical and thermal loads can be

handled. This program will be used to study the warping of the electrodes. An electrode is divided into washer shaped regions which form the elements of the model. Thermal and mechanical loads are prescribed on each element and the computer program solves the equations of motions for the deformations. Since the dimensions of each element can be specified independently, initially dished and tapered electrodes can be considered.

Because the stress analysis program considers solid plates, a literature search was conducted to determine whether an equivalent set of thermal and elastic parameters could be used in the solid plate analysis in order to simulate the actual punched plate electrode. It was found that such an equivalence is possible and has been used in the analysis.

The analysis of electrode misalignment as a result of the thermal warping of the electrodes consists of first determining the radial temperature distributions on each electrode and next calculating the warping produced by the thermal stresses. A detailed discussion of each of these tasks will now be given.

B.   Thermal Simulation of the Grid System

   1.   Network Model

       A thermal model of the grid system was developed in the form of a network of nodes, each of which corresponds to a constant temperature region on an electrode. For axisymmetric heating the nodes N_i and N_i' are washer shaped (annuli) regions on the electrodes (see Fig. 18). Heat is transferred between adjacent washers of each electrode by conduction and between opposite washers of the two electrodes by radiation. An additional constant temperature node N_B, which represents the background, absorbs heat radiated directly from the accelerator electrode and from screen electrode by way of the holes in the accelerator electrode. The heat input to the grid system from the discharge chamber is represented by a distribution of black body radiation which is incident on screen electrode and varies radially

42
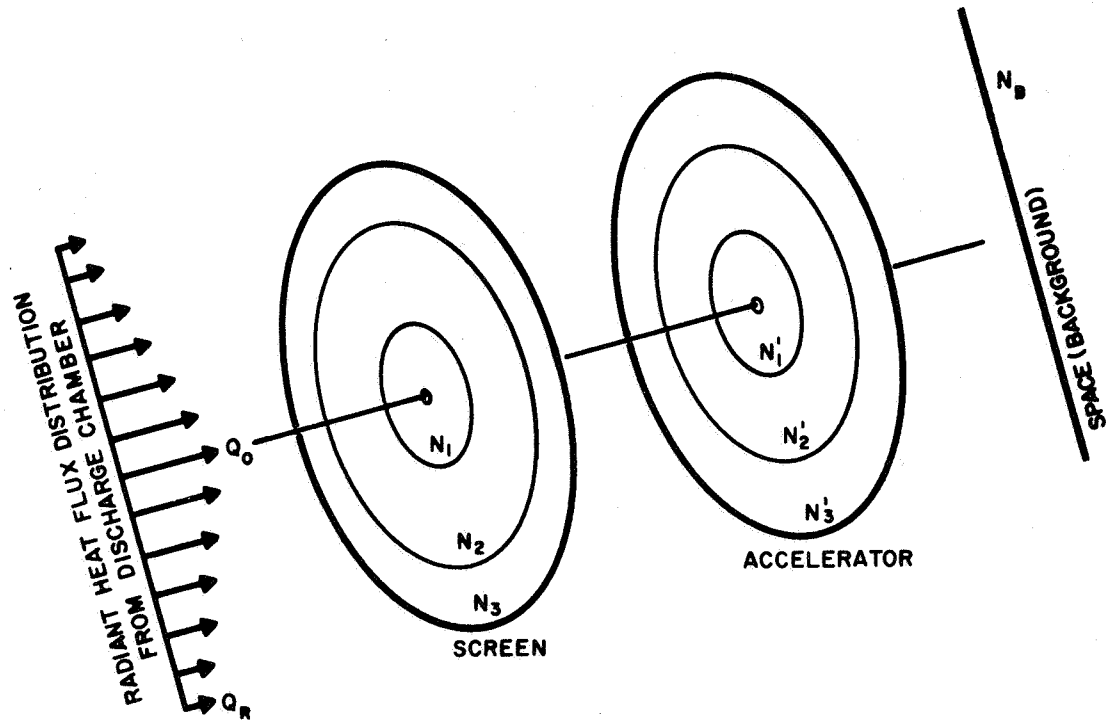
Fig. 18.   Model for electrode thermal analysis.

in intensity. The thermal network corresponding to this model is shown in Fig. 19. The node N_B is fixed at a constant temperature ($0^{\circ}F$ in our examples) and is assumed to be a black body ($\epsilon = 1$) whose area is much larger than any other node. Under these assumptions N_B may be regarded as a heat sink. For given values of incident heat flux Q_i, the temperatures of the other nodes N_i, N_i' can be calculated once the node coupling by the conductance paths $C(i, j)$ and radiation paths $R(i, j)$ is established. The evaluation of the thermal conductivities between the nodes of the model is straightforward and will be considered first. The evaluation of the geometric (view) factors which govern the radiative heat transfer in the model is more complicated and will receive a more lengthy discussion. The results of node temperature calculations for four cases of electrode geometry will then be given.

a.   Heat Conductance in the Electrodes — The temperature of a (washer shaped) node on an electrode shown in Fig. 20(a) will be taken as the value of the temperature at the circle halfway between the edges of the washer. Thus, the temperatures of nodes N_1, N_2, and N_3 are taken at the locations R_1, R_2, and R_3. The thermal conductance between nodes N_i and $N_i + 1$ is then equal to the conductance between the inside and outside edges of the washer shown in Fig. 20(b). The formula for this conductance is

$$C_{i, i+1} = \frac{2\pi t K'}{\log \frac{R_{i+1}}{R_i}}$$

where

$$t \equiv \text{thickness of the washer}$$
$$K' \equiv \text{thermal conductivity of the washer.}$$

44

Fig. 19. Thermal network for grid system.

(a)

(b)

Fig. 20.
Heat conduction between an-
nular regions.

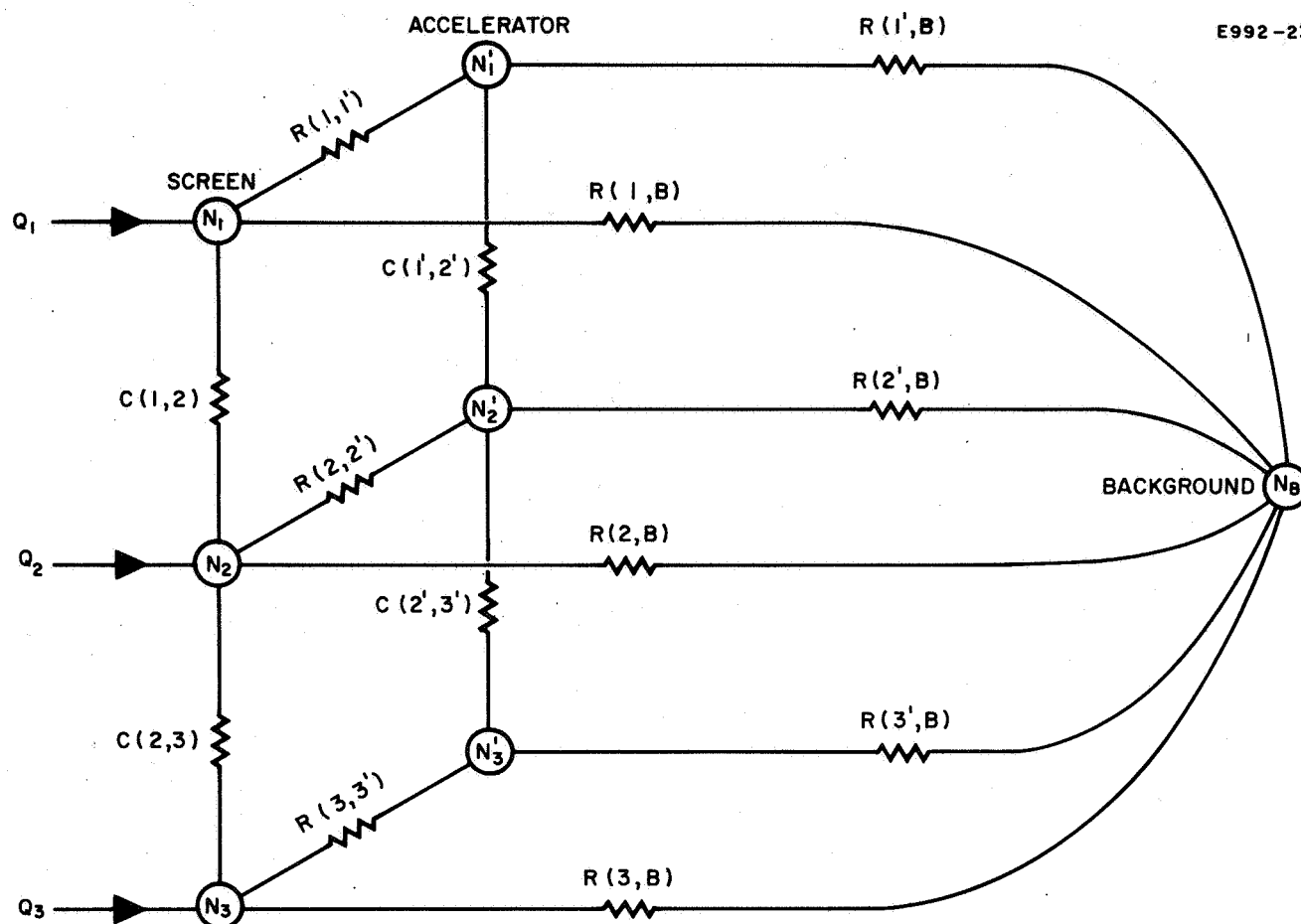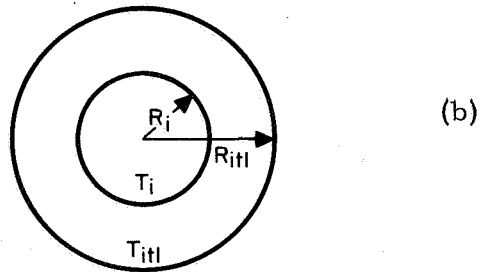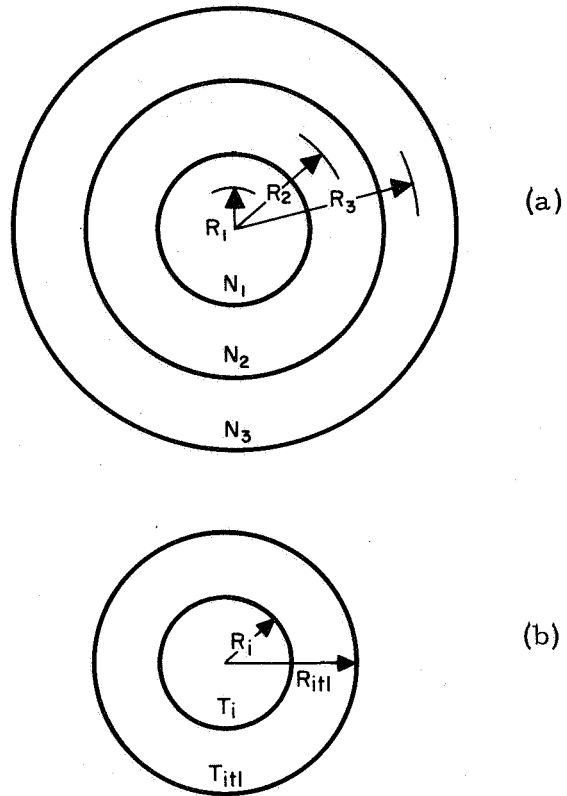For a perforated plate of open area fraction f and material thermal conductivity K, we take $K' = (1 - f) K$.

b.   View Factors for Radiative Heat Transfer in the Grid System — Because of the small spacing between the electrodes relative to the radii of the annular nodes (see Fig. 18), it is reasonable to assume that radiative heat transfer occurs between only the directly opposing nodes (i.e., between N_i and N_i'). Under this assumption the desired view factors for the grid system can be calculated on the basis of two infinite parallel perforated plates. The geometry of a cross section of two aligned perforated plates S and A is shown in Fig. 21. The nodes for which view factors are to be calculated are indicated by the numbers 1 through 7. The actual calculations are carried out in Appendix II; because of their complexity, approximations are made. The nodes 1 through 6 describe in detail the coupling between each set of nodes (N_i, N_i'). The over-all detailed network for the grid system has three sets of six nodes each, as shown in Fig. 22.

The heat incident on the screen electrode is first divided (into Q_1, Q_2, and Q_3) between the three nodes N_1, N_2, and N_3. A radial heat flux distribution is assumed which varies linearly between Q_o at the center of the screen and Q_R at the edge. The heat components Q_i are then split into $(1 - f_s)Q_i$ (input to the material surface of N_i (node 3)) and $f_s Q_i$ (input to the open surface area of N_i (node 1)). Here f_s is the open area fraction of the screen. In the heat transfer calculations it is assumed that node 1 is a black body ($\epsilon = 1$).

2.   Examples of Grid System Temperature Calculations

The computer program TAS-1B was used to calculate the temperatures and heat flows in the network model shown in Fig. 22. The areas, thermal conductivities, and power inputs to the nodes are shown in Table II. These values correspond to the following electrode geometry:
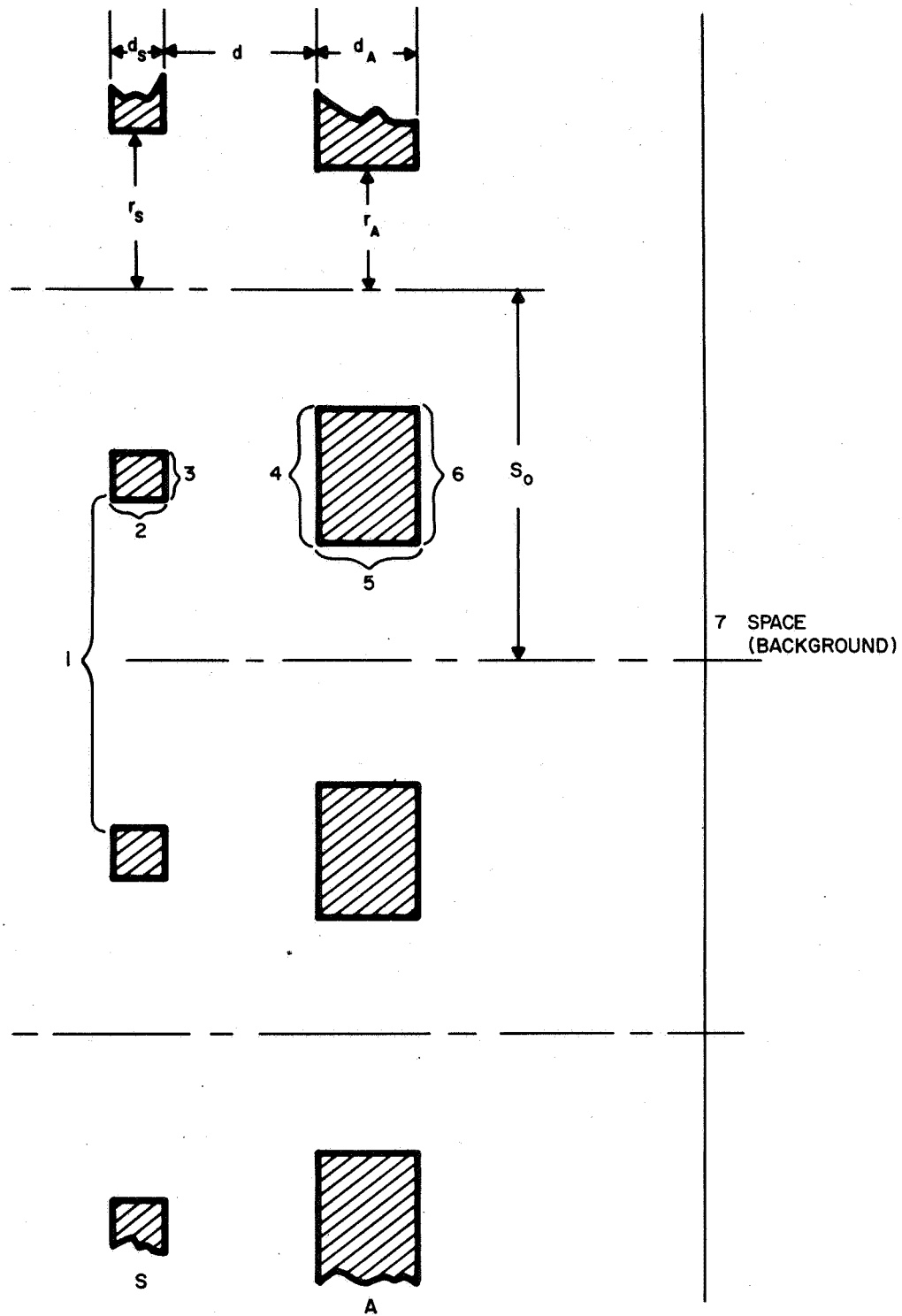
Fig. 21. Cross section of parallel perforated plates.
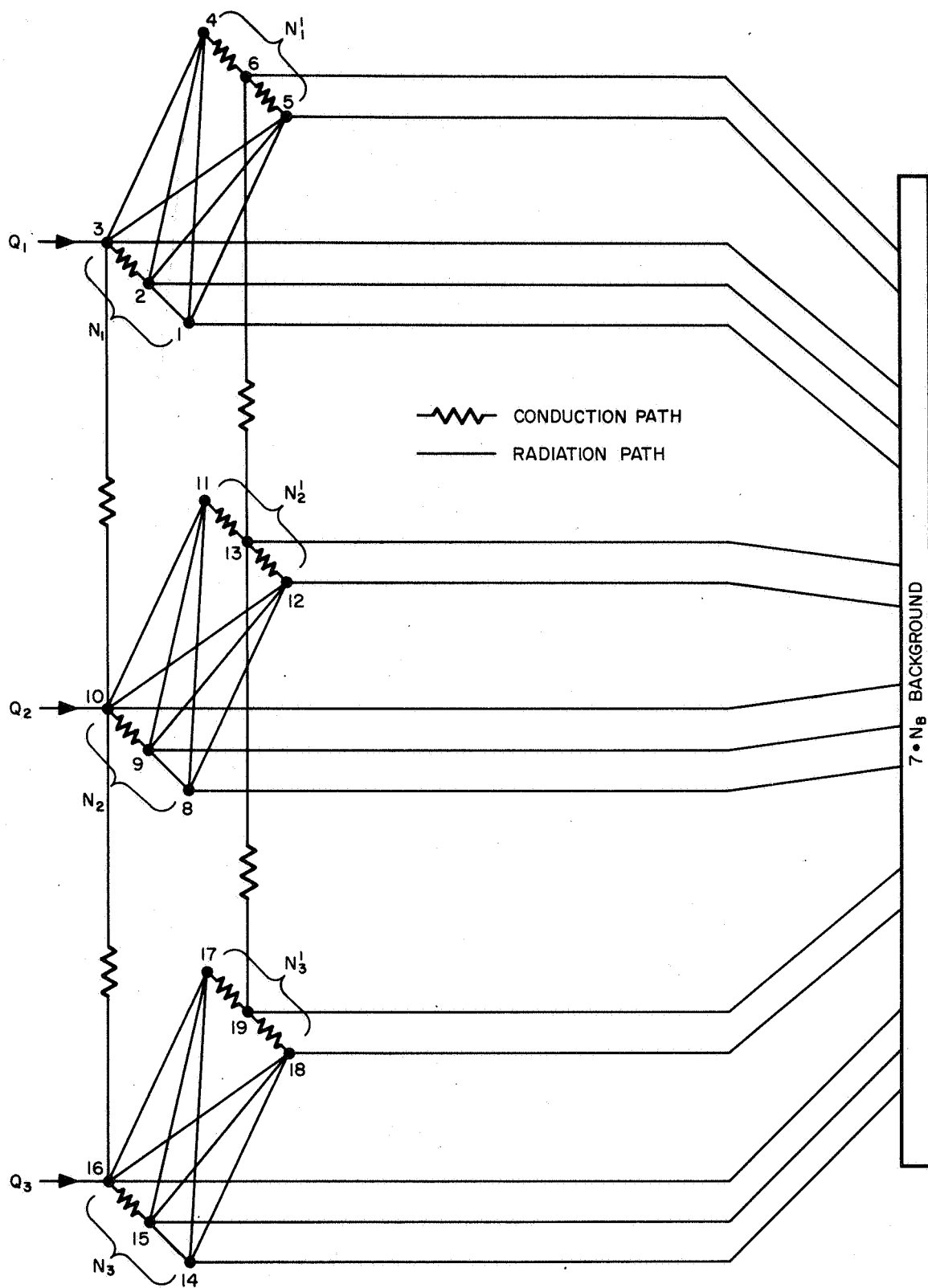
Fig. 22. Detailed thermal network for grid system.

TABLE II

Nodal Areas, Power Inputs, and Thermal Conductivities

Areas, in.^{2}		Power Inputs, W	
A_1	8.55	Q_1	14
A_2	5.50	Q_3	6
A_3	3.55	Q_8	35
A_4	7.30	Q_{10}	15
A_5	8.25	Q_{14}	56
A_6	7.30	Q_{16}	24
A_7	10^7	**Thermal Conductivities, W/$^\circ$C**	
A_8	25.6		
A_9	16.4	$C_{3,10}$	0.050
A_{10}	10.8	$C_{10,16}$	0.109
A_{11}	21.6	$C_{6,13}$	0.207
A_{12}	24.6	$C_{13,19}$	0.443
A_{13}	21.6		
A_{14}	43.0	$C^a_{2,3} = C_{9,10} = C_{15,16} = C_{4,5} =$	
A_{15}	27.5	$C_{17,18} = C_{5,6} = C_{12,13} =$	
A_{16}	17.8		
A_{17}	36.2	$C_{18,19} = 10^6 \dfrac{\text{watt}}{^\circ\text{C}}$	
A_{18}	41.7		
A_{19}	36.2		

[a]Instead of calculating the very high conductances between these nodes, we insured that they arrive at equal temperatures by coupling them with very high conductances.

	Screen	Accelerator
Diameter	30 cm	30 cm
Thickness	0.030 in.	0.060 in.
Open area	70%	40%
Hole diameter	0.187 in.	0.142 in.
Hole spacing	0.213 in.	0.213 in.

Three values of electrode spacing were considered: 0.090 in., 0.070 in., and 0.050 in. The corresponding view factors were found using the formulas in Appendix II and are given in Table III. In all cases the total heat input from the discharge chamber is 150 W, which varies linearly in the ratio $Q_o:Q_R = 1.25:1$ from center to edge.

The six solid curves in Fig. 23 give the screen and accelerator electrode temperatures for the three values of spacing. As shown, decreasing the interelectrode spacing lowers the over-all temperatures of both electrodes. Apparently, the grid system appears more transparent to the incident radiation as the electrode spacing decreases. Since the actual decrease in temperatures is small and the temperature gradients across the electrodes remain unchanged as the spacing varies, the assumption that the grid system temperature distributions can be calculated independently from the thermal-warping is substantiated.

A detailed breakdown of the heat flow between the electrodes and the background is shown in Fig. 24 for a spacing of 0.090 in. In addition to the 150 W input from the discharge chamber, an additional 2 W of interception power has been put directly into the center node N_1' of the accelerator. The increased temperatures of both electrodes are shown by the dashed curves in Fig. 23. Of the 150 W incident on the screen electrode, a total of 41 W after all reflections is absorbed by the accelerator and then reradiated to the background. The remaining 109 W goes to space either directly through the holes or after several reflections. Heat transfer by conduction in the electrodes is indicated by the radially pointing arrows. The quantities indicated are the amounts of heat which are conducted between the annular node regions

51
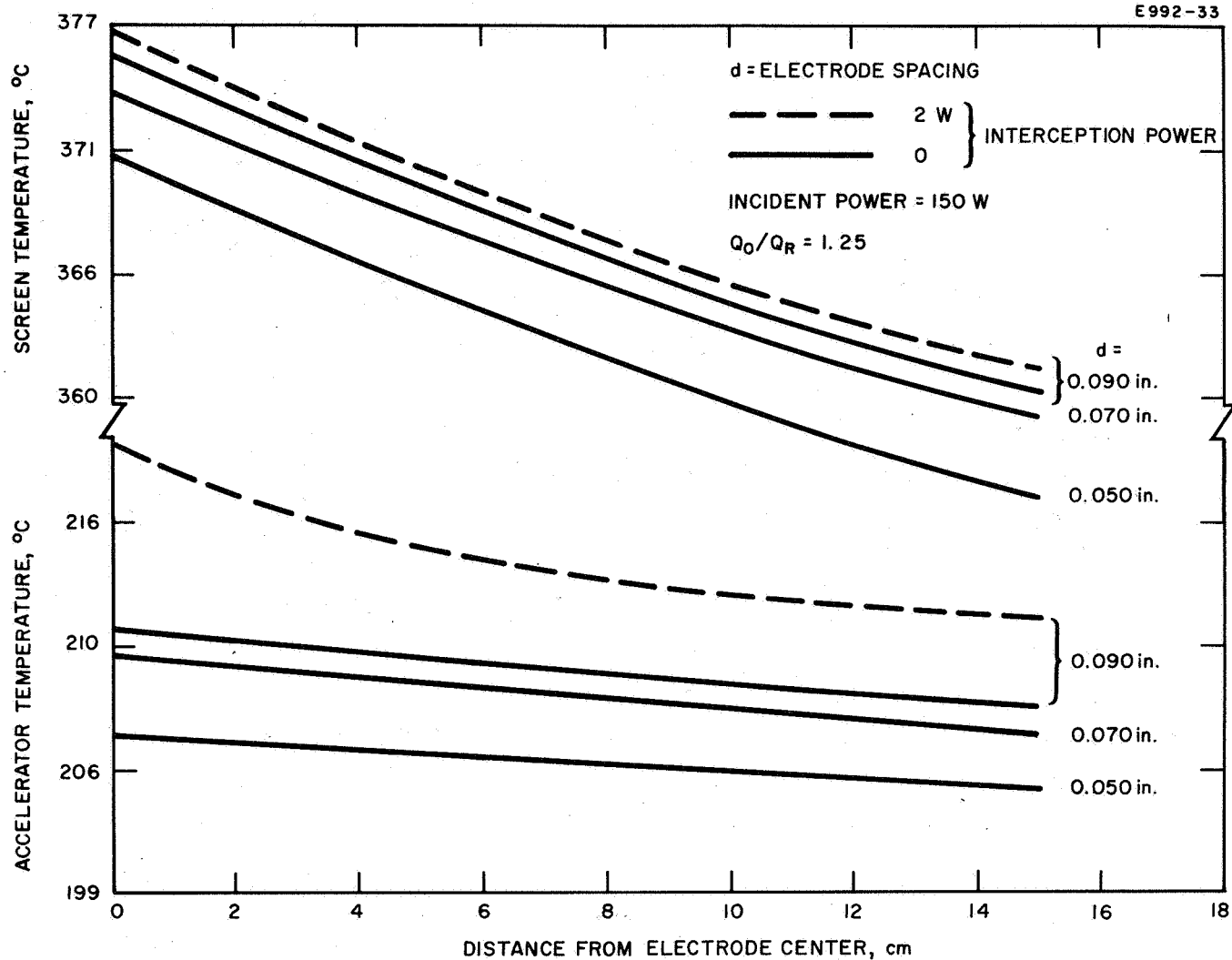
Fig. 23. Grid system temperature distributions.
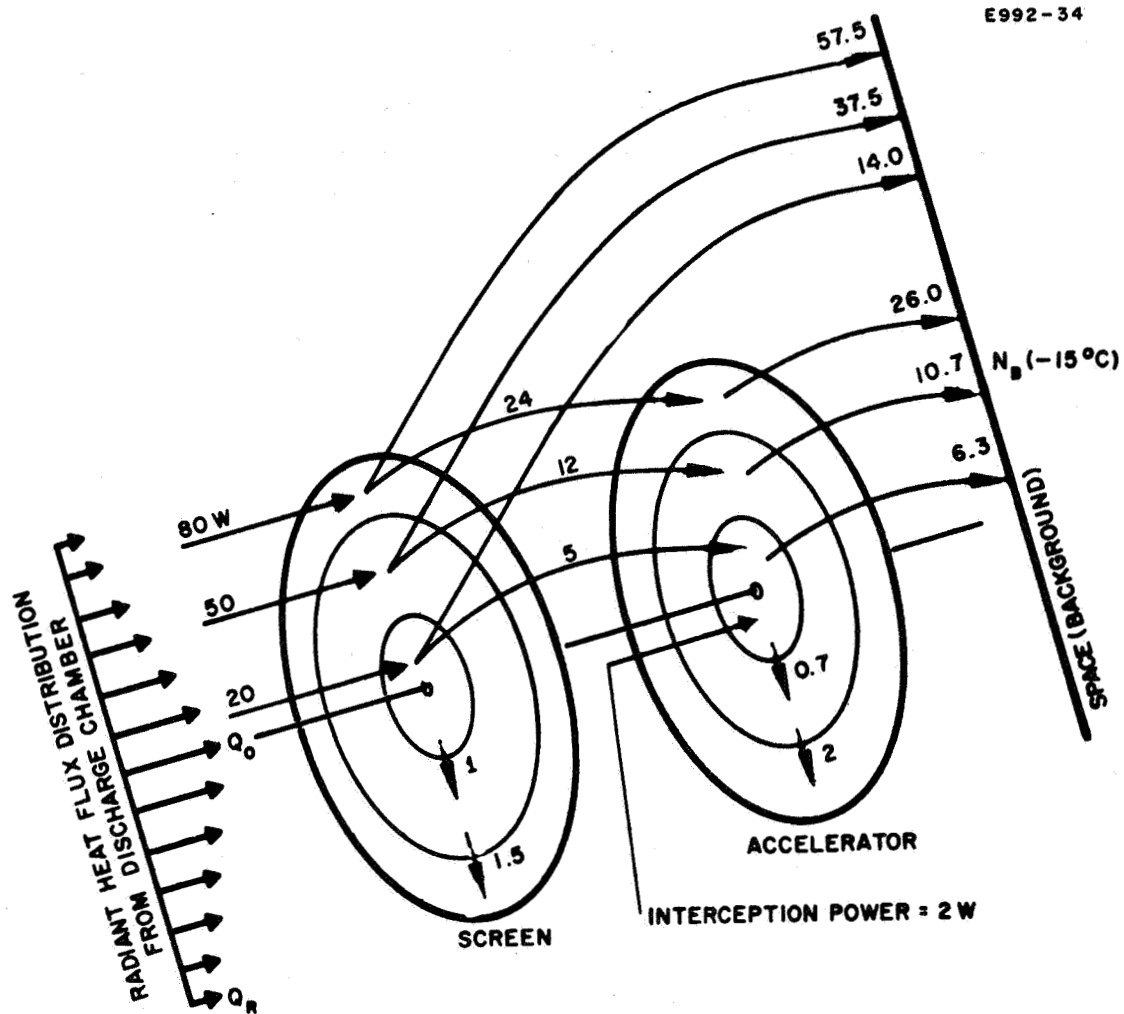
Fig. 24. Heat flow paths in the grid system.

TABLE III

Grid System View Factors

	Electrode Spacing		
	0.90 in.	0.070 in.	0.050 in.
$F_{1,2}$ = $F_{8,9}$ = $F_{14,15}$	0.27	0.27	0.27
$F_{1,4}$ = $F_{8,11}$ = $F_{14,17}$	0.32	0.35	0.33
$F_{1,5}$ = $F_{8,12}$ = $F_{14,18}$	0.14	0.16	0.17
$F_{1,7}$ = $F_{8,7}$ = $F_{14,7}$	0.21	0.22	0.23
$F_{2,2}$ = $F_{9,9}$ = $F_{15,15}$	0.15	0.15	0.15
$F_{2,4}$ = $F_{9,11}$ = $F_{15,17}$	0.31	0.29	0.26
$F_{2,5}$ = $F_{9,12}$ = $F_{15,18}$	0.05	0.07	0.09
$F_{2,7}$ = $F_{9,7}$ = $F_{15,7}$	0.05	0.06	0.08
$F_{3,4}$ = $F_{10,11}$ = $F_{16,17}$	0.60	0.68	0.75
$F_{3,5}$ = $F_{10,12}$ = $F_{16,18}$	0.3	0.26	0.21
$F_{3,7}$ = $F_{10,7}$ = $F_{16,7}$	0.1	0.06	0.04
$F_{5,5}$ = $F_{12,12}$ = $F_{18,18}$	0.34	0.34	0.34
$F_{5,7}$ = $F_{12,7}$ = $F_{18,17}$	0.33	0.33	0.33
$F_{6,7}$ = $F_{13,7}$ = $F_{14,7}$	1.0	1.0	1.0

(e.g., between N_1 and N_2). As shown, thermal conduction in the electrodes is small compared with the radiative transfer.

C.   Stress Analysis of Electrodes at Operating Temperature

In Section III-B a thermal model of the grid system was developed for predicting the temperatures of the electrodes under normal (unperturbed alignment) operating conditions. Since the current practice is to align the electrodes precisely during assembly, at room temperature, the differences between the electrode operating temperatures and room temperature represent thermal-stress producing temperature gradients. We believe that the stresses produced as the grid system undergoes heating to operating temperature produce the largest axisymmetric misalignments which are likely to occur. A significant effort has therefore been devoted to predicting these misalignments quantitatively. Although it is the natural next step, the extension of our analysis to cover misalignments resulting from non-axisymmetric thermal stresses is too time consuming and expensive for the Phase I study. We will only note here that this problem is of concern for operating thrusters in an array.

We now discuss example calculations of axisymmetric warping. The remaining causes of misalignment (due to assembly errors and mechanical vibrations) are not axisymmetric and will be analyzed in a later report.

The warping of the screen and accelerator electrodes was calculated for the highest (dashed) temperature profiles in Fig. 23. Equivalent values of elastic constants for the perforated plates, inferred from the paper by O'Donnell and Langer,[4] are the following:

	Young's Modulus (%/$^\circ$F)	Poisson Ratio
Screen	2.15 x 10^6	0.7
Accelerator	10.8 x 10^6	0.36

The resulting axial and radial displacements of the electrodes are shown in Fig. 25. Both electrodes were almost flat (0.004 in. rise) initially. The rather large radial displacements occurred because no clamping forces caused by the supports were included. The presence of such forces will reduce the radial displacements and in turn reduce the transverse misalignment, but will also increase the axial deflection (bowing). An example of this situation will be studied in the next reporting period.

D.   Analysis of Electrode Supports

Thermal and mechanical analyses of the electrode supports are required to determine whether they contribute significantly as a heat transfer path in the thermal model and/or as a boundary constraint in the stress model. To evaluate their importance, the thermal resistance and clamping forces of the supports will be estimated. These effects will then be included in an electrode warping calculation. If significant changes in the amounts of warping occur, the support properties will be studied in more detail. The thermal resistance of supports is calculated below. The mechanical analysis will be done in the next reporting period.

A schematic of a typical electrode support considered in this analysis is shown in Fig. 26. The equivalent heat paths for this assembly are shown in Fig. 27. We see from this figure that the direct heat path through the top insulator to the supporting bracket is paralleled by the heat path composed of the series resistance of the bottom insulator and the clamping screw. The thermal resistance of each component will be approximated by the one-dimensional thermal resistance formula

$$R = \ell/kA \qquad\qquad (32)$$
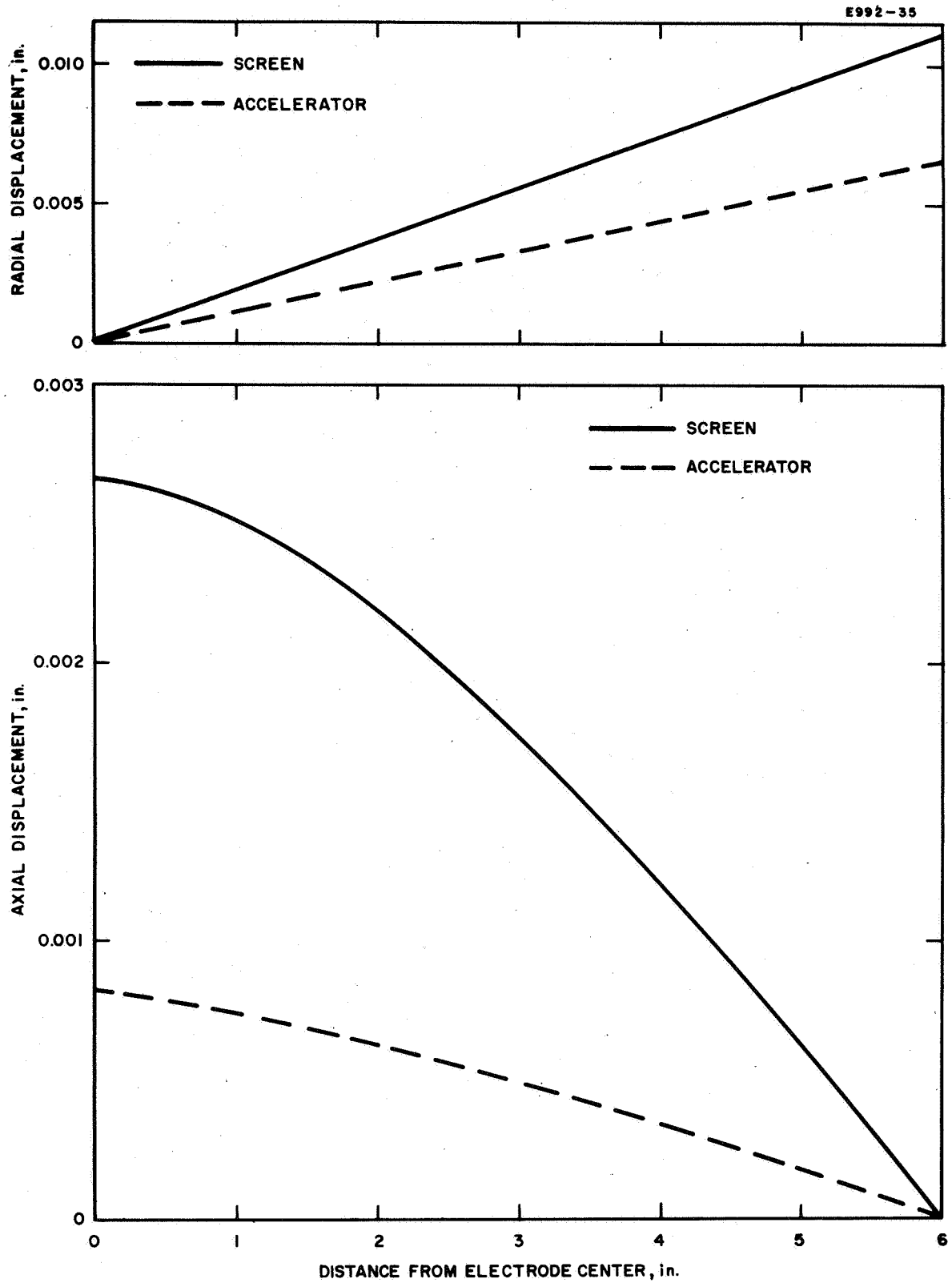
Fig. 25. Thermal warping of electrodes.
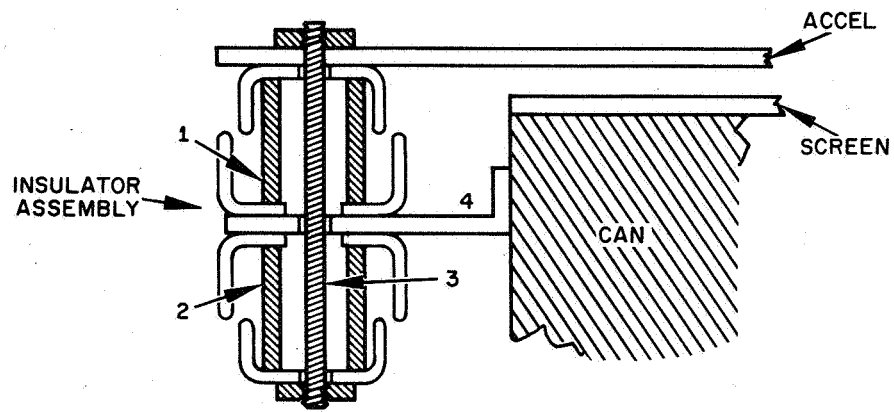
Fig. 26. Schematic of typical insulator assembly.
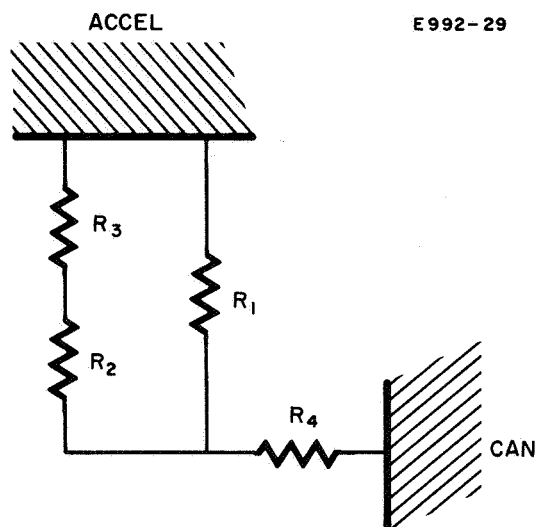
Fig. 27. Equivalent thermal re-
sistance paths of insula-
tor assembly.

where

$$\ell \equiv \text{length of thermal path (cm)}$$
$$A \equiv \text{cross sectional area (cm}^2)$$
$$k \equiv \text{thermal conductivity (W/cm-}^\circ\text{C)} .$$

For the insulators considered

$$A = 0.395 \text{ cm}^2 = \pi/4 \ [(0.95)^2 - (0.635)^2]$$
$$\ell = 1.59 \text{ cm}$$
$$k \cong 0.05 \text{ W/cm-}^\circ\text{C (Al 300 ceramic)}$$

and

$$R_1 = R_2 = \frac{1.59}{(0.05)(1.59)} = 80.6 \ ^\circ\text{C/W} . \qquad (33)$$

For the stainless steel clamping rod

$$A = 0.0964 \text{ cm}^2 = \pi/4 \ (0.35)^2$$
$$\ell = 3.76 \text{ cm}$$
$$k = 0.16 \text{ W/cm} \ ^\circ\text{C}$$

and

$$R_3 = \frac{3.76}{(0.16)\ (0.0964)} = 244 \ ^\circ\text{C/W} . \qquad (34)$$

Finally, for the stainless steel supporting bracket

$$A = 0.31 \text{ cm}^2 = (0.122)\ (2.54)$$
$$\ell = 1 \text{ cm}$$
$$k = 0.16 \text{ W/cm} - \ ^\circ\text{C}$$

and

$$R_4 = \frac{1}{(0.16)(0.31)} = 20.2\ ^{\circ}C/W \quad . \tag{35}$$

Inspection of Fig. 27 indicates that an equivalent thermal resistance of the complete assembly can be written in terms of the individual thermal resistances according to the relationship

$$R = R_4 + \left(\frac{1}{R_1} + \frac{1}{R_2 + R_3}\right)^{-1}$$

$$= 20.2 + \left[\frac{1}{80.6} + \frac{1}{80.6 + 244}\right]^{-1}$$

$$= 84.6\ ^{\circ}C/W \text{ (per insulator assembly)} \quad . \tag{36}$$

Since there are six insulator-support assemblies per engine module, the total thermal resistance between the accelerator and the can is

$$R_{total} = \frac{1}{6}\ (84.6) = 14.1\ ^{\circ}C/W \quad . \tag{37}$$

E.   Integration of Misalignment and Ion Optical Results

From the examples of warping given above and a consideration of the ion optical results (Section II), some indications of the behavior of the grid system as it is heated to operating temperature, and the corresponding effects on the thrust vector, can be obtained. These effects are summarized by the following qualitative observations. When an aligned grid system (initially at room temperature) is heated to operating temperature:

60

1. Radial and axial displacements of both electrodes will occur.

2. Both displacements will be greater for the screen because it becomes hotter with a larger temperature gradient, has a larger open area, and is thinner than the accelerator electrode.

3. The misalignments which result from the above displacements are (a) a decrease in the electrode spacing, and (b) a transverse (radially outward) motion of the screen holes with respect to the accelerator holes.

4. The misalignments 3(a) and 3(b) will cause a decrease in beam current and axisymmetric beam divergence for an ideal operating thruster.

5. The magnitude of the decrease in spacing resulting from bowing of both electrodes is most dependent on the temperature gradients; the magnitudes of the radial displacements depend on the over-all temperature levels of the electrodes.

6. The relative amounts of radial and axial displacements which occur in an individual electrode depend strongly on the radial clamping forces by the supports at the electrode edge.

For the case considered in Fig. 25 (including 2 W interception power, without radial constraint due to clamping), the maximum change in axial spacing between screen and accel electrodes was found to be about 0.002 in. (at the center). The maximum transverse displacement difference (between screen and accel electrodes) was 0.0046 in.

These data can be used, together with the linear coefficients found in the ion optics study, to yield the change in axial thrust of a center hole only: $\Delta T = j \times -0.002$ in. $= +0.0044 \times 10^{-5}$ lb and rotation of thrust vector of the outer levels (outward) by $w \times 0.0046$ in. $= 1.9^{\circ}$. These data are furnished for illustrative purposes only; during the next quarter the results of the ion optics and electrode displacement studies will be combined for the entire thruster.

IV.   THRUSTER DESIGN

As discussed in the last quarterly report, the thruster proposed for this task is basically a SERT-II thruster scaled to 30 cm diameter. Early in the program a layout was made and used as the basis for the thermal analysis. The construction techniques, estimated component weights, and general structural design have subsequently been confirmed in a company funded program to fabricate and test a hollow cathode thruster of similar size and design. No further design effort was made during this quarter.

It is scheduled that the thruster design be reevaluated in the final quarter of the contract and that the final design and construction details be worked out at that time. This will permit full use of experience gained on related programs and the performance reported in the literature for similar thrusters. Tentative design modifications may include incorporation of throughfeed rather than reverse feed and shortening of the discharge chamber to approximately the length of the 15 cm SERT-II thruster rather than direct scaling (as was done in the preliminary design).

V. INSTRUMENTATION

A. Thrust Stand[*]

A number of techniques potentially useful for measuring the thrust direction were investigated and reported in the last quarterly report. A system consisting of a table freely floating in a mercury pool appeared the most promising. It is capable of measuring the thrust direction, its point of application, and any torque about the thrust axis. This system, which is described below, has been analyzed in considerable detail during this quarter to establish its sensitivity, stability, optimum configuration, and over-all utility for the task at hand. Some of the elementary features of the system were discussed in the last report but are repeated below in order to provide a complete description in one place.

1. System Description

This concept uses a suspension mechanism which permits the three components of the thrust and the torques about the three mutually perpendicular axes to be measured[**] at the same time. The thruster platform is floated in a mercury pool and is free to drift horizontally or to lean away from the vertical, depending on forces applied. It is also possible for the system to rotate about its vertical axis if a couple exists about this axis. As discussed below, the suspension must be carefully designed to assure stability and to assure that the suspension itself introduces minimum perturbations into the system.

The operation of the system may be understood by referring to Fig. 28, which shows a two dimensional sketch of the essential elements of the device, and Fig. 29, which illustrates the two types of thrust misalignment which may occur. The mercury surface remains horizontal,

---

[*] This section was prepared by D. Berman and J. D. Smith.
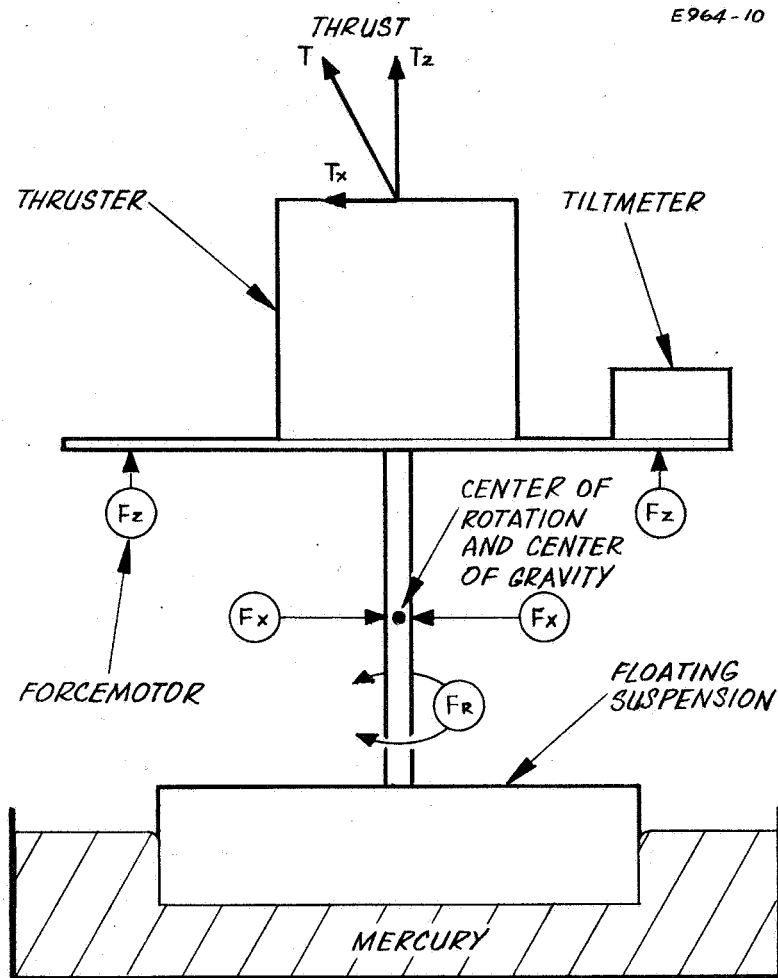[**] The total thrust is calculated from electrical measurements.
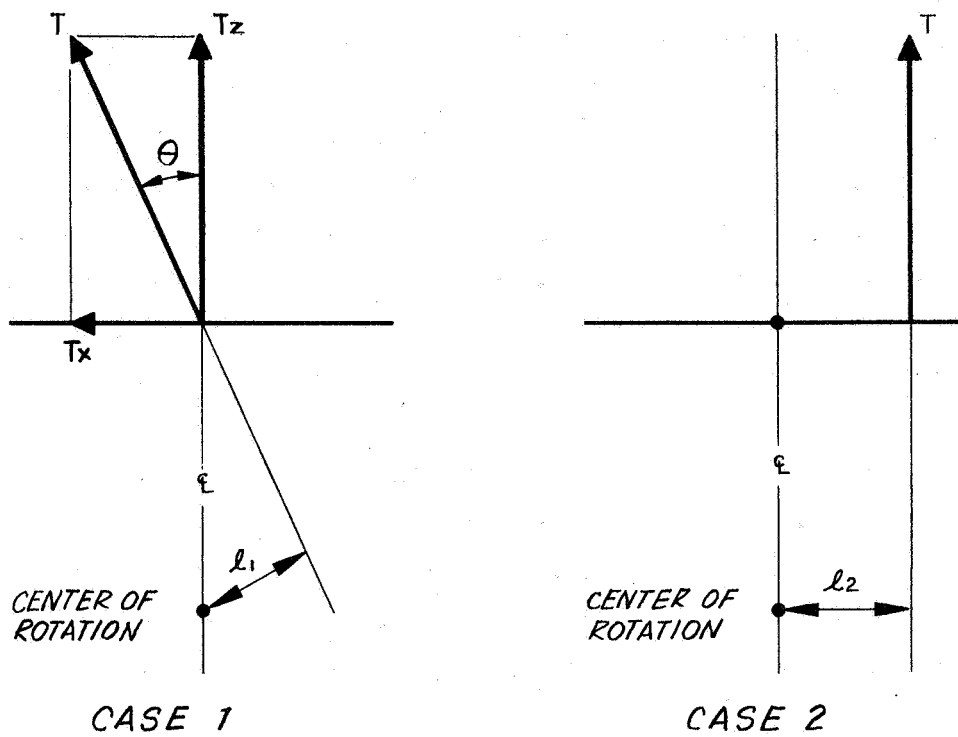
Fig. 28. Sketch of floating suspension device.

Fig. 29. Two types of thrust misalignment.

thus removing the necessity of placing the entire apparatus on a stable table, as in the previous design. In operation the table is releveled by the force motors F_z, using the tiltmeter as a reference, while horizontal and rotational motion is arrested by the force motors F_x and F_r, respectively. The position monitors which establish these null positions are not shown.

Consider first case 1 of Fig. 29. Here the thrust vector is at an angle θ with the desired direction along the centerline. It is apparent that such a force tends both to tilt the platform and to move it horizontally. To resolve such a force, force motors F_z level the platform and the force motor F_x compensates for the horizontal drift. Next, consider case 2 of the same figure, which illustrates a situation in which the thrust vector has moved laterally while remaining parallel to the centerline. Notice that if $\ell_1 = \ell_2$, the same torque is produced about the center of rotation, as in case 1. However, there is no lateral force in the second case.

The primary advantages of the floating suspension are (1) that it resolves the two possible types of thrust misalignment illustrated in Fig. 29 and (2) that a single experimental setup measures both angular deflections of the thrust vector and torques set up about the centerline or nominal thrust axis. Figure 30 illustrates the proposed suspension mechanism which provides the additional degrees of freedom.

It is desirable to design the floating suspension system so that the buoyant force of the mercury supports the platform but does not tend to force it to maintain a particular position. In other words, by proper mechanical design the system may be made critically stable so that the buoyant forces tend neither to right it or to upset it. The design criteria which define such a neutral system were described in the previous quarterly report.

The preliminary design of the system incorporated a bubble sensor, such as is used as the sensing mechanism on the HAC tiltmeter, to sense the table position with respect to the horizontal. It was subsequently recognized that it is not necessary to maintain the table
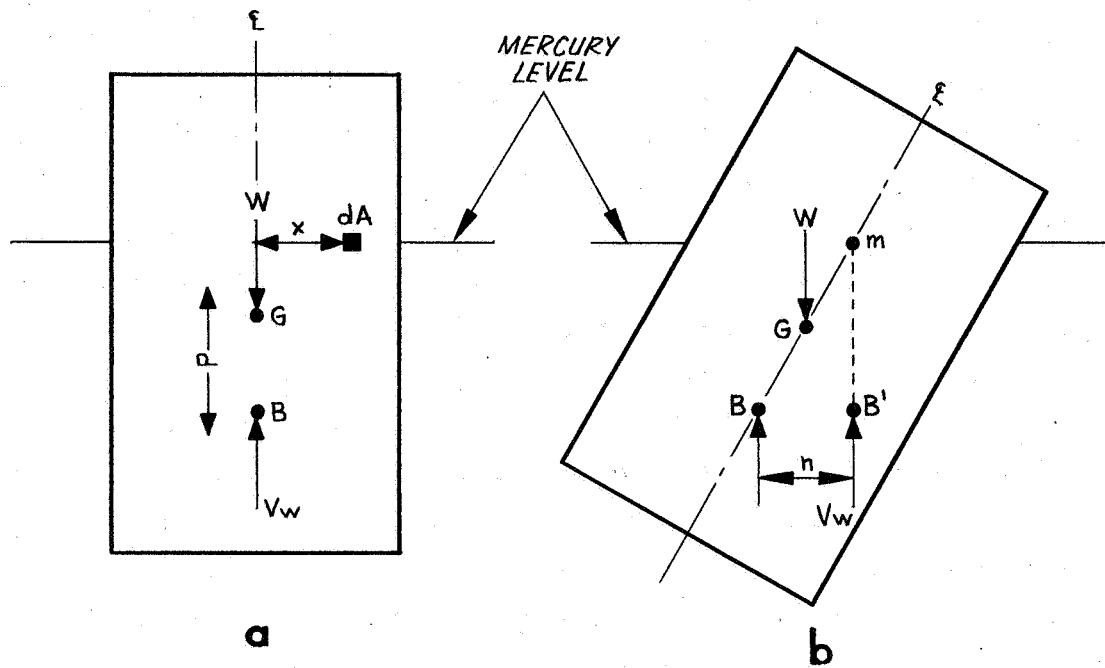
Fig. 30. Proposed suspension system.

accurately horizontal at the null position when the neutrally stable suspension described above is achieved. By using linear position sensors referenced to the platform supporting the mercury reservoir to monitor the motion of the floating table in the vertical (z) as well as the horizontal (x, y) plane, the dynamic control system is greatly simplified and made unconditionally stable. Both systems are described and compared in the following discussion.

As shown in Fig. 31, the several components of thrust and torque are balanced by a combination of eight force motors; four are aligned with the vertical axis z, positioned in a plane symmetrically, and four are aligned in the horizontal plane. It will be demonstrated below that this arrangement is adequate to determine the thrust deflection and torque by algebraic manipulation of the static force motor readings.

The vertical force motors are intended only to balance torque about an axis in the horizontal plane (x, y). The main thrust (along the z-direction — vertical) is obtained from measurement of the ion engine beam current and voltage; thus z-motion is unimportant. Therefore, these four force motors are operated as series pairs such that the two always produce an equal and opposite force. This gives the required torque with no net z force.

The horizontal force motors must balance torque about the vertical (z) axis and translational thrust components in the x-y plane. Therefore, the opposite horizontal force motors cannot be paired to always produce an equal and opposite force because they must produce a net balancing force in addition to the torque.

Figure 32 shows the transducer and force motor control arrangement for the five degrees of freedom of interest. The β_x and β_y rotations are sensed by the (two-axis) bubble sensor or by four linear transducers. These signals drive the four vertical motors in matched pairs. The rotation about the vertical axis and the translation in the x-y plane cannot be sensed independently. This coupled motion is observed by four photoelectric transducers, which sense the net x-y motion of a point
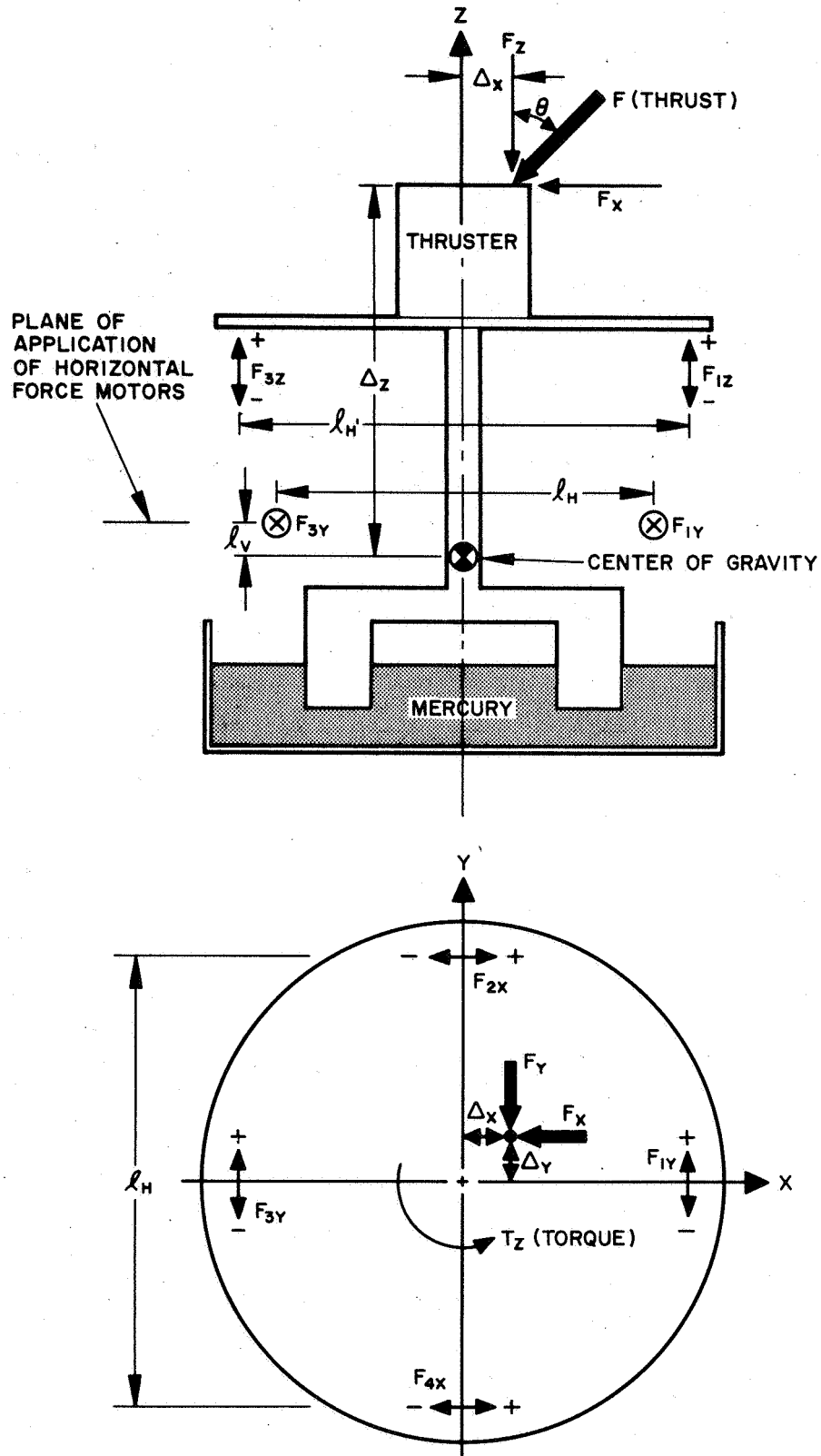
Fig. 31. Thrust stand schematic layout.
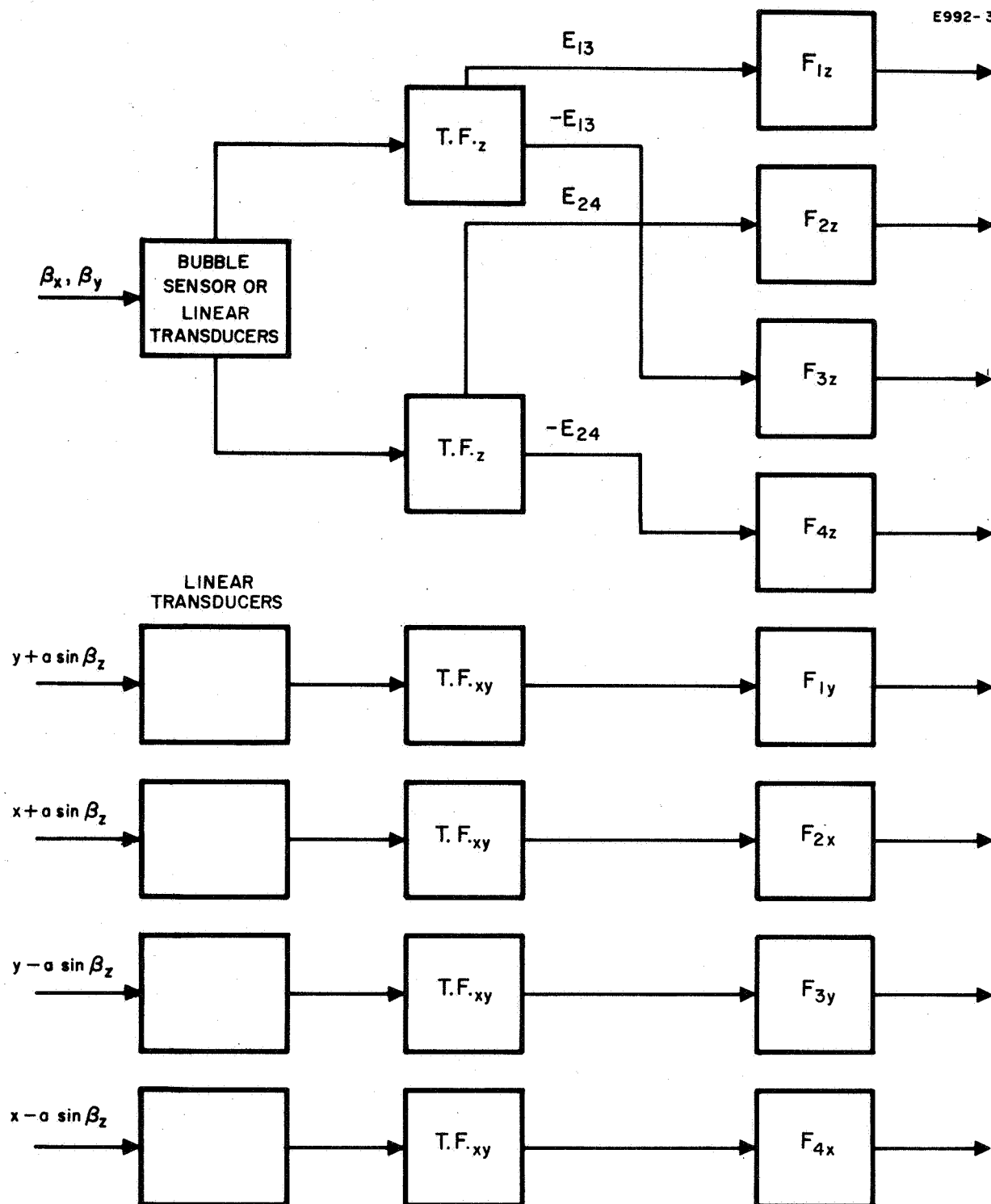
Fig. 32. Transducer-force motor arrangement.

on the edge of the platform. Hence, the displacement which each horizontal transducer experiences is the sum of x-y center of gravity translation, plus rotation ($a \sin \beta_z$). Each of the horizontal force motors is controlled by its associated transducer, independently of the other three. The total system thus has six control loops.

2. Static Analysis

The principle of thrust stand operation is that under steady static conditions, the static forces applied by the force motors exactly cancel out the applied constant force of the thrust vector plus an associated torque. From a knowledge of the force motor readings, the thrust vector deviation from the normal plus the torque may be determined.

The thrust vector deflection is determined by balancing the horizontal force motors. The thrust vector is represented by

$$\vec{F} = F_x \hat{i} + F_y \hat{j} + F_z \hat{k}$$

where i, j, k are unit vectors in the x, y, z directions. The angular deflection θ which we seek may be expressed as

$$\sin \theta = \frac{\sqrt{F_x^2 + F_y^2}}{F} . \tag{38}$$

In order that the x and y components will balance exactly,

$$F_{1y} + F_{3y} = F_y$$

and

$$F_{2x} + F_{4x} = F_x .$$

The amplitude of the total thrust F is measured independently from beam current and voltage. Substituting into (38),

$$\sin \theta = \frac{1}{F} \left[(F_{2x} + F_{4x})^2 + (F_{1y} + F_{3y})^2 \right]^{1/2} . \qquad (39)$$

Therefore, we obtain the deflection θ from calculation involving only the basic horizontal force motors. This is true in theory; in practice, success will depend on the accuracy of the readings, and the required deflection resolution. For $1/4°$,

$$\sin \theta \approx \theta = \frac{1}{4} \left(\frac{\pi}{180} \right) \approx 0.004 \text{ rad.}$$

Assuming no torque about z and equal x-y components ($F_{2x} = F_{4x} = F_{1y} = F_{2y} = F_{xy}$), the force measuring accuracy required to measure this deflection, for a nominal thrust of 0.025 lb is,

$$\theta F = \sqrt{(2F_{xy})^2 + (2F_{xy})^2} = 2\sqrt{2} \; F_{xy}$$

Evaluating,

$$F_{xy} = \frac{(0.004)(0.025)}{2\sqrt{2}} = 0.35 \times 10^{-4} = 35 \; \mu \text{ lb.}$$

The applied engine torque is obtained by balancing the total applied and induced torques against the combined torsional reaction of the force motor array. The induced torque is $\vec{F} \times \vec{R}$, where $\vec{R} = \Delta x \hat{i} + \Delta y \hat{j} + \Delta z \hat{k}$ = the vector distance between the point of thrust application, and the total system center of mass. The induced torque components about the x, y, and z axis are, respectively, $(\Delta z \, F_y - \Delta y \, F_z)$, $(\Delta x \, F_z - \Delta z \, F_x)$, and $(\Delta y \, F_x - \Delta x \, F_y)$.

74

The torque balances about each of the three axes are

$$(F_{1z} - F_{3z}) \, \ell_{H'} - (F_{2x} + F_{4x}) \, \ell_v = \Delta z F_y - \Delta y F_y \qquad (40)$$

$$(F_{2z} - F_{4z}) \ell_{H'} - (F_{1y} + F_{3y}) \, \ell_v = \Delta x F_z - \Delta z F_x \qquad (41)$$

$$- (F_{1y} - F_{3y}) \ell_H + (F_{2x} - F_{4x}) \, \ell_H = \Delta y F_x - \Delta x F_y - T_z \qquad (42)$$

where T_z is the engine applied torque, and ℓ is the lever arm of the force motors about the system center of gravity (Fig. 33).

Equation (42), balance of torques about the z-axis, yields the applied torque T_z, provided we know Δx and Δy, the lateral displacement of the applied force. These are available from (40) and (41). The distance Δz is not unknown, since it represents the distance between the accelerator electrode of the thruster and the system center of gravity. Hence

$$T_z = \left[(F_{1y} - F_{3y}) + (F_{2x} - F_{4x}) \right] \ell_H + (\Delta x F_y - \Delta y F_x)$$

The accuracy required for torque measurement is 5×10^{-4} in. -lb. Neglecting the thrust vector coupling, the last term disappears, and $F_{1y} = F_{2x}$, etc. Thus,

$$T_z = 4 F_{xy} \, \ell_H$$

From Fig. 33, the lever arm length $\ell_{xy} \approx 8$ in.

Evaluating,

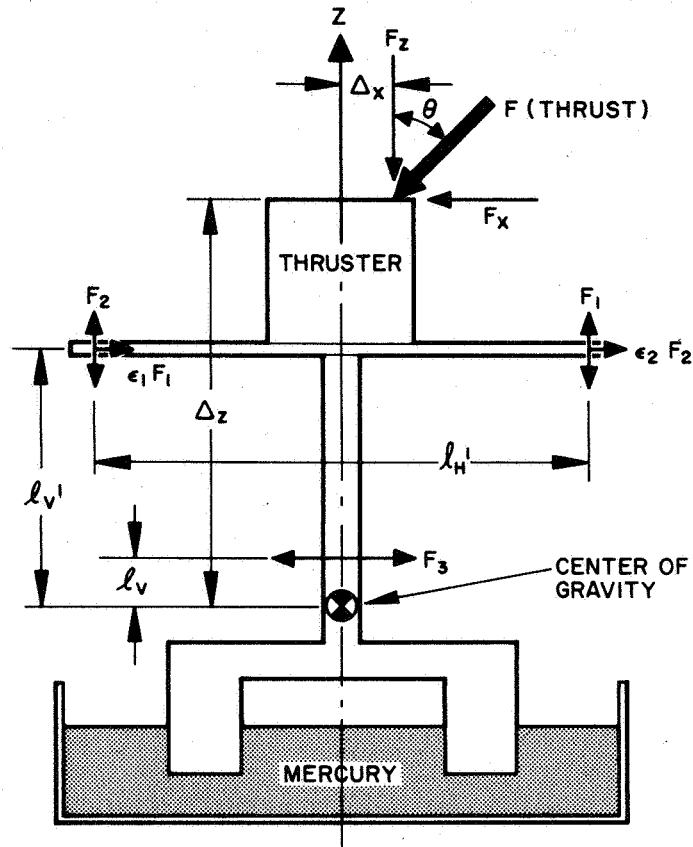$$F_{xy} = \frac{5 \times 10^{-4}}{4 \times 8} = 1.5 \times 10^{-5} = 15 \, \mu\text{lb}.$$

75

Fig. 33.   Forces applied to thrust stand.

Thus, the applied torque measurement accuracy requirement is slightly more severe than that of the thrust vector deflection measurement.

State-of-the-art thrust measurements down to 10 μlb have been demonstrated in a one-axis thrust platform developed by HRL for the U.S. Air Force.[*] However the six degree of freedom platform presents new problems with transducer characteristics, mechanical balancing, and dynamic stability. The dynamics are discussed below.

3. Dynamic Model

In order to study the thrust platform dynamics, the motion was limited to two degrees of freedom: one translational (x) and one rotational (β). The rotational motion is about an axis perpendicular to translation axis, making the problem essentially two-dimensional.

These two components of motion are sufficient to demonstrate the different transducer loop dynamics and the coupling effects between the various degrees of motion. Thus, this limited model can provide adequate insight into the dynamic characteristics of the platform, although it should be kept in mind that the real problem has thrice the complexity represented here.

Figure 34 shows the schematic for the dynamic model.

Three force motors balance the applied force components F_x, F_z. The two force motors F_1, F_2 provide a restoring torque to balance the applied torque $\Delta x F_z + \Delta z F_x + (\ell_3 F_3)$, where Δx, Δz are the applied force coordinates with respect to the system center of mass. The force motor F_3 balances the horizontal applied force component which we wish to measure.

Because we wish to study the platform dynamics, we must now consider other forces which were not important in the static case. These are displacement and damping forces which exist when the system is not in a null condition. These additional forces consist of viscous damping in the mercury liquid, spring displacement and damping forces from the electrical leads, and buoyancy torques due to displacement of

---
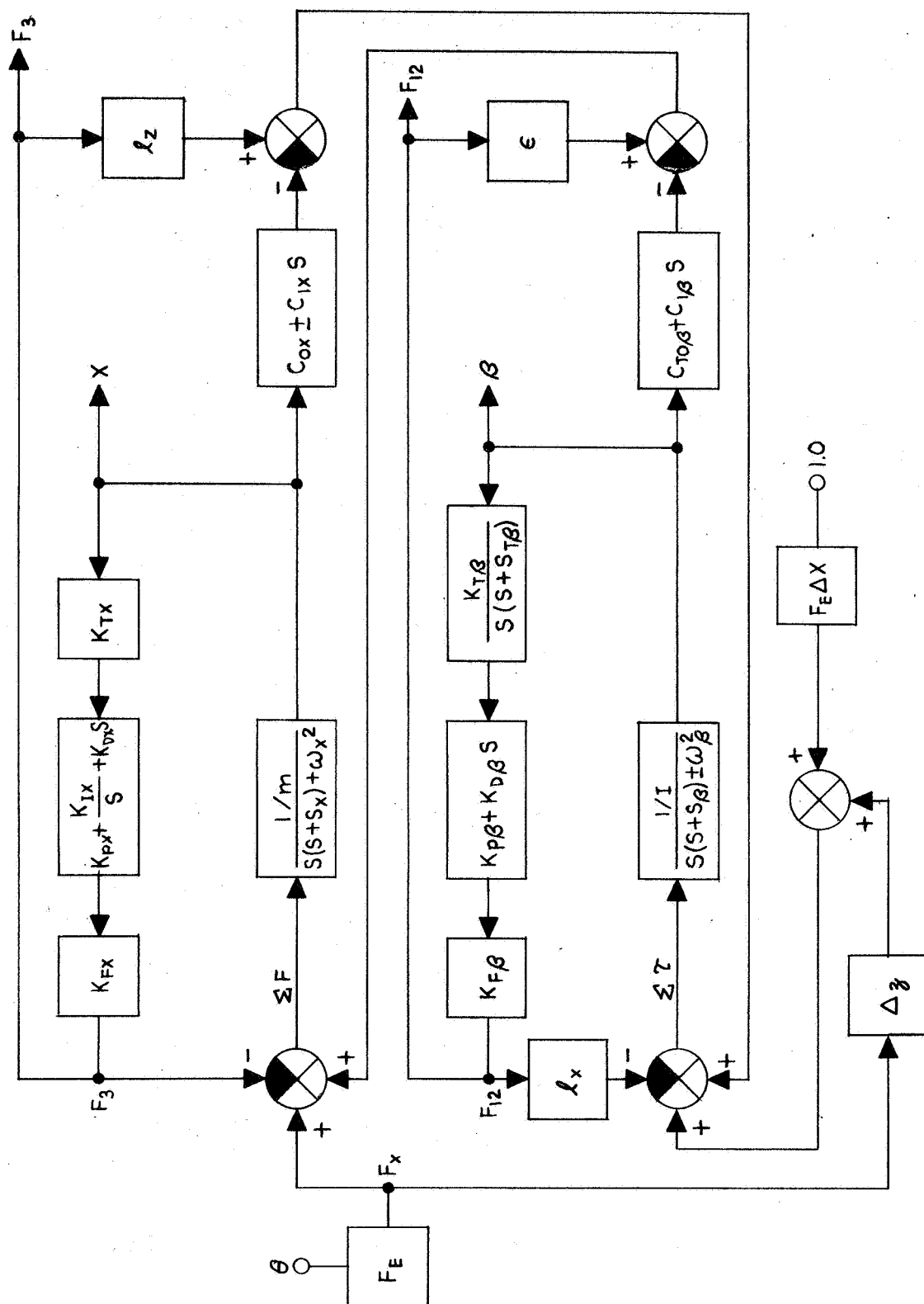
Fig. 34. Block diagram schematic for the two-dimensional dynamic model.

the float metacenter. Thus, each degree of motion is described by a damped spring-mass system, although some of the spring and damping forces may be very small.

In block diagram notation

$$\Sigma \text{ forces} \longrightarrow \boxed{\dfrac{\dfrac{1}{m}}{s(s + s_x) + \omega_x^2}} \longrightarrow \text{displacement (x)}$$

$$\Sigma \text{ torques} \longrightarrow \boxed{\dfrac{\dfrac{1}{I}}{s(s + s_\beta) + \omega_\beta^2}} \longrightarrow \text{rotation } (\beta)$$
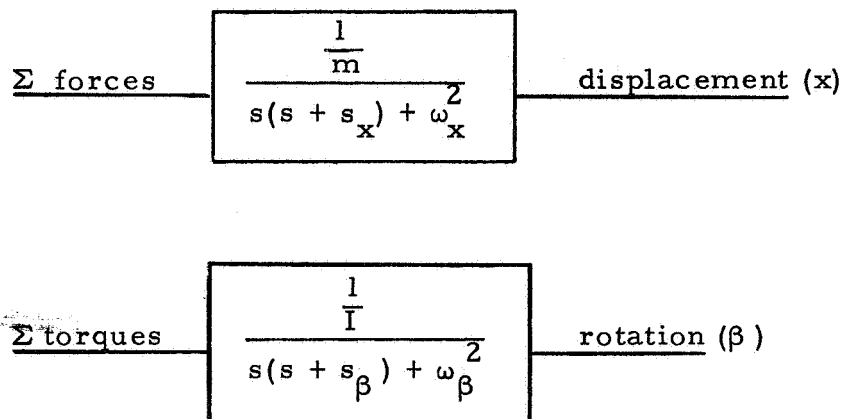
where

$m \equiv$ system mass

$I \equiv$ system moment of inertia about horizontal axis

$\omega_x \equiv$ natural frequency, x-motion

$\tau_x = 1/s_x \equiv$ time constant, x-motion

$\omega_\beta \equiv$ natural frequency, β-motion

$\tau_\beta = 1/s_\beta \equiv$ time constant, β-motion

To complete the model, we also include the coupling forces which can cause one degree of motion to affect another degree. This coupling is of two types:
1. physical coupling
2. induced coupling

79

The first of these can be visualized by considering the translational displacement of a body attached to a spring not at the center of mass. The displacement thus causes a reactive torque, in addition to the translational restoring force. The second type of coupling is that induced by the force motors. For example, when the x-translational force motor acts it will induce a torque.
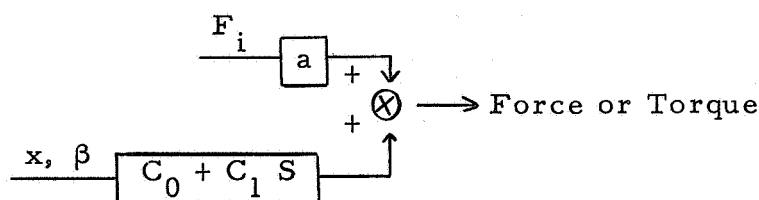
The coupling transfer function may be written

$$\frac{F_i}{\boxed{a}} \xrightarrow{+} \; \substack{+ \\ +} \; \bigotimes \longrightarrow \text{Force or Torque}$$

$$\frac{x, \; \beta}{\boxed{C_0 + C_1 S}}$$

4.   Control System Analysis and Design

The engine thrust measuring instrument is a precision balance of six components of force and torque. Before engine thrust is measured the system must be balanced by adjusting the engine and counterweights to reduce the effects of environmental vibrations which might result from vacuum pumps, seismic disturbances, etc. When the balance adjustments have been made and the mechanical zero established, the mechanical system is then calibrated with the electrical instrumentation and control system.

The following physical equations describe a single degree of translational dynamics of the six-degree thrust platform during an engine thrusting condition. These equations are based on the assumption that the platform has been previously balanced in an engine non-thrust condition such that platform disturbance from background vibration is completely balanced out.

$$(F_E - F_R) = M \ddot{x} + B \dot{x} + K x$$

where

F_E ≡ engine thrust force (lb) or torque

F_R ≡ platform restoring force (lb) or torque

M ≡ total mass of system (lb-sec^2/in.) or moment of inertia

B ≡ velocity damping (lb-sec/in.)

K ≡ spring rate (lb/in.)

$\ddot{x}$ ≡ horizontal acceleration

$\dot{x}$ ≡ horizontal velocity

x ≡ horizontal displacement

Linearizing and performing a LaPlace-transform on the force balance equation yields the linear operator expression

$$\frac{\Delta x(S)}{\Delta F(S)} = \frac{1}{(MS^2 + BS + K)}$$

The thrust platform is designed to have a minimum mechanical spring rate K in the direction of thrust measurement. However, all residual spring forces cannot be completely eliminated. As the value of mechanical spring rate K approaches zero, the transfer function of the mechanical device approaches the following

$$\frac{\Delta x(S)}{\Delta F(S)} \approx \frac{1/B}{S(\tau_1 S + 1)}$$

where

$$\tau_1 = M/B \text{ (sec)}.$$

81

It is clearly shown here that as the mechanical spring rate (resulting from wire, cable, buoyance effect, etc.) approaches zero, the device assumes the characteristics of a mechanical integrator with a cascaded first order lag with a time constant τ_1 (sec).

In order to achieve moderate speed operation the platform mechanism control loop is closed to meet the following requirements:

1. The goal of the dynamic response of the control system with a 20 lb engine weight load on the platform will be approximately 1 cps at all force ranges.

2. The goal threshold of the thrust stand is less than 3.0 μlb of thrust.

3. The goal steady state error of the thrust stand is less than 3% of the upper limit of the 100 μlb range setting.

4. The system is optimally damped for all ranges of thrust and weight loads and stable with a 20 lb engine weight load at all force ranges.

Since the thrust platform is basically an integrator device, the platform will continue to displace as long as a force imbalance exists across the platform within the mechanical limits of the mechanism. To provide a restoring force feedback F_R to servo set the platform to its steady state null position during engine thrusting, it is necessary to provide a voltage integrator to generate a restoring voltage E_R to the restoring motor that is a function of the time integral of the displacement away from the null position. Displacement of the platform Δx causes an error voltage ΔE_x to be generated in the transducer output. This error voltage is integrated to contribute to the restoring voltage E_R to the force motor. When the horizontal forces across the

82

platform are balanced, the platform is restored to the null position. The addition of a voltage or mechanical integrator (i. e., a bubble sensor) into the control loop results in additional control loop phase shift and system instability. Therefore, in order to provide a response with a high degree of stability for this type of system, it becomes necessary to introduce a proportional plus derivative compensating network in parallel with the voltage integrator and in tandem with the mechanical integrator.

a.   Horizontal Loop — Consider now the transfer function block diagram of the horizontal force balance control loop (Fig. 35). The open loop transfer function for the linear system is

$$GH(S) = \frac{K_o (S^2 + a_1 S + a_2)}{S(S^2 + (B/M)S + K/M)}$$

where

$$K_o = \left(\frac{P}{M}\right) \left(\frac{\delta E_x}{\delta x}\right) K_D \text{ rad/sec}$$

$$a_1 = K_p/K_D \text{ (rad/sec)}$$

$$a_2 = K_I/K_D \text{ (rad/sec)}^2$$

$$P = K_A K_M \text{ (lb/V)}$$

$K_P \equiv$ proportional gain (volts/volts)

$K_D \equiv$ derivative gain (volt-sec/volt)

$K_I \equiv$ integral gain (volt/sec-volt)

$P \equiv$ force motor power gain (lb/volt)

$\dfrac{\delta E_x}{\delta_x} \equiv$ displacement transducer gain (V/in.)
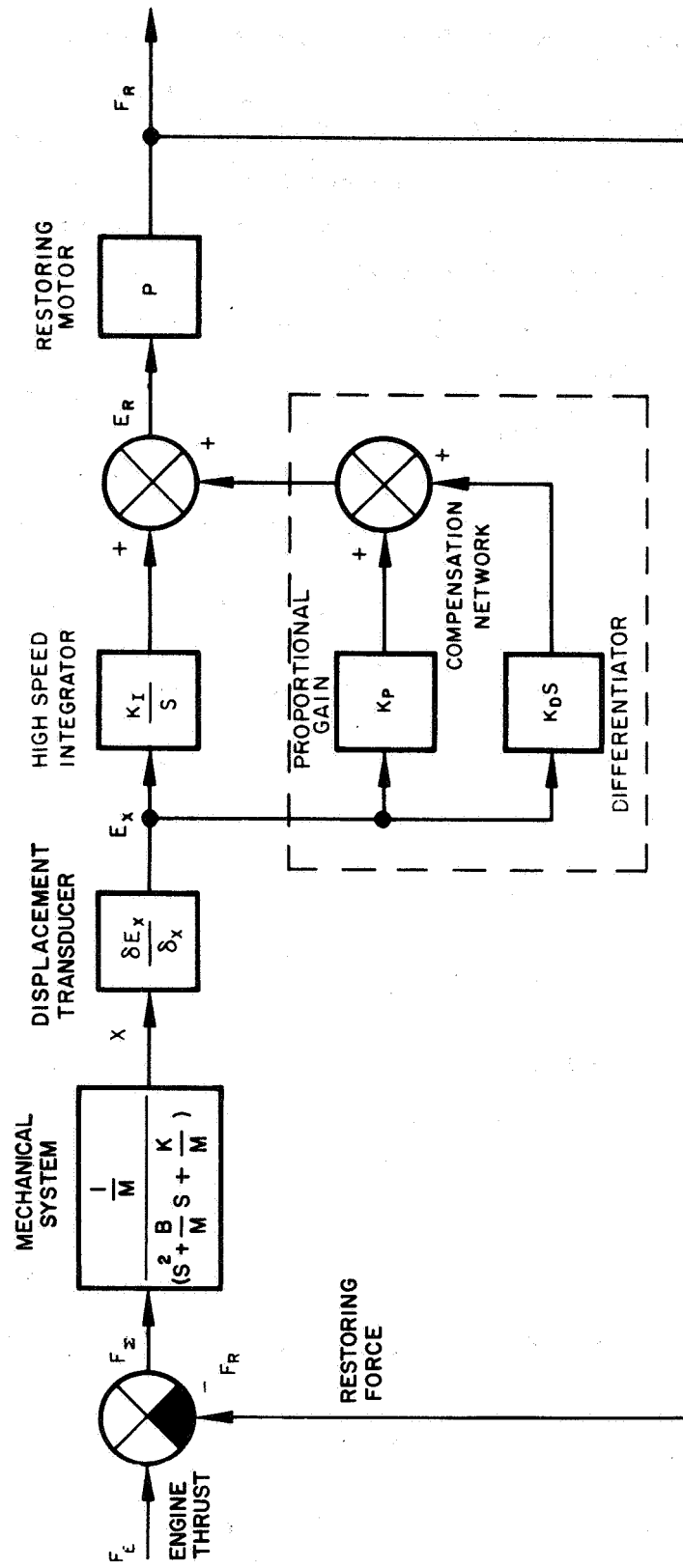
83

Fig. 35. Horizontal force balance control loop system block diagram.

If the network gains can be assumed to be adjustable, then a_2 can be set approximately to equal (K/M) and a_1 can be adjusted to approach (B/M) experimentally (e.g., the network gains* can be set to the following analytically determined values).

$$a_1 = K_P/K_D = B/M \approx 5.0 \text{ (rad/sec)}$$

$$a_2 = K_I/K_D = K_x/M \approx 1.0 \text{ (rad/sec)}^2$$

If $K_D = 1.0$ sec/rad, then $K_I = 1.0$ rad/sec and $K_P = 5.0$. The roots of the polynominal are thus

$$S^2 + (B/M)S + K/M = S^2 + (K_P/K_D)S + \frac{K_I}{K_D} = 0$$

$$\sigma = -\frac{a_1}{2} \pm \frac{1}{2}\sqrt{a_1^2 - 4}$$

$$= -2.5 \pm \frac{1}{2}\sqrt{25 - 4}$$

$$\sigma_1 = -0.2 \,, \; \sigma_2 = -4.8$$

The open loop transfer function is thus

$$\frac{F_R(S)}{F_\Sigma} = \frac{K_o(S + \sigma_1)(S + \sigma_2)}{S(S^2 + (B/M)S + K/M)}$$

---

*Gains less than unity (1) imply passive networks.

where $F_\Sigma = F_E - F_R \equiv$ error signal, as shown in Fig. 35. Because the roots of the network are adjusted to equal the roots of the mechanical system, the open loop transfer function is reduced to

$$\frac{F_R}{F_\Sigma}(S) = \frac{K_o}{S}.$$

The closed loop transfer function now becomes

$$\frac{F_R}{F_E}(S) = \frac{K_o}{S + K_o} = \frac{1}{\tau S + 1}$$

The over-all loop response acts as a first order lag with a time constant (τ) equal to $1/K_o$, i.e.,

$$\tau = \frac{1}{K_o} = \left(\frac{M}{P}\right) \frac{1}{K_D\left(\frac{\delta E_x}{\delta_x}\right)} (\text{sec})$$

Here

$$M = 0.065 \text{ lb sec}^2/\text{in}$$

$$K_D = 1.0 \text{ sec/rad}$$

$$\left(\frac{\delta E_x}{\delta_x}\right) \approx 10^4 \text{ V/in.}$$

$$P = 10^{-5} \text{ lb/V.}$$

Therefore,

$$\tau \approx 0.65 \text{ sec.}$$

Improved frequency response can be obtained by increasing the proportional network gain K_P. For example, let $K_P = 50$; the network roots are then

$$\sigma = \frac{-50}{2} \pm \frac{1}{2} \sqrt{2500 - 4}$$

$$\sigma = -25 \pm \frac{1}{2} \sqrt{2496}$$

$$\sigma_1 \approx 0.02; \quad \sigma_2 \approx 50$$

The open loop transfer function now becomes

$$\frac{F_R}{F_\Sigma}(S) = \frac{K_o (S + 0.02)(S + 50)}{S (S + 4.8)(S + 0.2)}$$

A plot of the root locus of the open loop transfer function is shown in Fig. 36. The percent overshoot when the system is subjected to a step input can be estimated easily by referring to Fig. 37. For a damping factor $\xi = 0.7$ the overshoot is near zero. For higher values of damping factor it is noted that the system is heavily damped. For lower values of damping, the system is underdamped. For operation at a damping factor of 0.7, the over-all system natural frequency (ω_n) is approximately 65 rad/sec or 10 cps, as shown in Fig. 36. This estimate will be verified in subsequent analog solutions.

$$\omega_n = 65 \text{ rad/sec} \approx 10 \text{ cps}$$

$$\xi = 0.7$$

The closed loop function of the horizontal force balance system is

$$\frac{F_R}{F_E}(S) = \frac{G}{1 + GH}(S)$$

where $H = 1$.

$$G(S)H(S) = \frac{Ki(S+0.02)(S+50)}{S(S+0.2)(S+4.8)}$$

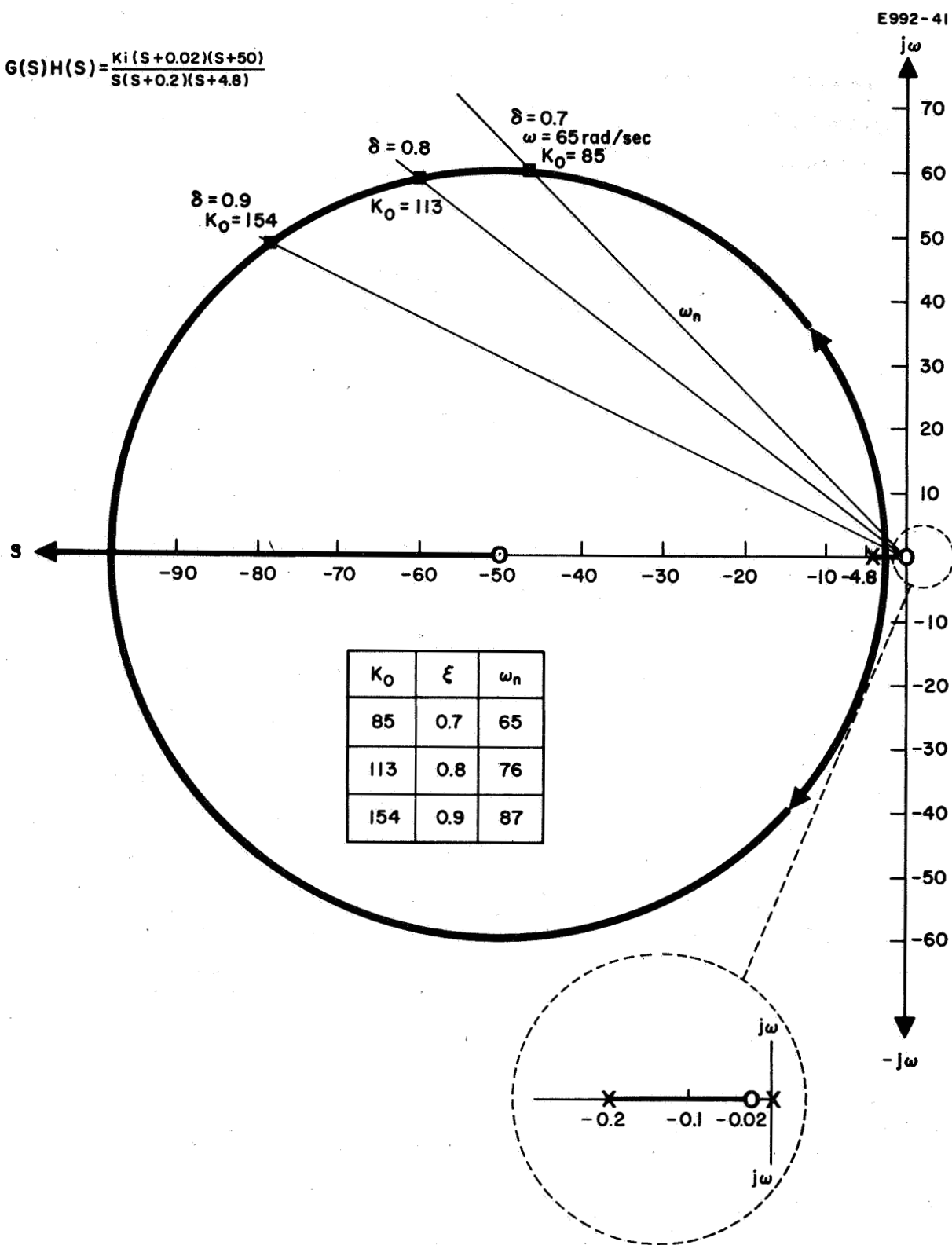| K_O	ξ	ω_n
85	0.7	65
113	0.8	76
154	0.9	87

Fig. 36. Root locus plot of horizontal platform control open loop transfer function.
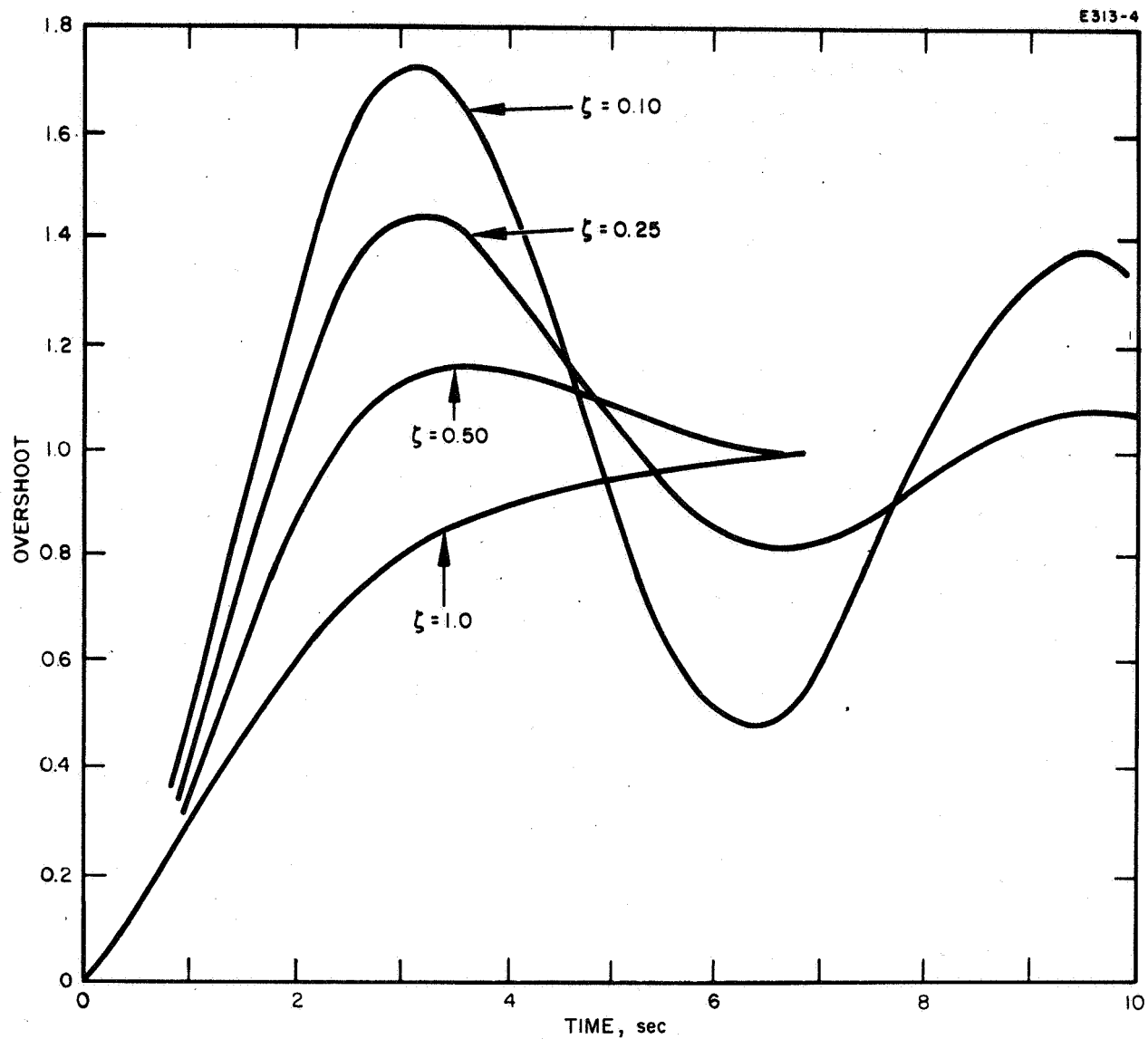
Fig. 37. Unit step-function response for system with transfer function $\omega_s^2/(s^2 + 2\zeta\omega_n s + \omega_n^2)$.

The frequency response characteristic shows that the theoretical system bandwidth is approximately 20 cps for a system gain of $K_o = 85$ rad/sec. The system equations indicate that bandwidth of the horizontal force system can be extended by increasing the system gain K. Thus, the power gain of the control loop and the mass of the system will determine the system bandwidth; for a 10 cps system natural frequency with a 20 lb load on the thrust stand, the open loop gain of the system should be at least

$$K_o = \frac{P}{M} \left(\frac{\delta E_x}{\delta x}\right) K_D = 85 \text{ rad/sec.}$$

b.   Rotational Deflection Control Loop — Consider now the transfer function block diagram of the rotational force balance control loop shown in Fig. 38. The basic components of the system are the mechanical system, bubble sensor, compensating network, and power amplifier and electromagnetic force motor.

In theory, any static moment resulting from an off-axis engine thrust component will be counter balanced by an equal and opposite torque from the force motor, provided that the control loop is properly designed. The design of a compensating network for the rotational control loop is somewhat more critical, however, because of the dynamic characteristics of the deflection sensing device (the bubble level sensor).

Consider the basic system problem. The Laplace transfer function of the mechanical system in the rotational axis, neglecting for the moment the cross coupling effects, may be described as

$$\frac{\Delta \theta}{\Delta F_E} (S) = \frac{1/I}{(S^2 + 2\xi \omega_\beta S + \omega_\beta^2)} \tag{43}$$

where

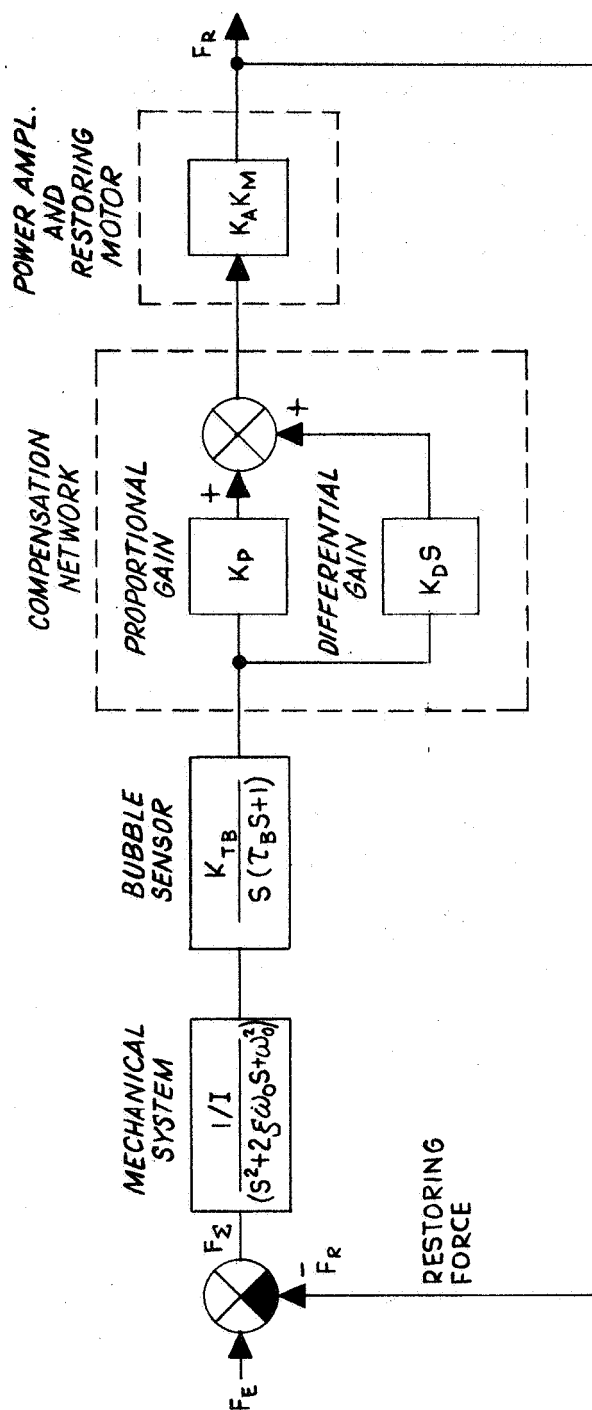$$\omega_\beta = f (I, K_{eff})$$

90

Fig. 38. Rotational force balance control loop system block diagram.

As the effective spring rate K_{eff} approaches a small value, as in the case of a neutrally balanced system with negligible spring rate coupling of the electrical cabling, the platform system dynamics approach the characteristics of a mechanical integrator for small force perturbations; e.g., as $\omega_\beta \rightarrow$ small value,

$$\frac{\Delta\theta}{\Delta F_E}(S) = \frac{1/I}{S(S + 2\xi\omega)} \tag{44}$$

The bubble sensor also has the characteristics of a mechanical integrator, i.e.,

$$\frac{\Delta E}{\Delta\theta}(S) = \frac{K_{TB}}{S(S + S_{TB})} \tag{45}$$

The cascading of the two devices now presents a relatively severe stability problem, as shown below.

$$\frac{\Delta E}{\Delta F_E}(S) = \frac{K_{TB}/I}{S^2(S + 2\xi\omega_\beta)(S + S_{TB})} \tag{46}$$

The double integration term (S^2) results in 180° phase shift of the input signal. The compensation network therefore must correct the total system phase shift to less than 180° if over-all loop stability is to be achieved.

The first step in considering the compensating network is to consider a single first order lead network coupled to the output of the bubble sensor output. This network would be comprised of a proportional plus derivative network:

$$\frac{\Delta\theta^1}{\Delta\theta} = K_p + K_D S = K_p(\tau_c S + 1) \tag{47}$$

92

where

$$\tau_c = \frac{K_D}{K_p} \, .$$

In order to simplify the circuit design, it would be desirable that the gain terms be less than unity so that a passive network could be utilized; therefore, let us assume the following values:

$$K_p = 1 \ V/V$$

$$K_D = 1 \ V\text{-sec}/V.$$

Therefore,

$$\tau_c = 1 \ \text{sec.}$$

This system is illustrated in the rotational force balance control loop system block diagram shown in Fig. 38. The dynamics of this system are described in the results of the analog computer simulation (Section V-A-5).

Consider now the root locus of the above described system. The open loop transfer function of the system is

$$\frac{F_R}{F_\Sigma} (S) = \frac{K_{TB} \ K_p \cdot P/I \ (K_D/K_p \ S + 1)}{S(S^2 + 2 \ \xi \ \omega_\beta \ S + \omega_\beta^2) \ (\tau_B \ S + 1)} \tag{48}$$

where

$$P = \text{power gain} = K_A \ K_M \ (\text{lb}/V).$$

Substituting in values as described in Table IV, the open loop transfer equation becomes

$$\frac{F_R}{F_\Sigma}(S) = \frac{K_B (S + 1)}{S(S^2 + 4S + 4)(S + 3)} \tag{49}$$

The root locus of the above transfer function is shown in Fig. 39 and shows that this system requires that the loop gains be very low for stability. On the other hand, a high loop gain is desirable for high steady state accuracy. Thus, the above system cannot satisfy both stable system response and high steady accuracy.

The next step is to cascade an additional lead network into the compensating network. It should be noted that each time another lead network is added, increased noise problems are introduced into the system. However, consider a second order lead network which exactly compensates out the effects of the platform mechanics, i.e.,

$$S^2 + \left(\frac{K_{p1}}{K_{D1}} + \frac{K_{p2}}{K_{D2}}\right) S + \left(\frac{K_{p1}}{K_{D1}} \frac{K_{p2}}{K_{D2}}\right) = (S^2 + 2 \xi \omega_B S + \omega_B^2) \tag{50}$$

This network will result in an active compensating network (i.e., high gain dc amplifiers). Consider the characteristics of the new system open loop transfer function

$$\frac{F_R}{F_\Sigma} = \frac{K_B^1 \left[S^2 + \left(\frac{K_{p1}}{K_{D1}} + \frac{K_{p2}}{K_{D2}}\right) S + \left(\frac{K_{p1}}{K_{D1}} \frac{K_{p2}}{K_{D2}}\right)\right]}{S(S^2 + 2 \xi \omega_\beta S + \omega_\beta^2)(\tau_B S + 1)} \tag{51}$$

TABLE IV

Constants and Parameters

F_E = 0.025 lb

K_{Tx} = 10,000 V/in.

ℓ_B = 8.25 in.

ℓ_X = 7.75 in.

ℓ_Z = 1.5 in.

Δ_x = 0.25 in. → 0

Δ_z = 15.5 in.

m = 0.17 lb-sec^2/in.

I = 9.1 slug-ft-in.

$K_{T\beta}$ = 10^5 V-rad/sec^2

ϵ = 0.1

ω_x^2 = 1.0 rad^2/sec^2

τ_x = 0.1 → 1.0 sec (.2)

ω_β^2 = ±1.0 → 10.0 sec = (1.0)

τ_β = 0.1 → 1.0 sec = (1.0)

$\tau_{T\beta}$ = 0.32 sec

C_{0x} = 0.17 lb

C_{1x} = -1.4/τ_x → 0.17/τ_x lb-sec -7 → +1

$C_{0\beta}$ = 0.83 lb

$C_{1\beta}$ = 0.0 → 0.83/τ_x lb-sec; 4

K_{Px} = 5 (or 1/τ_x)

K_{DX} = 1

K_{IX} = 1

$K_{P\beta}$ = 1

$K_{D\beta}$ = 1

$\dfrac{\partial F_x}{\partial E_x} = \dfrac{\partial F_\beta}{\partial E_\beta} = 10^{-4}$ lb/V

$$GH(S) = \frac{K(S+1)}{S(S^2+4S+4)(S+3)}$$

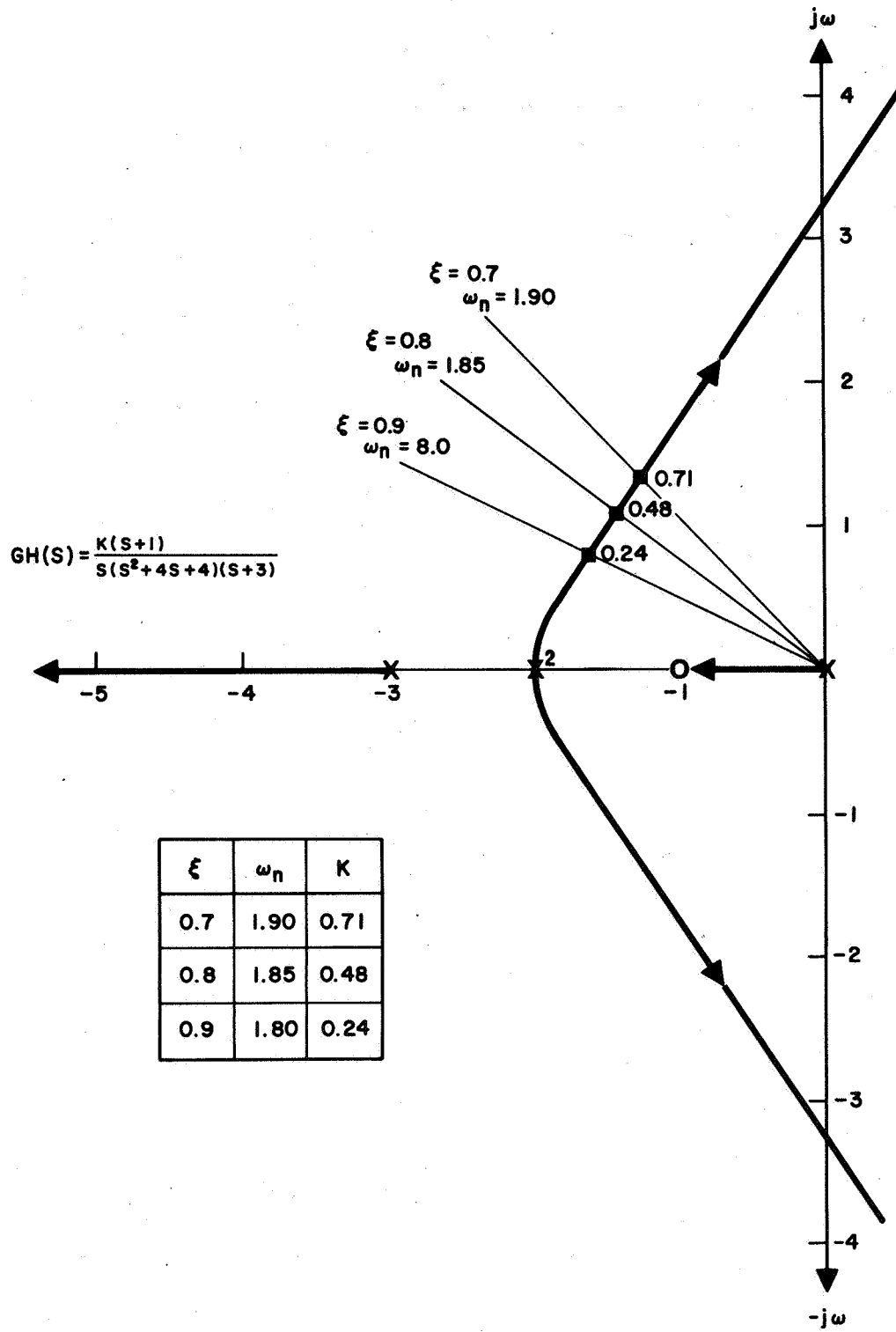| ξ	ω_n	K
0.7	1.90	0.71
0.8	1.85	0.48
0.9	1.80	0.24

Fig. 39. Root locus for single lead conpensating network for rotational deflection loop.

where

$$\left(\frac{K_{p1}}{K_{D1}} + \frac{K_{p2}}{K_{D2}}\right) = 2\,\xi\,\omega_\beta \text{ (rad/sec)}$$

$$\frac{K_{p1}}{K_{D1}} \frac{K_{p2}}{K_{D2}} = \omega_\beta^2 \text{ (rad/sec)}^2$$

The rotational force balance system open loop transfer function can now be resolved to approximately

$$\frac{F_R}{F_\Sigma}(S) = \frac{K_B^1}{S(\tau_B S + 1)} \tag{52}$$

with a closed loop transfer function of

$$\frac{F_R}{F_E}(S) = \left(\frac{1}{a_3 S^2 + a_4 S + 1}\right) \text{ (lb/lb)} \tag{53}$$

where

$$a_3 = \frac{\tau_B}{K_B^1} \text{ sec}^2$$

$$a_4 = \frac{1}{K_B^1} \text{ (sec)}$$

since

$$\tau_B = 0.32 \text{ sec}$$

$$\frac{a_3}{a_4} = 0.32.$$

97

Figure 40 shows the root locus of the open loop transfer function of (52) which is characteristic of a simple second order system. While the cascading of a second order lead network appears to solve the transient problem, it should be pointed out that each lead network should be followed by a double lag network to filter any high frequency noise that may appear in the signal conditioning. These filters should be designed for break frequencies approximately two octaves above the desired maximum system frequency. For example, if the system response goal is 1 cps, the filters should be designed for approximately 4 cps (25 rad/sec).

Thus, the filter design would be

$$\frac{e_o}{e_i} = \frac{1}{(\tau_f S + 1)^2} = \frac{1}{(0.04 S + 1)^2}$$

where

$$\tau_f = R C \text{ (sec)}$$

For standard components, let

$$C = 0.33 \ \mu F \ \pm 10\%$$

$$R = 120 \ k\Omega \ \pm 10\%$$

$$RC = \approx 0.04 \text{ sec.}$$

It can be postulated and shown in a simple classical controls analysis that additional lead networks can be cascaded to the compensating network. However, the preceding analysis is valid only for small perturbations of the input signal while the system is in a quiescent state. The analysis does not consider voltage power supply transients when the electrical power is turned on; nor does it consider noise transients

$$GH(S) = \frac{K(S^2 + \delta_B\, S + \omega_B^2)}{S(S^2 + \delta_B\, S + \omega_B^2)(S+3)}$$

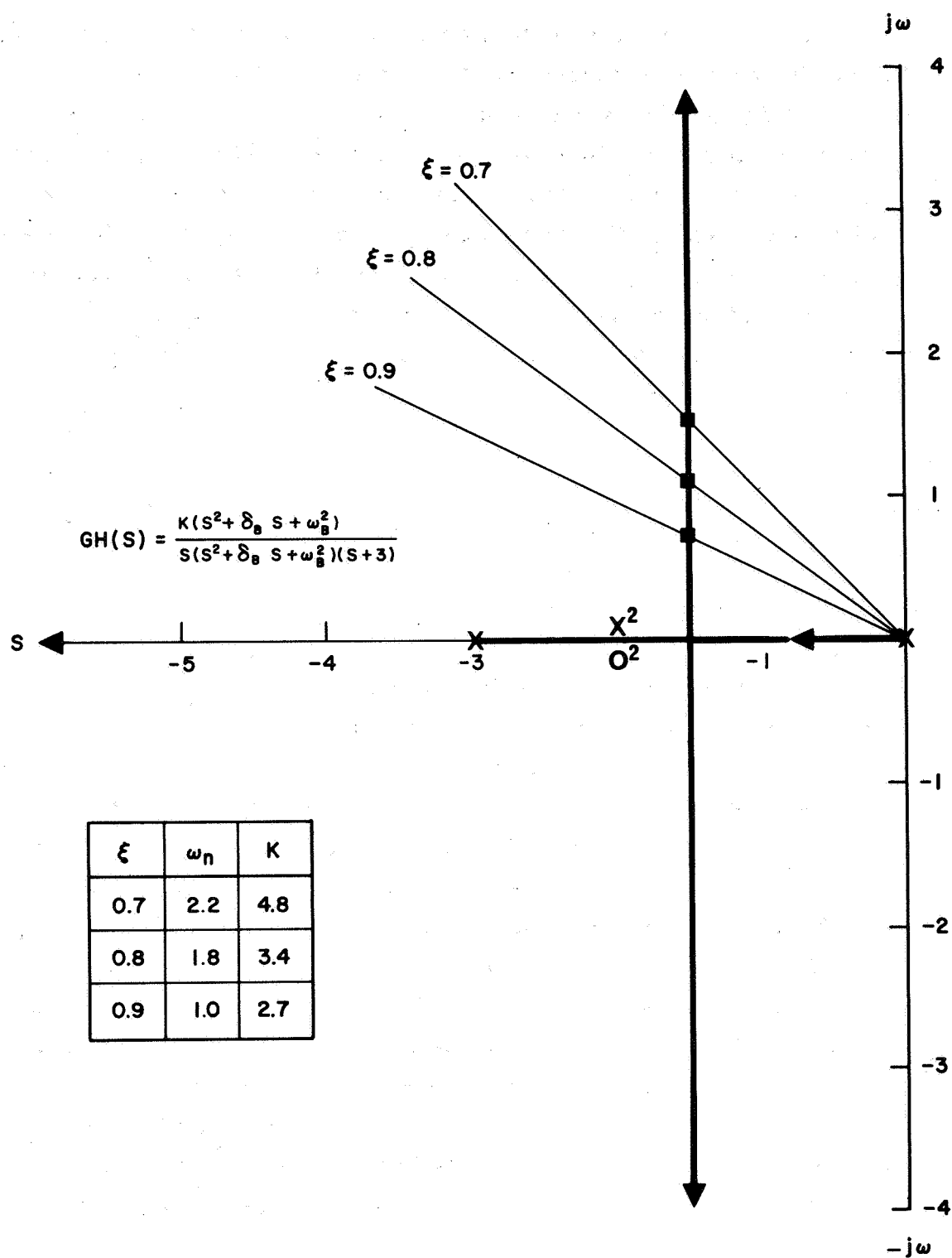| ξ	ω_n	K
0.7	2.2	4.8
0.8	1.8	3.4
0.9	1.0	2.7

Fig. 40. Root locus for a second order lead filter for the rotational deflection loop.

from engine sputtering or arcing conditions. Experience has shown that the linear hand analysis should be used only as a guide to the design. A full scale analog or digital computer study of the transient behavior of the system to voltage transients caused by electrical power variations, engine arcing conditions, power supply turn on conditions, thermal variations in the force motors, etc., is mandatory to a well designed system. Figure 41 shows the root locus of the rotational deflection control loop utilizing a third order lead network. The lead network gain values have been set at unity to facilitate the use of passive network elements.

$$K_p = 1 \text{ V/V}$$

$$K_D = 1 \text{ V-sec/V}$$

$$\text{Lead network} = (S + 1)^3.$$

This system is stable for all values of gain. While it may be postulated that lead networks can be cascaded indefinitely, the physical characteristics of the components may not permit this. Lead networks have noise enhancement characteristics and the stability of the operational amplifiers may be impaired. In addition, while the lead networks appear to solve the transient problem, it is unlikely that the desired system steady state accuracy can be achieved.

While the design of the compensating network is feasible, the added complexity results in additional electrical components and dc amplifiers. A simple solution to the rotational displacement control stability and steady state accuracy requirement is to merely replace the bubble sensor with a linear displacement transducer. The rotational displacement control loop would then demonstrate the same stable, accurate characteristics of the horizontal displacement control loop.

100

$$GH(S) = \frac{K(S+1)^3}{S(S^2 + \delta_B S + \omega_B^2)(S+3)}$$

WHERE, $\delta_B = 4.0$; $\omega_B^2 = 4.0$

$\delta \cong 0.94$

$\omega_n = 1.5$

δ	ω_n	K
0.94	1.5	3.4
1.0	1.0	∞

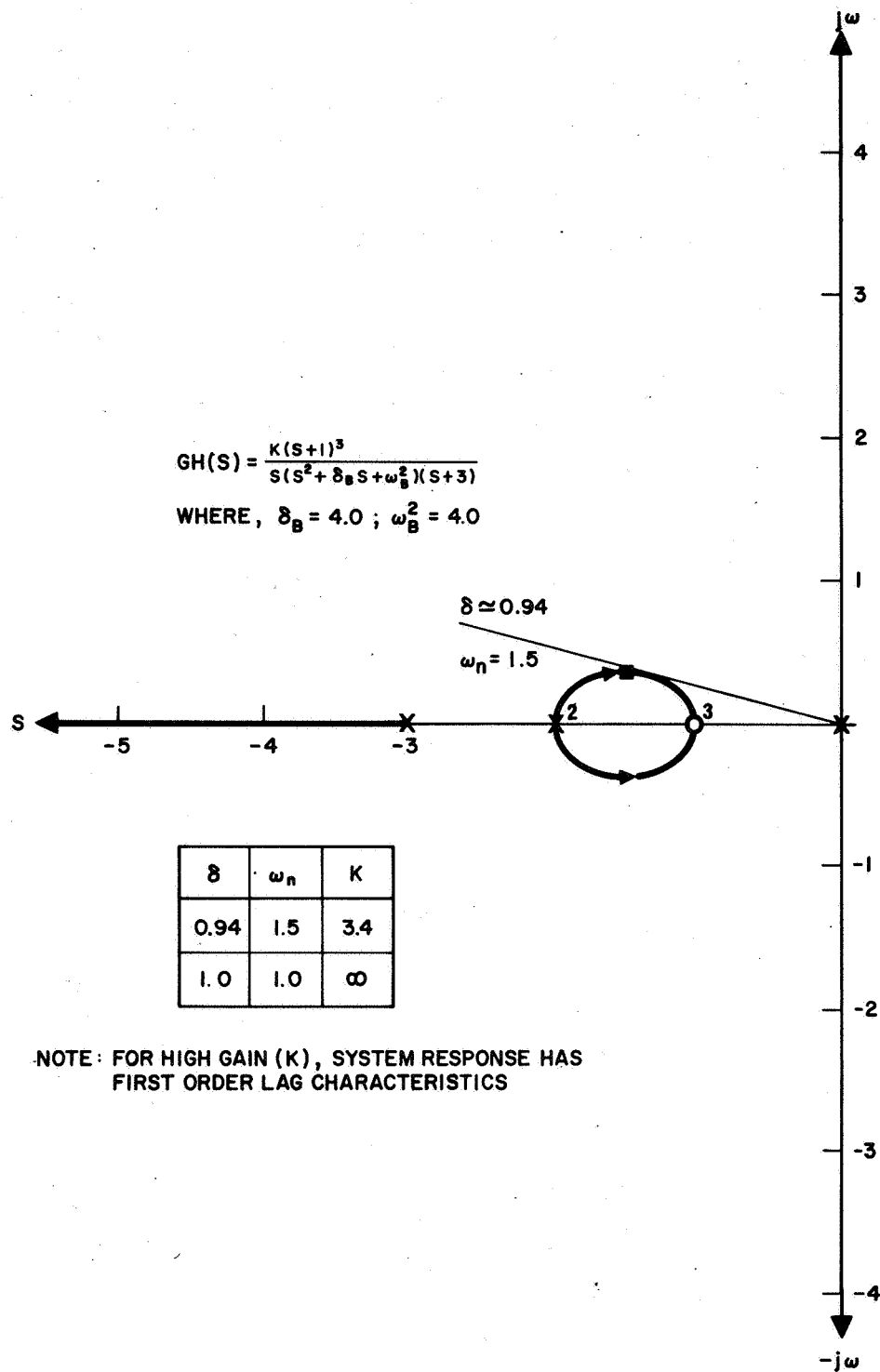NOTE: FOR HIGH GAIN (K), SYSTEM RESPONSE HAS FIRST ORDER LAG CHARACTERISTICS

Fig. 41. Root locus for a third order lead filter for the rotational deflection loop.

The effects of limited cross coupling have been assessed analytically. The system has been mechanized on the HRL Pace 16-31 analog computer and will be discussed in the subsequent sections of this report.

Figure 42 shows a comparison of the system derived from Fig. 40 and the simple linear displacement transducer loop used in the horizontal deflection control.

5. Analog Study

Analog simulation (Fig. 43) of the dynamics of the thrust platform and control system has been conducted on the HRL-PACE 16-31R general purpose analog computer. The purpose of this study was to develop an electronic control system which would provide a stable, dynamic response for the balanced thrust platform system for all conditions of engine thrusting. The study included the determination of amplifier gains, sizing of the compensation networks, cross coupling effects, and the investigation of the over-all system transient behavior. In addition, the effect of the coupling to the platform of numerous electrical cabling and on system stability and accuracy was investigated.

During the study, the analog model of the balanced thrust platform system was subjected to thrust vector step deflections ranging from 1/40 to 1/8°, at a nominal thrust level of 0.025 lb. The values of system parameters used in the simulation are listed in Table V.

The results in the next section are based on the control systems described previously.

6. Results

Figures 44 through 50 demonstrate the significant analog results. The first four figures correspond to uncoupled loops, where it is assumed that the translational and rotational motions do not interact. Figure 44 shows the uncoupled translational response of the platform to a thrust vector step deflection of 1/8°. The effect of increased force motor gain is also shown. An increase from 10 μlb/V
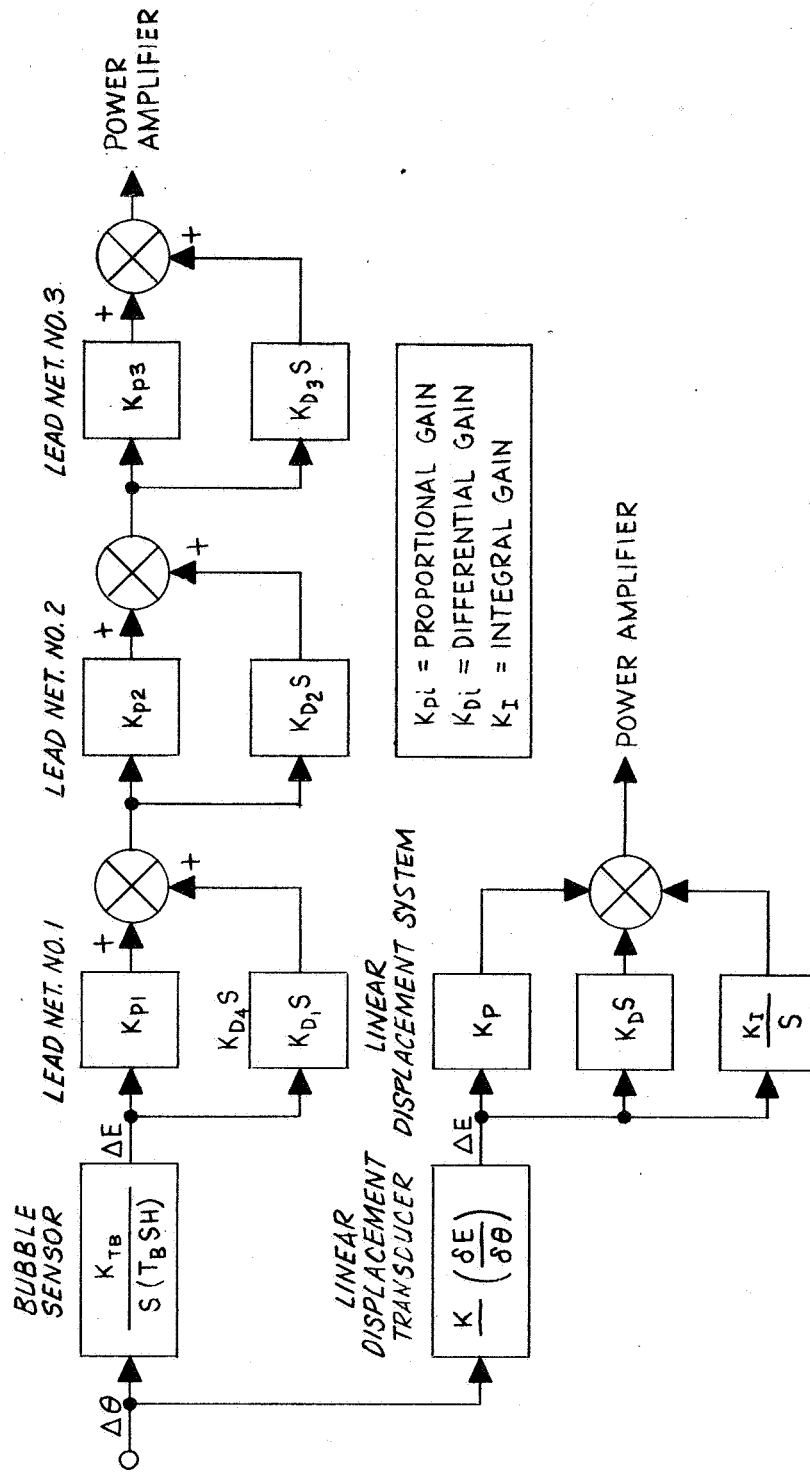
Fig. 42. Comparison of deflection instrumentation systems and their compensating networks.
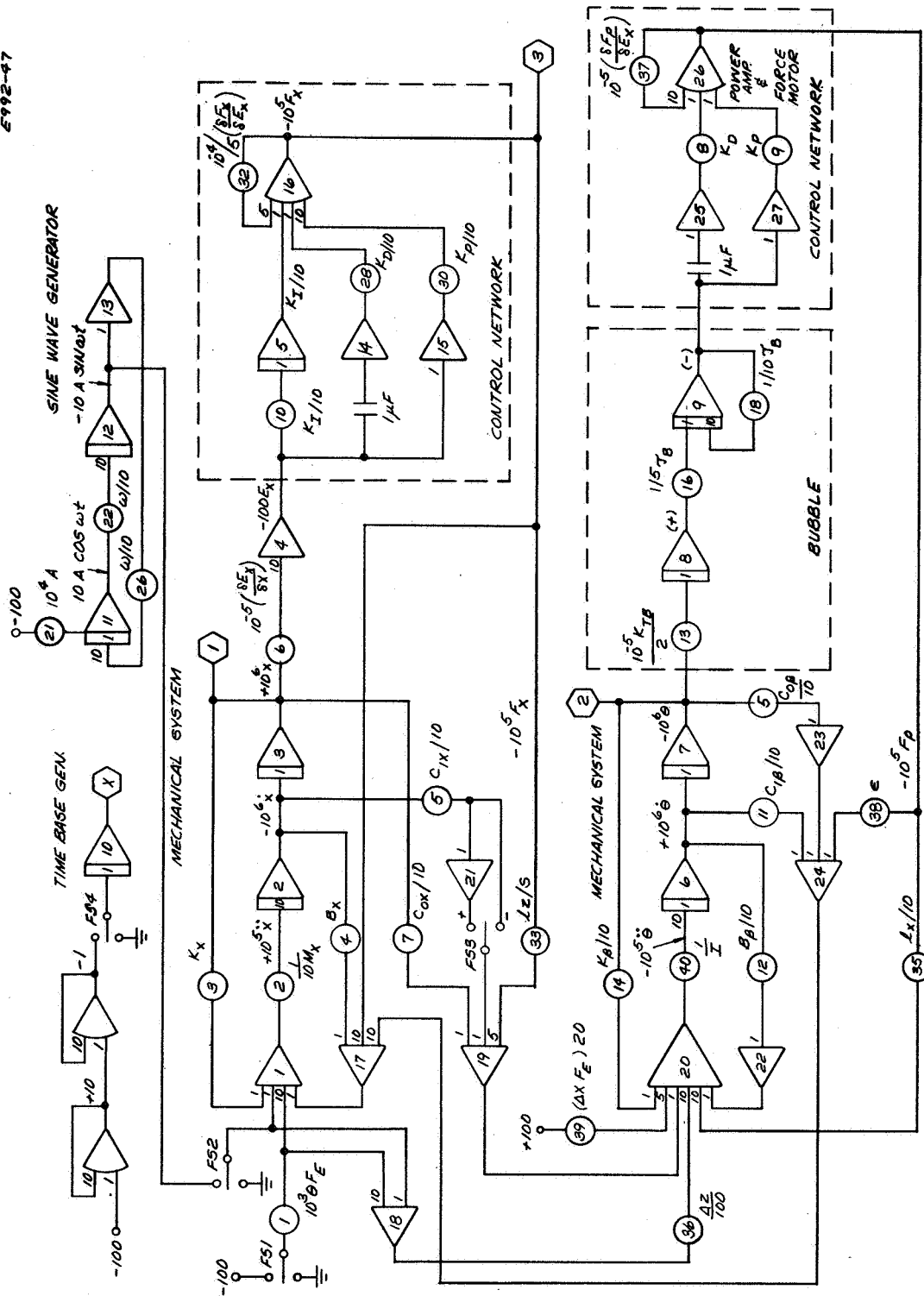
Fig. 43. Analog simulation of the thrust platform dynamic model.

104

TABLE V

Potentiometer Settings for Analog Simulation

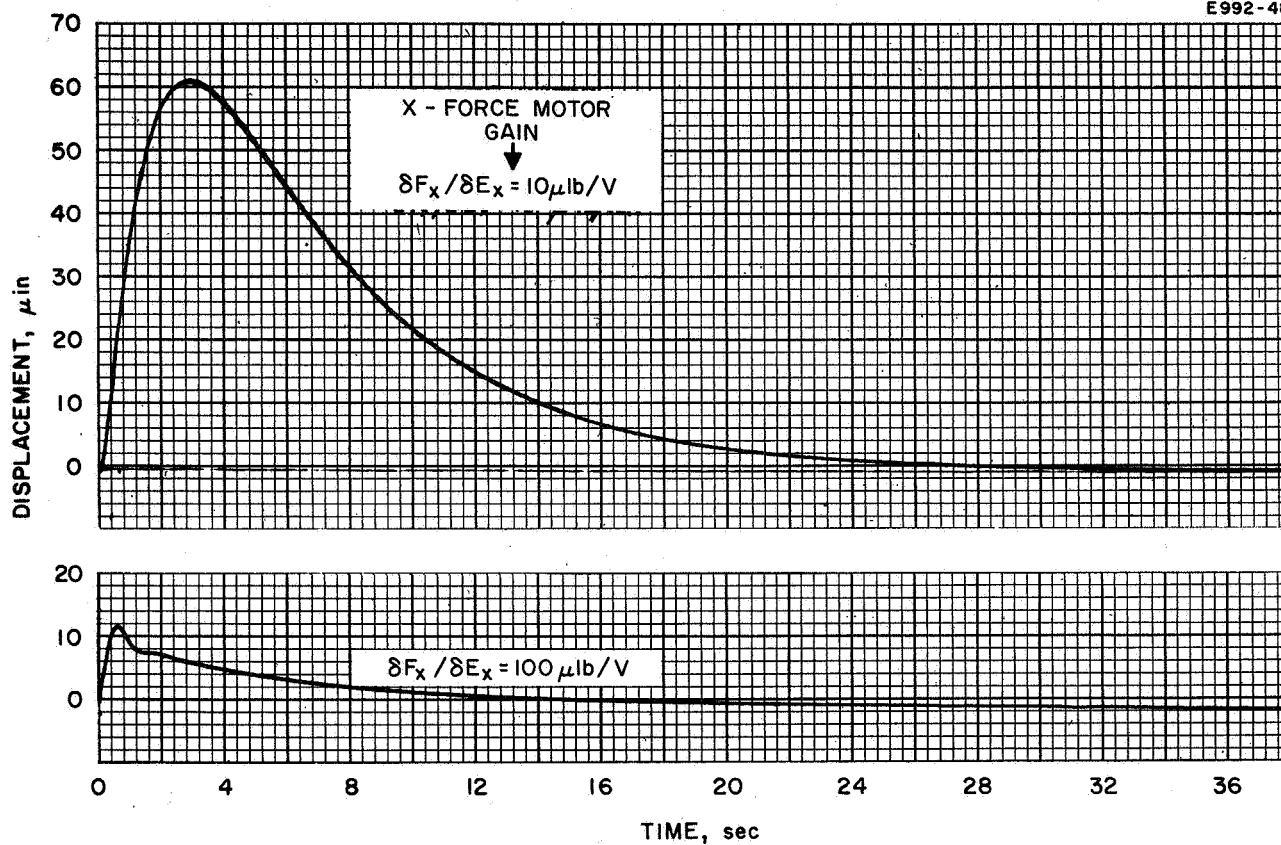| 1	$10^3 \theta F_E$	0.10	18	$1/(10 \tau_{TB})$	0.31
2	$1/(10 M_x)$	0.59	20	(time base gen)	
3	$K_x = \omega_x^2 M_x$	0.17	21	$10^4 A$ ⎫	
4	$B_x = M_x/\tau_x$	0.85	22	$\omega/10$ ⎬ sin-wave gen.	
5	$C_{1x}/10$	$-.7 \to +.1$	26	$\omega/10$ ⎭	
6	$10^{-5}(\delta E_x/\delta_x)$	0.10	28	$K_{DX}/10$	0.10
7	$C_{ox}/10$	0.02	30	$K_{PX}/100$	0.05
8	$K_{D\beta}$	1.00	32	$10^{-5}/(dF_x/E_x)$	1.00
9	$K_{P\beta}$	1.00	33	$\ell_z/5$	0.30
10	$K_{Ix}/10$	0.10	35	$\ell_x/10$	0.775
11	$C_{1\beta}/10$	$0 \to .4$	36	$\Delta Z/100$	0.155
12	$B_\beta = I/\tau_\beta/10$	0.91	37	$10^{-5}/(\delta F_\beta/\delta E_\beta)$	1.00
13	$10^{-5} K_{T\beta}/2$	1.00/2	38	E	0.10
14	$K_\beta = \omega_\beta^2 I/10$	0.91	39	$\Delta X F_E (100/5)$	0.125 = 0
15	$C_{o\beta}/10$	0.08	40	$1/I$	0.11
16	$1/(10 \tau_{T\beta})$	(0.31) 2			

Fig. 44. Displacement response to a step in thrust vector deflection; $\Delta\theta = 1/8^{\circ}$ (uncoupled).

to 100 μlb/V reduces the maximum displacement by a factor of six, and the time response by a factor of two. These displacements are seen to be on the order of 10 μin., and the time response is several seconds. Figure 45 shows the force motor response associated with the translational displacement. The steady state balancing force is 50 μlb. These dynamics are well behaved; therefore, no problem is anticipated with the translational loop.

Figure 46 shows the uncoupled response for the simple rotational loop of Fig. 38 using a bubble sensor following a thrust vector deflection step of $1/40^\circ$. The effect of different force motor gains are shown, ranging from 1 to 4 μlb/V. The loop is seen to go unstable at the higher gain, but is stable with about 10 sec response at the lower gain. The angular displacements are on the order of 20 μrad. Thus, the rotational loop requires a low gain in order to assure stability; for this reason the loop could not take a much larger input step. The low gain allows the rotational transducer (bubble sensor) to limit before the excursion can be corrected. The system will be stable only under small perturbations. Figure 47 shows the results for a $1/20^\circ$ step in thrust vector deflection. The transducer limit for the low gain case was encountered at 6 sec.

The remaining figures (Figs. 48 through 50) show the effect of coupling between the two degrees of motion. This coupling has been described above, and consists of both the physical and induced types. Figure 48 indicates the translational reaction when that loop is coupled with the rotational loop. The motion is more oscillatory (compare with Fig. 44) than in the uncoupled case because of the influence of the rotational loop. The upper curves correspond to negative coupling, which means that the thrust vector deflection induces a negative torque into the rotational loop. The lower curves are for positive coupling. Two extreme conditions have been studied: viscous damping in the spring (electrical leads). It is seen that the latter case produces greater interaction effects.
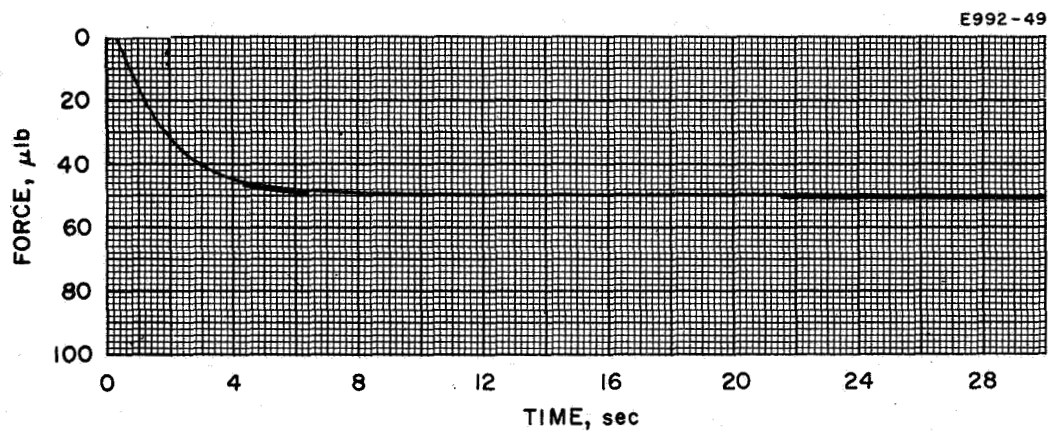
Fig. 45. Force motor response to a step in thrust vector deflection; $\Delta\theta = 1/8^\circ$ (uncoupled).
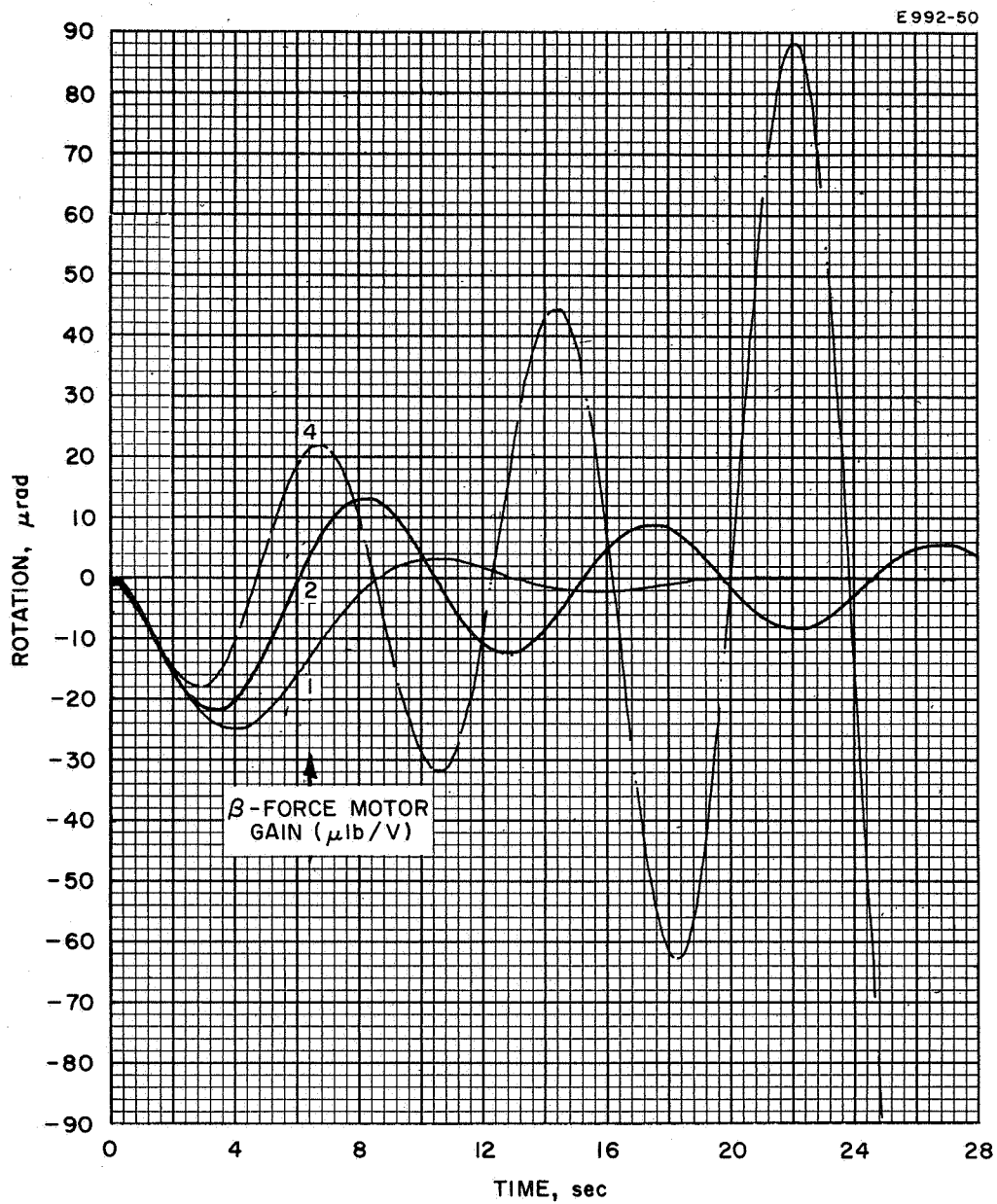
Fig. 46. Rotational response to a step in thrust vector deflection; $\Delta\theta = 1/40^{\circ}$ (uncoupled).
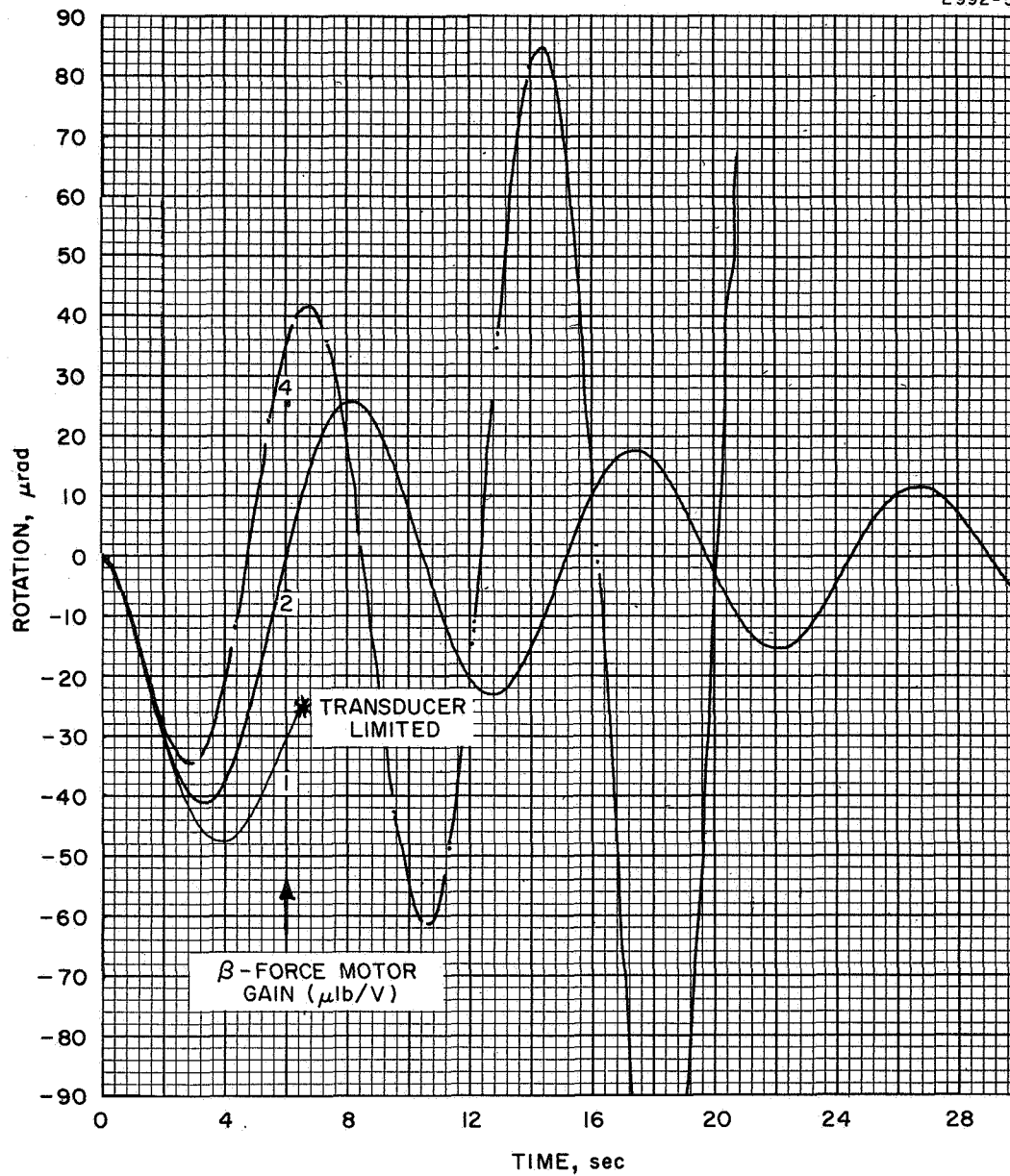
Fig. 47. Rotational response to a step in thrust vector deflection; $\Delta\theta = 1/20^{\circ}$ (uncoupled).
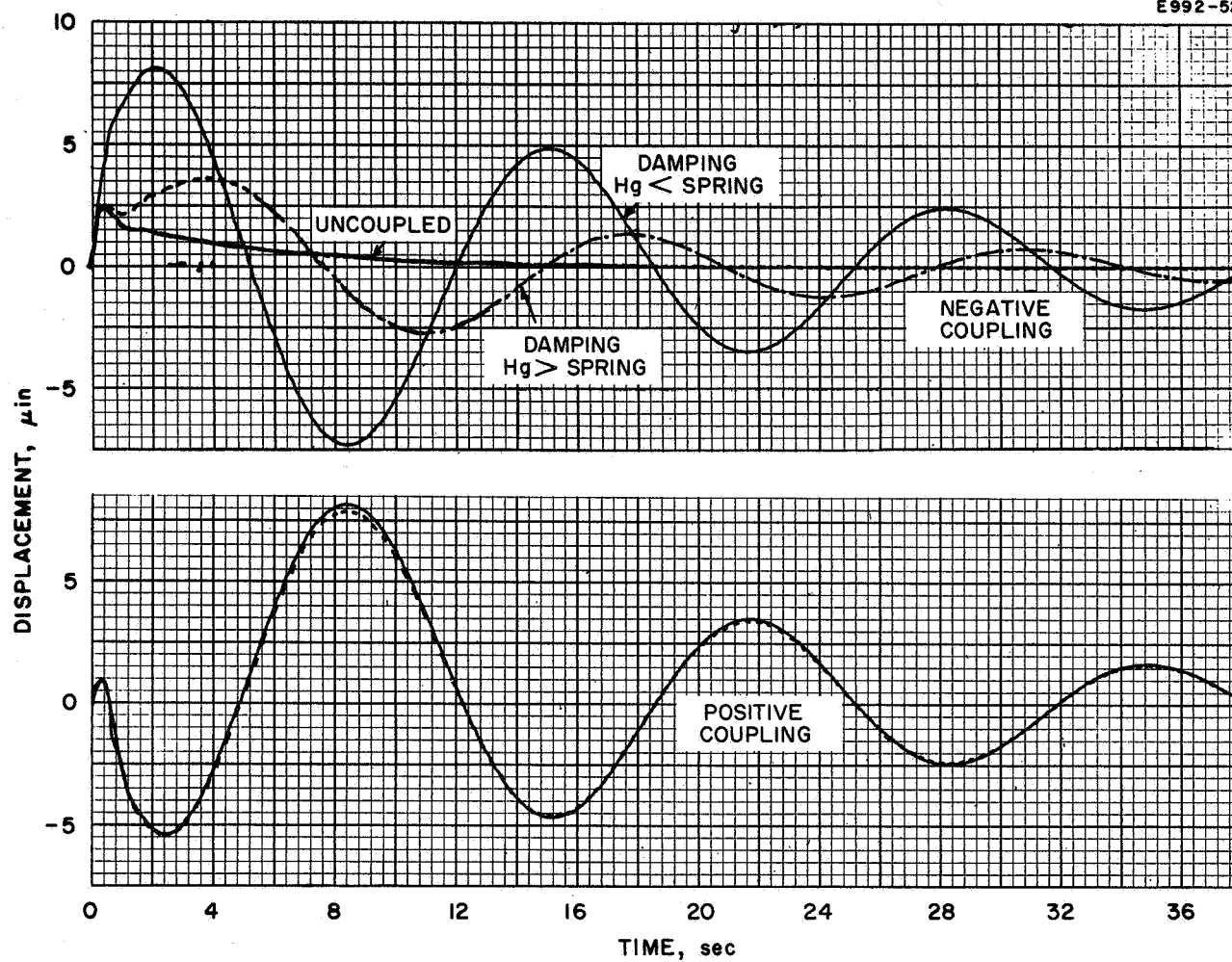
Fig. 48. Displacement response to a step in thrust vector deflection (coupled).

Figure 49 is the associated rotational dynamics as a result of coupling with the translational loop. The results are compared with the uncoupled case. Finally, Fig. 50 gives the effect of x-force motor gain for the coupled case, and shows that the higher gain stabilizes faster.

We conclude that the coupling effects generally cause the individual loop response to be more oscillatory than they would be independently. However, if each loop is stabilized independently, the coupling induces no new instability. The cross coupling effects in the second and third order lead systems (Fig. 40 and 41) were not studied because of the proposal to use linear displacement transducers rather than a bubble sensor which was made at this point.

7. Conclusions

It may be concluded from the above analysis that

a. the bubble sensor may be replaced with linear transducers and that an over-all simplification of the system will result

b. the linear transducers should be designed to provide maximum possible sensitivity (10^5 V/in., if possible)

c. the floating mass should be as light as possible; this suggests exchanging the position of the forcemotor magnets (now mounted on the float) and the coils if suitably flexible leads can be demonstrated.

8. Development of Thrust Stand Components

a. Displacement Sensors — A displacement sensor which utilizes a light beam and a pair of matched photocells has been developed (see Fig. 51); the light falling onto the cell is apertured by a slit mounted on the floating table. The relative motion between the slit and the light bulb and sensors which are mounted on the fixed table causes a variation in the amount of light reaching each half of the split photocell. This produces a difference in voltage across the matched load resistors which may be interpreted directly in terms of the relative motion.
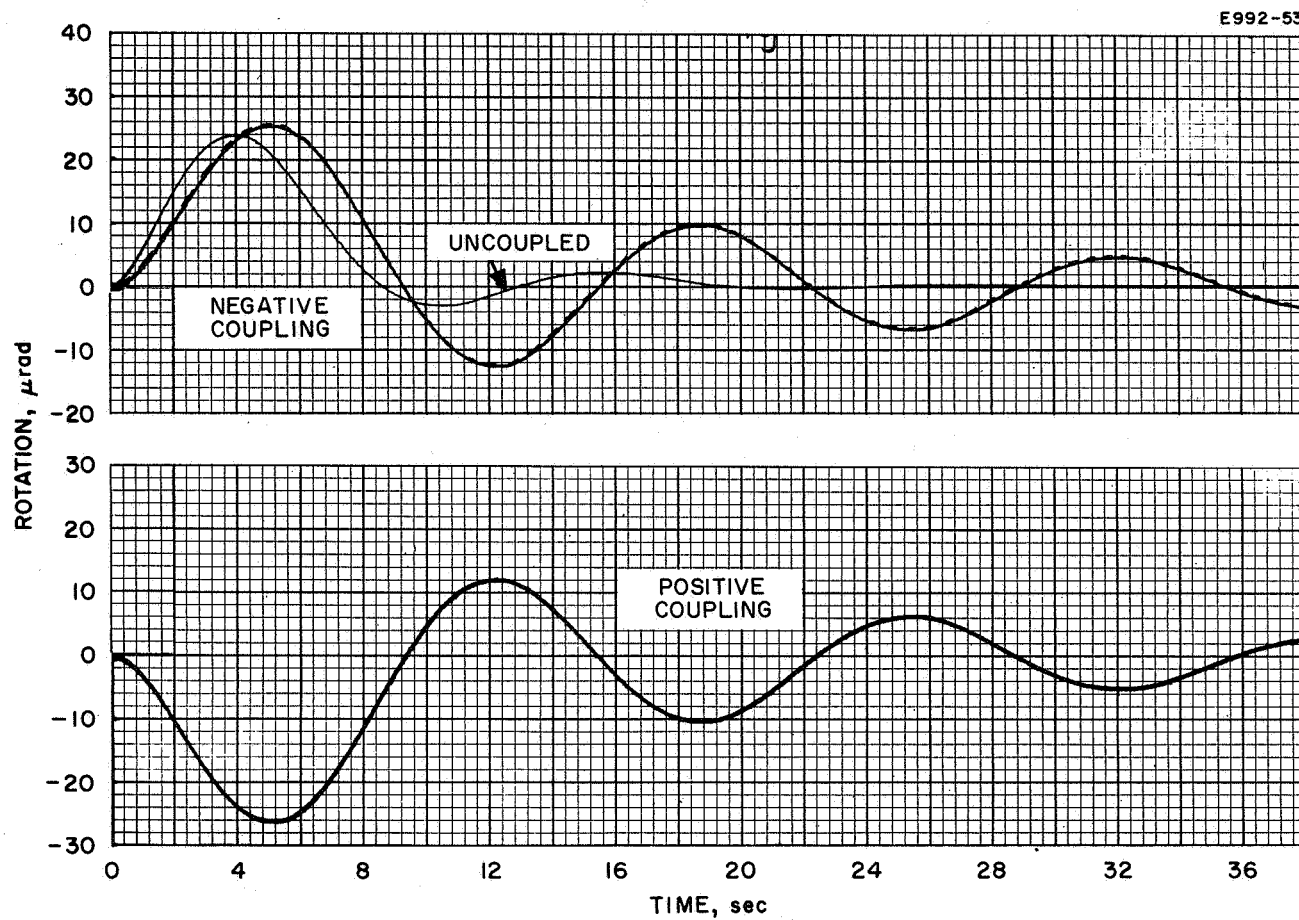
Fig. 49. Rotational response to a step in thrust vector deflection (coupled).
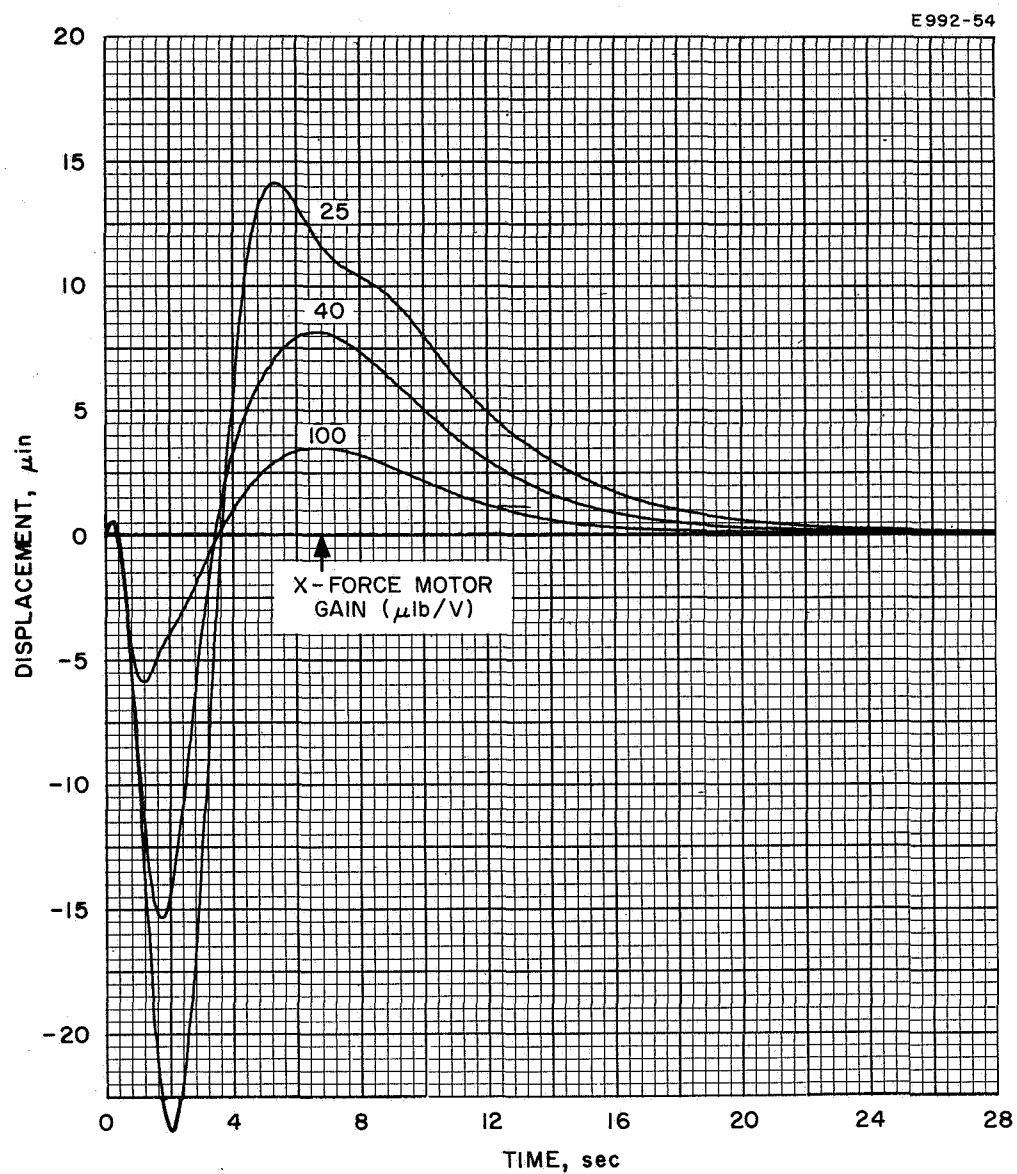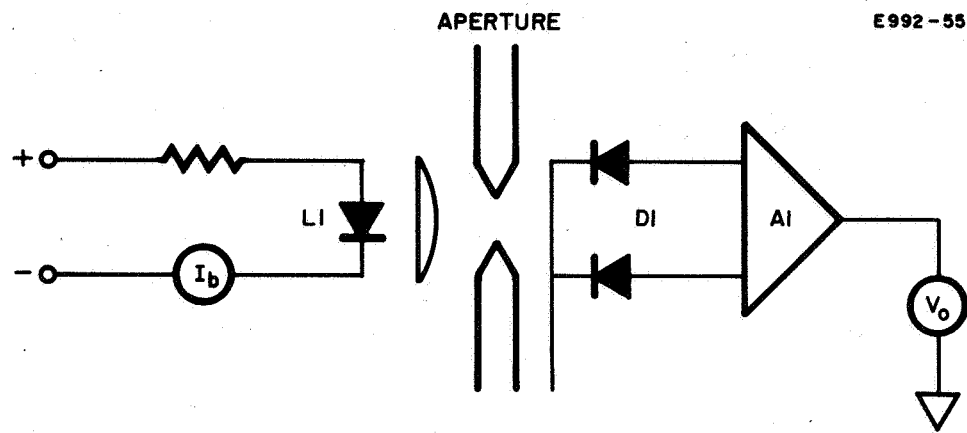
Fig. 50.   Effect of force motor gain on coupled displacement response.

APERTURE

E992-55

AI — BURR BROWN NO. 1506
        GAIN = 200

LI — GAS LIGHT SOURCE
        NO. 470A
        ELECTRO NUCLEAR LABS

DI — IR DETECTOR
        NO. PIN SPOT II
        UNITED DETECTOR TECH

Fig. 51. Optical linear displacement sensor.

115

A system of this type using a United Detector Technology photodetector and gallium arsenide light source has been designed, fabricated, and tested. As shown in Fig. 52, this model, actuated by a micrometer drive, has demonstrated resolution of linear motion of less than 0.0001 in. and good sensitivity. This high sensitivity and the absence of any mechanical coupling between the floating and fixed suspension make this a very attractive system for this application.

b. Forcemotors — Electromechanical forcemotors such as those used to drive loudspeakers are preferred here because the force generated is directly proportional to input current and independent of position over a range which is large compared with the operating range here. It is tentatively planned to mount the permanent magnet driver on the floating suspension and the voice coil on the fixed platform. This increases the weight of the floating system (in contrast to the requirements of the dynamic analysis) but reduces the spring constant associated with the number of leads crossing from the fixed to floating table. As quantitative information concerning lead stiffness becomes available, this decision will be reevaluated.

Three commercial speakers have been disassembled and the forcemotors checked. The most useful forcemotor for this task comes from an Altec speaker, which has a nominal force of 0.5 lb/A. One possible difficulty with the commercial speakers is that the voice coils are by design mounted on very lightweight and delicate structures. This may ultimately necessitate rewinding of the coils on a more rigid form to provide stable mechanical coupling to the table.

c. Electrical Leads — A minimum of 16 leads will be required to operate the thruster and all the actuators necessary for the experiment. These must mechanically connect the floating system and the fixed tank. It is desirable, therefore, that they be as flexible as possible to reduce the spring constant associated with the suspension system. Several lead geometries have been proposed and samples of highly flexible leads have been obtained from an internal HAC source
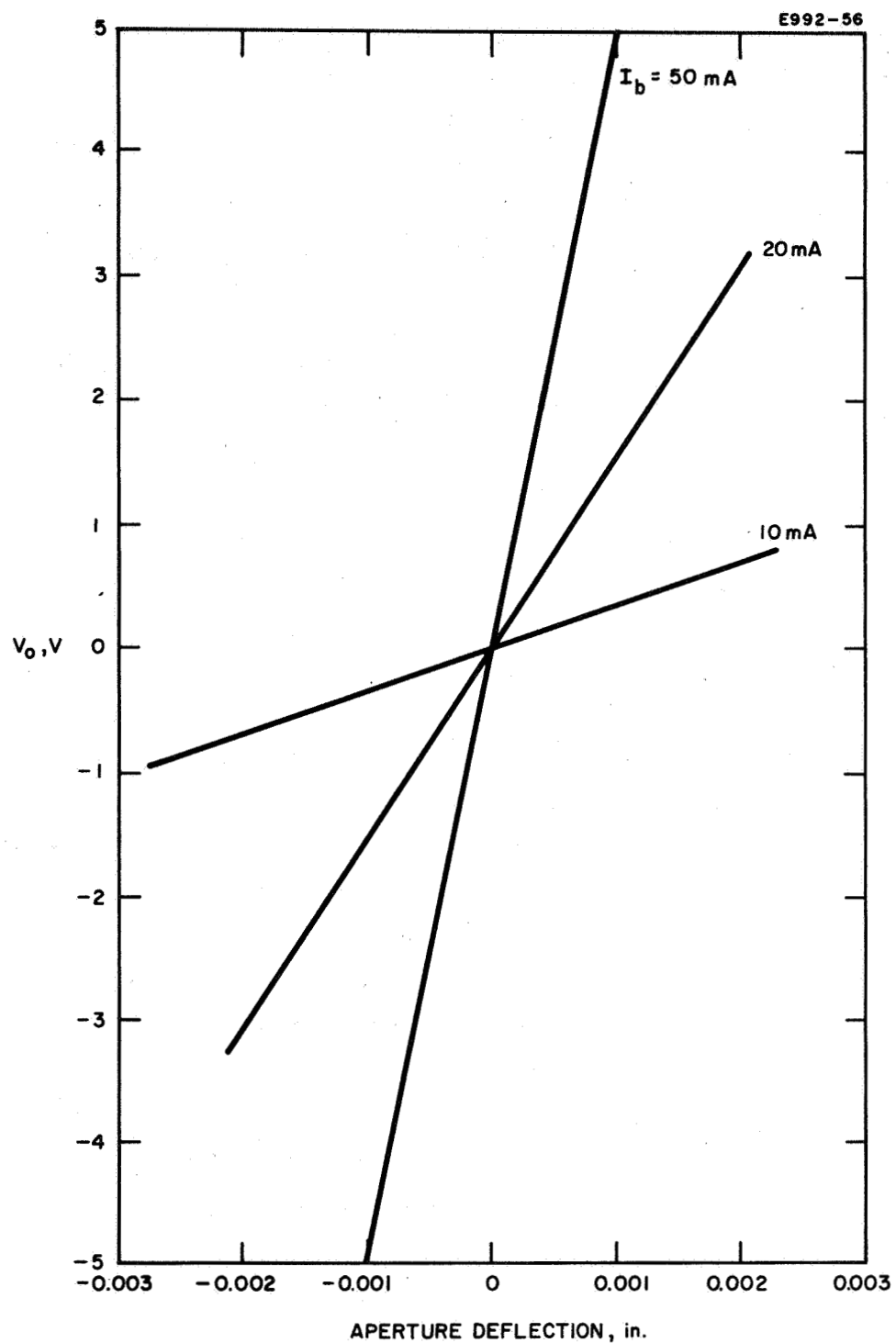
116

Fig. 52. Sensitivity of linear displacement sensor.

and from Sicoil Corp. The spring constants and other features of these leads will be evaluated before the thrust stand design is completed.

B.   Electrode Position Monitors

The linear differential transformer to measure relative electrode motions and the optical system to measure electrode contours were described in the last report.

C.   Electrode Motion Generators

Three actuators are required to move the accelerator electrode in a direction normal to the screen electrode in order to provide a change in accelerator screen spacing as well as tilt. Two more pairs are required to provide both rotation and translation while keeping a fixed spacing between electrodes.

The initial design is based upon a maximum motion of 0.020 in. This consideration ruled out direct thermal expansion because the actuators became unduly large for the permissible temperature range. It was decided to use a cam mechanism (Fig. 53) driven either by a thermally actuated stack of bimetallic washers or by a solenoid. The cam position is locked by an overrunning clutch. Both devices were fabricated and tested in vacuum. The thermal actuator provided smooth operation with full stroke in less than 2 min, but required 20 min to cool so that the next cam position could be activated. This would prove considerably inconvenient during experimentation. The solenoid was a modified high vacuum valve developed for use at $400^{o}C$ with cesium thrusters. Its operation is satisfactory and rapid but may require a dashpot in the final system to reduce the mechanical impulse. The solenoid system has been chosen for the final design.
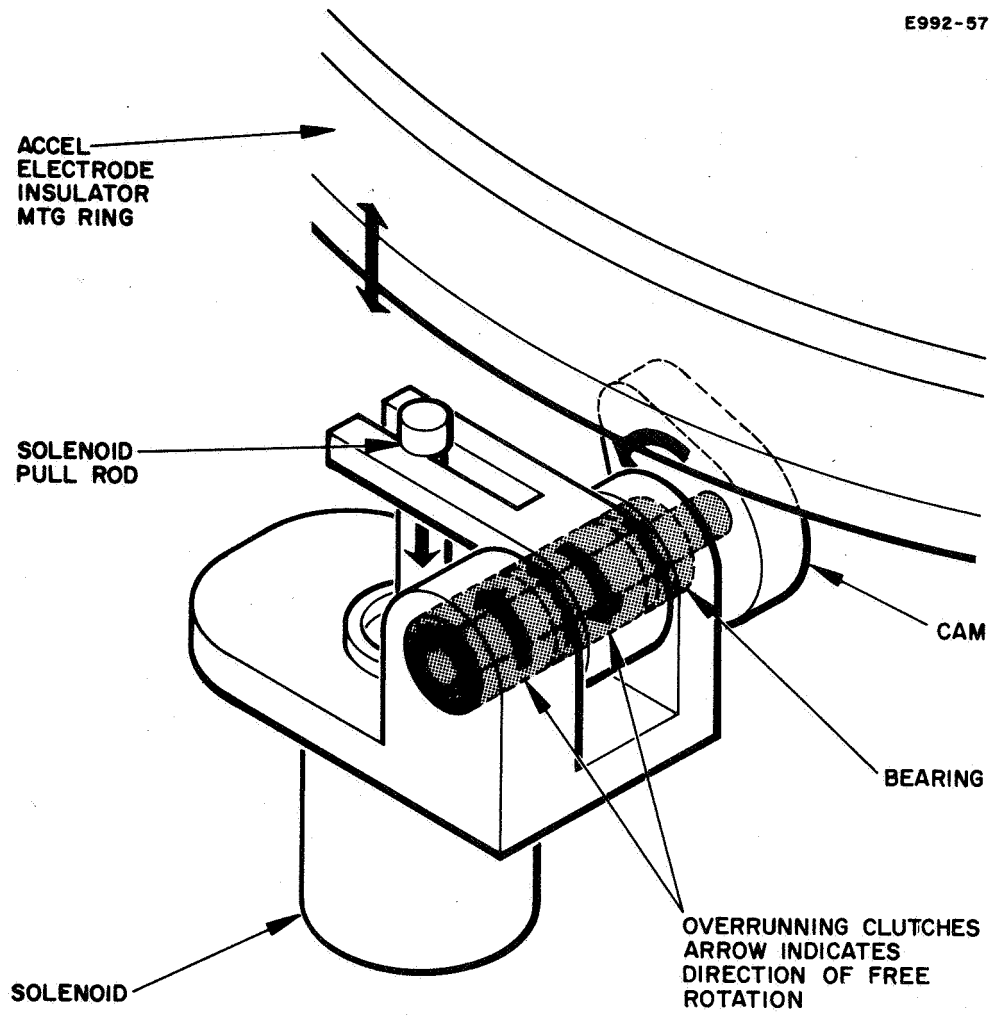
118

ACCEL
ELECTRODE
INSULATOR
MTG RING

SOLENOID
PULL ROD

CAM

BEARING

OVERRUNNING CLUTCHES
ARROW INDICATES
DIRECTION OF FREE
ROTATION

SOLENOID

Fig. 53. Electrode motion actuator.

VI.   SUMMARY AND CONCLUSIONS

The digital computer program for the determination of ion trajectories was used to solve several perturbed cases of electrode motion. With this experience in determining the costs associated with the ion optical studies, the total number of cases which can be run has been estimated.   This estimate is summarized in Table VI, in which the cases already completed are shown circled.   The balance of runs will be completed in August.

TABLE VI

Current Density mA/cm^2	Tilt, rad	Axial Spacing, in.	Transverse Displacement, % of Accel Hole Diameter	Without Screen Hole Countersunk, in.	Constant Beam Current, in.
8	0.02	0.090 0.070 0.050	10 5	0.090^a 0.050^a	0.070^a
4	-	0.090	-	-	-
2	-	0.090 0.070	10 5	-	-

[a]To be done if funds permit.

The computer analysis of electrode temperature distribution and consequent thermally induced stress has been carried out and results have been obtained.   Preliminary analysis of beam deflection resulting from these distortion effects has begun.   The modeling of the thermal and stress analysis is essentially complete; several more cases remain to be run.

The thruster design is complete.   A decision was reached in the thrust stand design, in coordination with the JPL Program Manager, in

favor of the floating suspension type. Extensive analysis of this system has been carried out, with the conclusion that the system will perform satisfactorily for the purpose intended. This analysis showed that a linear displacement transducer will result in lower system complexity and possibly better performance than that with a bubble sensor. The photoelectric position sensor has been tested and found satisfactory for use with the thrust stand.

VII.   PROGRAM FOR NEXT QUARTER

The remaining ion optical cases with perturbed electrode motion will be completed early in the next quarter. These results will be used, together with the electrode misalignment errors, to predict the effective thrust vector misalignment for a thruster.

Design parameters of the thrust stand will be defined.

It is anticipated that the program will be completed on schedule.

VIII.   NEW TECHNOLOGY

The following items of new technology were conceived and developed to varying degrees in the course of this program.

1. Thrust stand using mercury suspension

2. Thruster electrode motion generator by cam actuator

3. Linear motion monitor using optical means

4. Modification of digial computer program.

REFERENCES

1. K. Amboss, IEEE Trans. <u>ED-12</u>, 313 (1965).

2. W.C. Lathem, NASA TMX-52369.

3. "Structural Analysis of Shells by the Finite Element Method," Hughes Space Systems Division, Report No. 70090R-23.

4. W.J. O'Donnell and B.F. Langer, "Design of perforated plates," ASME J. Vol. 308 (1962).

APPENDIX I — DETERMINATION OF THE UPSTREAM BOUNDARY

The correct position of the upstream boundary was sought by successive deformations until the self-consistent current exactly equalled the predicted value. The accuracy with which the boundary must be known in order to match the current within 5% is estimated. The program calculates the emission density at the upstream plasma by assuming that a small planar diode exists in front of the emitter and by using Child's law this is

$$I = PV^{3/2}$$

where

$P \equiv$ perveance of the system

$I \equiv$ total ion emission

$V \equiv$ voltage across the assumed diode.

Therefore,

$$\delta I = \frac{3}{2} V^{1/2} P \, \delta V.$$

Assuming P is constant,

$$\delta I = \frac{3}{2} V^{1/2} P \, \frac{\partial V}{\partial x} \, \delta n$$

or

$$\frac{\delta I}{I} = \frac{3}{2} \frac{1}{V} \frac{\partial V}{\partial x} \, \delta n$$

where $\delta I/I$ is the percentage change in current due to a movement δx of the boundary. V is the voltage across the diode and $\partial V / \partial x$ is the electric field at the "anode."

In practice, the program assumes a diode which is 3 mesh units long. The field and voltage at the "anode" location for the unperturbed solution are approximately 14 kV/in. and 70 V, respectively.

Hence

$$\delta x \;=\; 0.05 \times \frac{2}{3} \times \frac{70}{14 \times 10^3} \text{ in.} \;=\; 0.000166 \text{ in.}$$

This is less than 0.001x (the screen aperture diameter) and is therefore too small to be satisfactorily represented on any reasonable scale chosen for the geometry.

The effect of choosing a boundary at the best estimated position and imposing the correct current solution on it is equivalent to assuming that the ion has a small thermal velocity at the boundary. If a boundary were chosen which was in error by δx it would represent a thermal energy E_T of the ions of approximately $e(\partial V/\partial x)\delta n$ eV. For the case above where
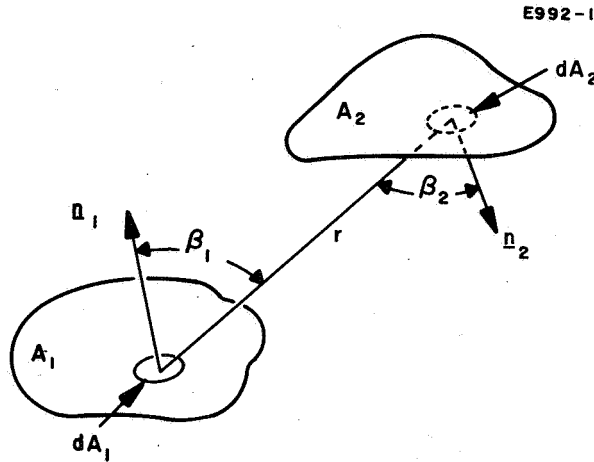
$$\delta x \;=\; 0.15 \times 10^3$$

and

$$\left(\frac{\partial V}{\partial x}\right) \;=\; 14 \times 10^3,$$

$$E_T \;=\; 2.1 \text{ eV}.$$

130

APPENDIX II — DETERMINATION OF GEOMETRIC (VIEW) FACTORS

A. Definition of Geometric (View) Factors for Radiative Heat Transfer

E992-1

The definition of the geometric (view) factor $F_{A_1-A_2}$ which enters into the calculation of the radiant heat transfer between two finite surfaces A_1, A_2 follows from the assumptions that:

1. The intensity of heat radiated from an infinitesimal area element dA_1 is proportional to dA_1 and varies with direction as the cosine of the angle from the normal $\underline{n}_1$ to dA_1.

2. The quantity of heat incident on an element dA_2 from dA_1 is proportional to the solid angle $d\omega = dA_2 \cos\beta_2/r^2$ subtended by dA_2 as seen from dA_1.

The ratio

$$\frac{\displaystyle\int_{A_1}\int_{A_2} \frac{\cos\beta_1 \cos\beta_2}{r^2} dA_1 dA_2}{\displaystyle\int_{A_1}\int_{2\pi} \cos\beta_1 \, dA_1 \, d\omega} = \frac{1}{A_1}\int_{A_1}\int_{A_2} \frac{\cos\beta_1 \cos\beta_2}{\pi r^2} dA_1 dA_2$$

$$\equiv F_{A_1-A_2} \quad ,$$

of the heat radiated by area A_1 which is incident on area A_2 to the heat radiated by A_1 in all directions (2π solid angle) is defined as the view factor $F_{A_1} - A_1$ from area A_1 to A_2.

From this definition of $F_{A_1-A_2}$, the very useful reciprocity relation

$$A_1 \, F_{A_1-A_2} = A_2 \, F_{A_2-A_1}$$

follows immediately. Another useful relation for deriving one view factor from others is based on conservation of energy. This states that if a surface A_1 radiates to surface A_2 and $A_2 = A_2' + A_2''$, then

$$F_{A_1-A_2} = F_{A_1-A_2'} + F_{A_1-A_2''} \quad .$$

B. Four Elementary View Factors

Formulas for the four basic view factors which are used in the determination of the over-all grid system view factors are given below.

1. Cylinder Walls to Disk

In the previous quarterly report the view factor from the walls of a cylinder to a disk was derived. With new notation corresponding to the figure below, the formula is

E992-2

$$X = \frac{h}{\ell} \; , \quad Y = \frac{r}{\ell}$$
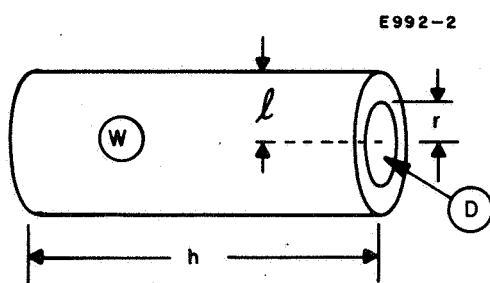
$$F_{WD}(X, Y) = \frac{1}{4X} \left\{ \sqrt{\left(X^2 + Y^2 + 1\right)^2 - 4Y^2} - \left(1 - Y^2\right)^2 - X^2 \right\}$$

2. Section of the Cylinder Wall to Disk
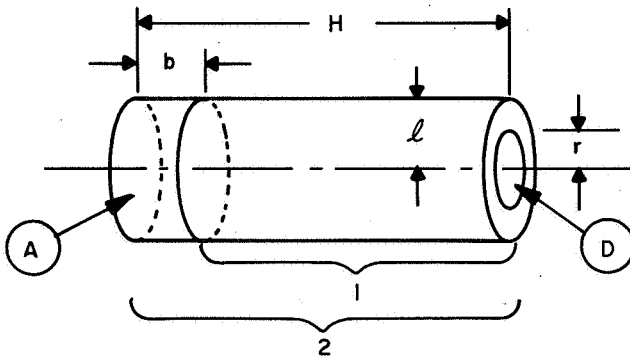
Using the reciprocity law in the relation,

$$F_{D-2} = F_{D-A} + F_{D-1} - 1$$

gives

$$A_2 F_{2-D} = A_A F_{A-D} + A_1 F_{1-D} \quad,$$

where

E992-3

$$A_1 \quad = \quad 2\pi\ell(H-b)$$

$$A_2 \quad = \quad 2\pi\ell H$$

$$A_D \quad = \quad \pi r^2$$

$$F_{1-D} \quad = \quad F_{WD}\left(\frac{H-b}{\ell}, \frac{r}{\ell}\right)$$

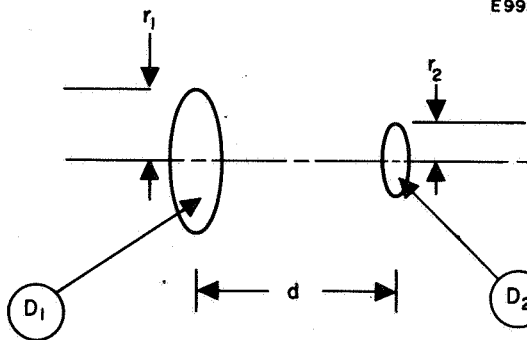$$F_{2-D} \quad = \quad F_{WD}\left(\frac{H}{\ell}, \frac{r}{\ell}\right) \quad .$$

The view factor from the section of a cylinder A to the disk D is then found to be

$$F_{AD}(H, b, \ell, r) = \frac{H}{b} F_{WD}\left(\frac{H}{\ell}, \frac{r}{\ell}\right) - \frac{H-b}{b} F_{WD}\left(\frac{H-b}{\ell}, \frac{r}{\ell}\right)$$

The next two view factors are found in many texts. See, for example, Eckert.[*]

3.   Disk to Disk

E992-4

$$X = \frac{d}{r_1}; \quad Y = \frac{r_2}{d}$$
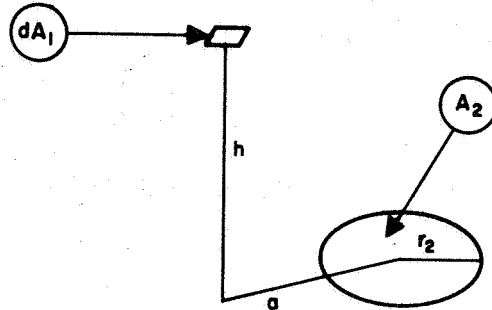
$$Z = 1 + (1 + Y^2) X^2$$

$$F_{DD}(r_1, r_2, d)$$

$$= \frac{1}{2}\left\{Z - \sqrt{Z^2 - 4(XY)^2}\right\}$$

---

[*]E. Eckert, Heat and Mass Transfer (McGraw-Hill, New York, 1959).

4. Area Element to Disk

$$X = \frac{h}{a}, \quad Y = \frac{r_2}{h}$$

$$Z = 1 + (1 + Y^2)\, X^2$$

$$F_{dA_1-A_2} = \frac{1}{2}\left\{1 - \frac{Z - 2\,X^2 Y^2}{\sqrt{Z^2 - 4\,X^2 Y^2}}\right\}$$
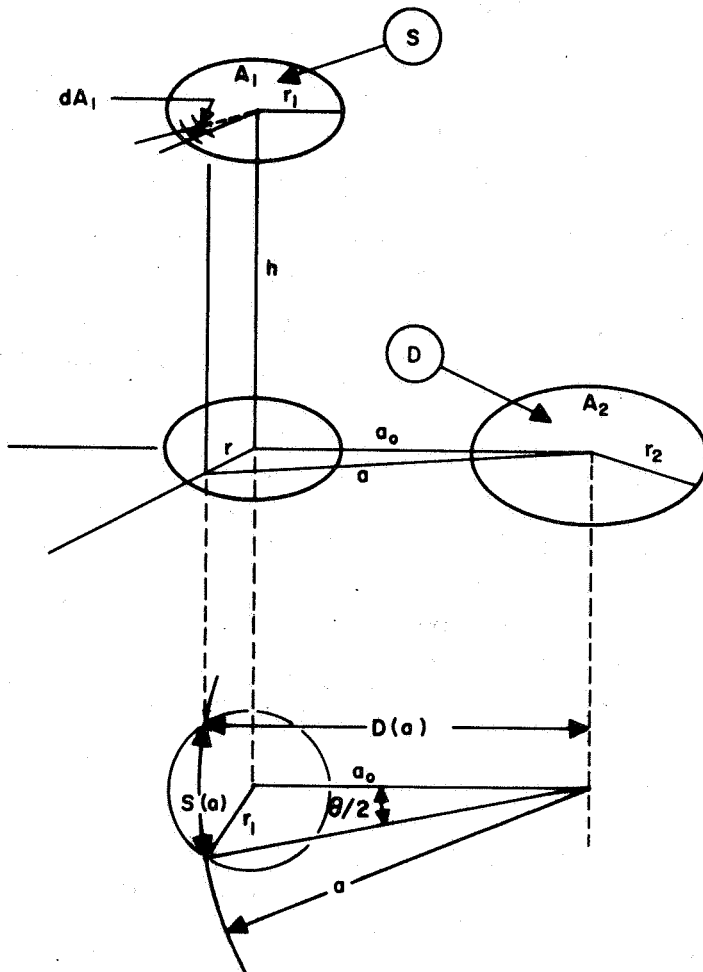
5. Disk to Off-Axis Disk

The view factor from a disk A_1 to a parallel but off-axis disk A_2 is found from the integral of $F_{dA_1-A_2}$:

$$F_{A_1-A_2} = \frac{1}{A_1} \int_{A_1} F_{dA_1-A_2}\, dA_1 \quad .$$

This integral must be calculated numerically; the most convenient form is

$$F_{A_1-A_2} = \frac{1}{A_1} \int_{a_o-r_1}^{a_o+r_1} F_{dA_1-A_2}\, S(a)\, da$$

where

$$S(a) = 2a \cos^{-1}\left\{\frac{D(a)}{a}\right\} , \qquad D(a) = \frac{a_o^2 + a^2 - r_1^2}{2a_o} .$$

In the applications below, the view factor $F_{A_1-A_2}$ is referred to as $F_{SD}(h, r_1, r_2, a_o)$, i.e.,

$$F_{SD}(h, r_1, r_2, a_o) = \frac{1}{A_1} \int_{a_o-r_1}^{a_o+r_1} F_{dA_1-A_2} S(a)\, da .$$

C. Calculation of View Factors for the Grid System

1. View Factor F_{1-2}

The figure at right shows a pair of aligned apertures in the perforated plates S and A. Node 1 corresponds to the disk which is at the back of the plate S aperture and node 2 corresponds to the cylindrical aperture wall. (For simplicity, the screen apertures are not countersunk.) The view factor F_{1-2} is given by

E992-8
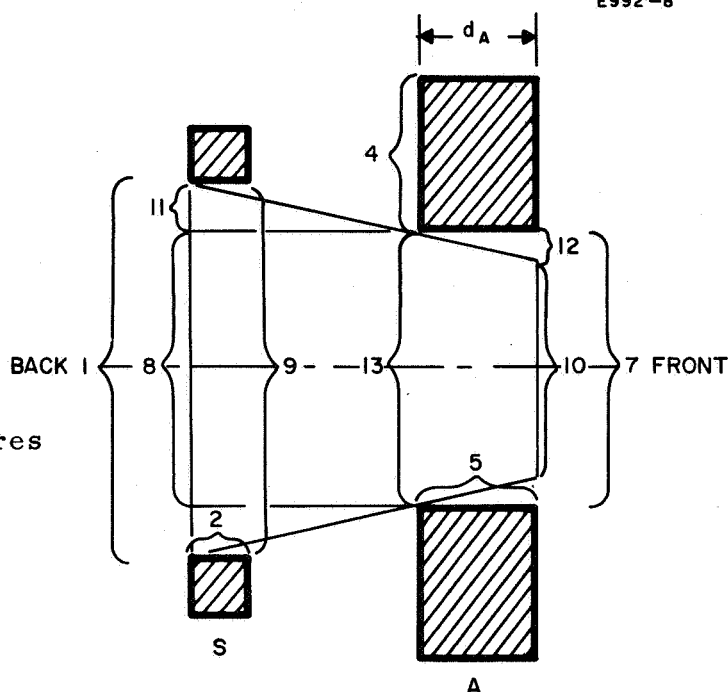
$$F_{1-2} = 1 - F_{1-9} = 1 - F_{DD}(r_s, r_s, d_s) .$$

135

2. View Factor F_{1-7}

Node 7 is a disk which is the front of the plate A aperture. Auxiliary nodes 8, 10, 11, and 12 are also used in the calculation of F_{1-7}. Nodes 8 and 10 are disks concentric to 11 and 7, and nodes 11 and 12 are the remaining annuli. An "aperture" effect is present in the calculation of F_{1-7} because of the nonzero thickness d_A of plate A. Thus F_{1-7} is a function of d_A. It would be difficult to account for this partial shielding between nodes 1 and 7 in the view factor calculation. Instead, upper and lower bounds are found for $F_{1-7}(d_A)$. From the geometry it is clear that for $d_A > 0$,

$$F_{1-7}(d_A) < F_{1-7}(0) .$$

A good lower bound for $F_{1-7}(d_A)$ is found as follows. Using the equations

$$F_{1-7}(d_A) = F_{1-12} + F_{1-10}$$

$$F_{1-12} = \frac{A_{11}}{A_1} F_{11-12} + \frac{A_8}{A_1} F_{8-12} ,$$

we obtain

$$F_{1-10} + \frac{A_8}{A_1} F_{8-12} + \frac{A_{11}}{A_1} F_{11-12}(d_A) = F_{1-7}(d_A) < F_{1-7}(0)$$

$$= F_{1-10} + \frac{A_{11}}{A_1} F_{11-12}(0) + \frac{A_8}{A_1} F_{8-12} .$$

Thus the inequalities

$$F_{1-10} + \frac{A_8}{A_1} F_{8-12} < F_{1-7}(d_A) < F_{1-7}(0) \qquad (II-1)$$

bound $F_{1-7}(d_A)$ below by taking $F_{11-12}(d_A) = 0$ and above by having $F_{11-12}(d_A) = F_{11-12}(0)$. Since $F_{11-12}(d_A) < F_{11-12}(0) << 1$, the

136

complicated view factor $F_{11-12}(d_A)$ is actually negligible. In terms of the elementary view factors given, eq. (II-1) becomes

$$F_{DD}(r_S, r_{10}, w) + \left(\frac{r_A}{r_{10}}\right)^2 \left\{ F_{DD}(r_A, r_A, w) - F_{DD}(r_A, r_{10}, w) \right\} < F_{1-7}(d_A)$$

(II-2)

$$F_{1-7}(d_A) > F_{DD}(r_S, r_A, w)$$

(II-3)

where

$$w = d_S + d + d_A$$

$$r_{10} = r_A - \frac{d_A}{d + d_S}(r_S - r_A) \quad .$$

3.   View Factor F_{1-4}

Node 4 corresponds to all of the material on the back side of plate A. The auxiliary nodes 9 and 13 are disks corresponding to the front of the plate S aperture and the back of the plate A aperture. The view factor F_{1-4} will be found from the relation

$$F_{1-4} = F_{1-9} - F_{1-13'} \quad ,$$

where node 13' corresponds to the disks at the back of all of the plate A apertures. The view factors F_{1-9} and $F_{1-13'}$ are given by

$$F_{1-9} = F_{DD}(d_S, r_S, r_S)$$

$$F_{1-13'} = F_{DD}(d_S + d, r_S, r_A) + 6 F_{SD}(d_S + d, r_S, r_A, S_o) \quad .$$

In the expression for $F_{1-13'}$ only the six apertures surrounding node 13 were considered, and the shielding due to the thickness of plate S was neglected. The approximate expression for F_{1-4} is then

$$F_{1-4} = F_{DD}(d_S, r_S, r_S) - \left\{ F_{DD}(d_S + d, r_S, r_A) + 6 F_{SD}(d_S + d, r_S, r_A, S_o) \right\}$$

4. **View Factor F_{1-5}**

Node 5 represents the cylindrical wall of the aperture in plate A. It is easily seen that
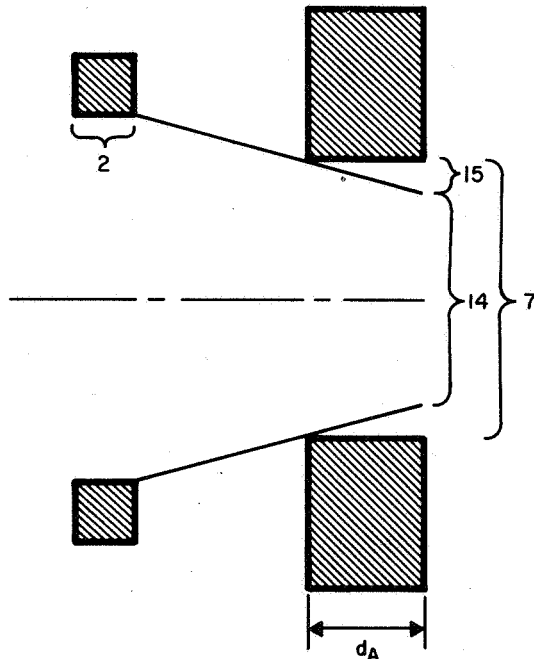
$$F_{1-5} = F_{1-13} - F_{1-7}$$

$$F_{1-5} = F_{DD}(d_S + d, r_S, r_A) - F_{1-7}(d_A)$$

where the value of $F_{1-7}(d_A)$ is chosen from (II-2) and (II-3).

5. **View Factor F_{2-7}**

E992-22

As in the case of F_{1-7}, there is partial shielding in the path from node 2 to node 7, because of the nonzero thickness d_A of plate A. Instead of calculating $F_{2-7}(d_A)$ precisely, an estimate is made based on upper and lower bounds. An upper bound which neglects the shielding completely is $F_{2-7}(d_A) < F_{2-7}(0)$. A lower bound which omits the difficult view factor F_{2-15} is $F_{2-7}(d_A) > F_{2-14}$. In terms of the elementry view factor formulas these bounds become

$$F_{AD}(w, d_S, r_{14}, r_S) < F_{2-7}(d_A) < F_{AD}(w, d_S, r_A, r_S)$$

138

where

$$w = d_S + d + d_A \ ,$$

$$r_{14} = r_A - \frac{d_A}{d} \ (r_S - r_A) \quad .$$

6.   View Factor F_{2-5}

The view factor F_{2-5} is found from the relation

$$F_{2-5} = F_{2-13} - F_{2-7} \ ;$$

node 13 is shown in the figure in Section C-1 of this appendix. The formula for F_{2-5} is

$$F_{2-5} = F_{AD}(d_S + d, \ d_S, \ r_A, \ r_S) - F_{2-7}(d_A)$$

where an estimate of $F_{2-7}(d_A)$ is made using (II-1)

7.   View Factor F_{2-2}

Since node 2 represents a concave surface it radiates to itself. The view factor F_{2-2} is found from the equation

$$F_{2-9} + F_{2-1} + F_{2-2} = 1,$$

and is given by

$$F_{2-2} = 1 - 2 F_{AD}(d_S, \ d_S, \ r_S, \ r_S)$$

8.   View Factor F_{3-4}

Node 3 represents all the material surface on the front of plate S. The calculation of F_{3-4} takes several steps. First we find F_{9-4} from the equations

139

$$F_{9-4} = 1 - F_{9-13'}$$

$$F_{9-13'} = F_{9-13} + 6 F_{SD}(d, r_S, r_A, S_o) \ .$$

The expression for $F_{9-13'}$ includes only the six nearest holes surrounding node 13. More distant groups of holes consist of $6\sqrt{3}\,S_o$, 6 at $2S_o$, 12 at $1.5\sqrt{3}\,S_o$, etc. The view factors from node 9 to node 13 and to each of the above groups are shown in Fig. II-1 as functions of the plate spacing d. The contributions to the over-all view factor $F_{9-13'}$ from holes more distant than S_o are negligibly small. Next, we define node 9' as the disks corresponding to the fronts of <u>all</u> the holes in plate S, and note that

$$F_{9'-4} = F_{9-4} \ .$$

The view factor $F_{4-9'}$ is then found from the reciprocity condition

$$F_{4-9'} = \frac{A_{9'}}{A_4} F_{9'-4} \ .$$

The area ratio $A_{9'}/A_4$ is defined by

$$\frac{A_{9'}}{A_4} = \frac{f_S}{1-f_A}$$

where f_S and f_A are the opened area fractions in plates S and A. Finally, the desired view factor F_{3-4} is found from the equations

$$F_{3-4} = \frac{A_4}{A_3} F_{4-3} = \left(\frac{1-f_S}{1-f_A}\right)^{-1} F_{4-3}$$
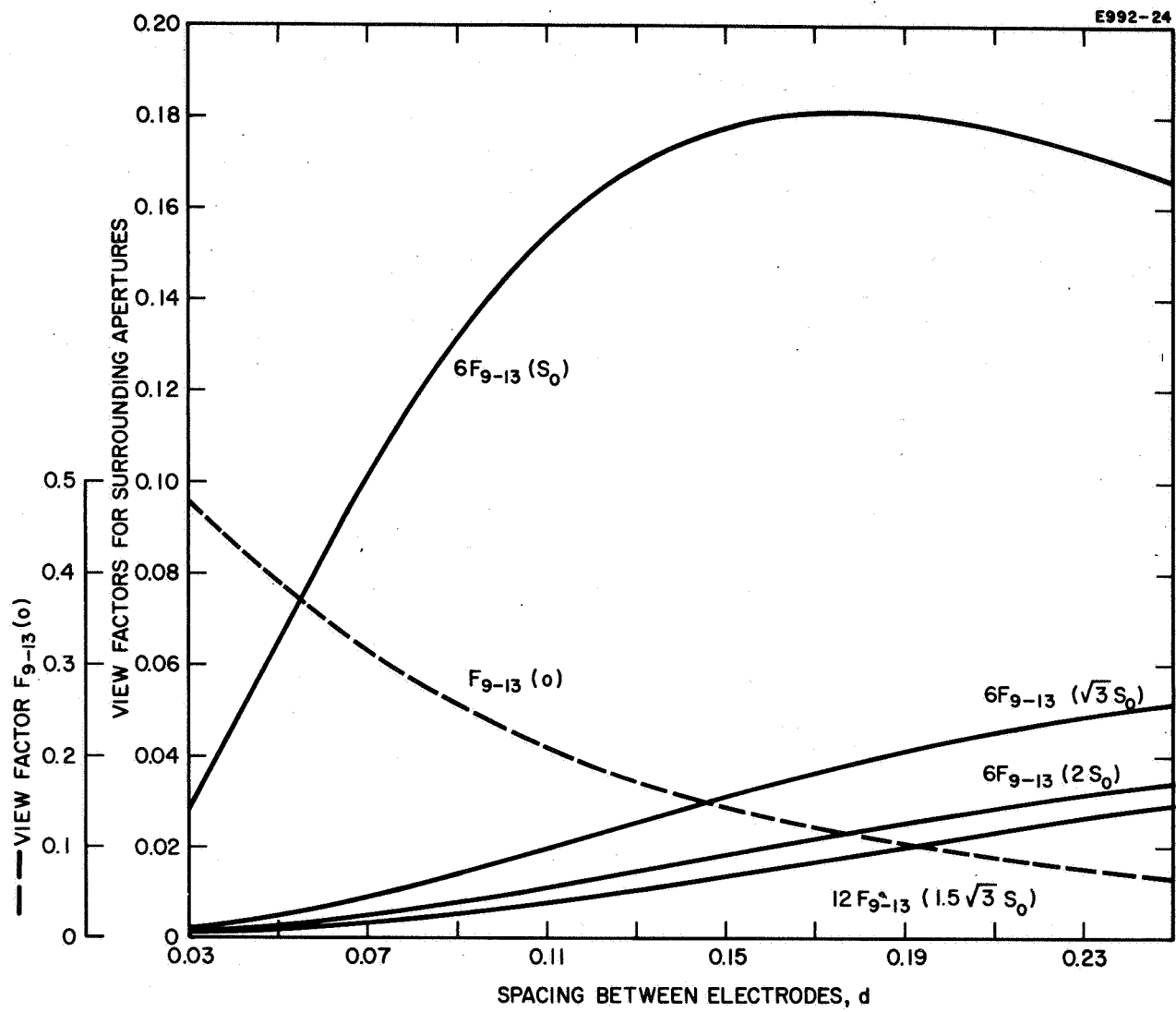
$$F_{4-3} = 1 - F_{4-9'}$$

Fig. II-1. Terms in the over-all view factor F_{9-13}.

The resulting expression is

$$F_{3-4} = \left(\frac{1-f_S}{1-f_A}\right)^{-1} \cdot \left\{1 - \frac{f_S}{1-f_A} \left(1 - F_{DD}(d, r_S, r_A) - 6 F_{SD}(d, r_S, r_A, S_o)\right)\right\}$$

9.   **View Factors $F_{3-5'}$, $F_{3-7'}$**

Nodes 5' and 7' correspond to the cylindrical wall and front disk surface of all of the plate A apertures. From the equation

$$F_{3-13'} = 1 - F_{3-4} = F_{3-5'} + F_{3-7'} ,$$

we learn the sum $(F_{3-5'} + F_{3-7'})$. No good approximation has been found to date for either; the difficulty is apparently that the shielding due to plate A enters significantly. Until more time is spent on their calculation, we will take

$$F_{3-5'} = F_{3-7'} = \frac{1}{2} F_{3-13'} = \frac{1}{2}(1 - F_{3-4}) .$$

10.   **View Factors F_{5-7}, F_{5-5}**

The view factors F_{5-7}, F_{5-5} are given by the formulas

$$F_{5-7} = F_{AD}(d_A, d_A, r_A, r_A)$$

$$F_{5-5} = 1 - 2 F_{5-7} .$$

142